Handbook T-I

Engineering and Applied Sciences

MARTÍNEZ-VARGAS, Sergio
FIGUEROA-RAMÍREZ, Sandra Jazmín
PATIÑO-CARACHURE, Cristóbal
SIERRA-GRAJEDA, Juan Manuel   *Coordinators*

ECORFAN®

Coordinators
MARTÍNEZ-VARGAS, Sergio. PhD
FIGUEROA-RAMÍREZ, Sandra Jazmín. PhD
PATIÑO-CARACHURE, Cristóbal. PhD
SIERRA-GRAJEDA, Juan Manuel. PhD

Editor in Chief
VARGAS-DELGADO, Oscar. PhD

Executive Director
RAMOS-ESCAMILLA, María. PhD

Editorial Director
PERALTA-CASTRO, Enrique. MsC

Web Designer
ESCAMILLA-BOUCHAN, Imelda. PhD

Web Diagrammer
LUNA-SOTO, Vladimir. PhD

Editorial Assistant
SORIANO-VELASCO, Jesús. BsC

Philologist
RAMOS-ARANCIBIA, Alejandra. BsC

©ECORFAN-México, S.C.

Handbooks

Definition of Handbooks

Scientific Objectives

To support the International Scientific Community in its written production of Science, Technology and Innovation in the CONAHCYT and PRODEP research areas.

ECORFAN-Mexico, S.C. is a Scientific and Technological Company in contribution to the formation of Human Resources focused on the continuity in the critical analysis of International Research and is attached to the RENIECYT of CONAHCYT with number 1702902, its commitment is to disseminate research and contributions of the International Scientific Community, academic institutions, agencies and entities of the public and private sectors and contribute to the linkage of researchers who perform scientific activities, technological developments and training of specialized human resources with governments, businesses and social organizations.

To encourage the interlocution of the International Scientific Community with other study centres in Mexico and abroad and to promote a wide incorporation of academics, specialists and researchers to the serial publication in Science Niches of Autonomous Universities - State Public Universities - Federal IES - Polytechnic Universities - Technological Universities - Federal Technological Institutes - Teacher Training Colleges - Decentralised Technological Institutes - Intercultural Universities - S&T Councils - CONAHCYT Research Centres.

Scope, Coverage and Audience

Handbooks is a product edited by ECORFAN-Mexico S.C. in its Holding with repository in Mexico, it is a refereed and indexed scientific publication. It admits a wide range of contents that are evaluated by academic peers by the double-blind method, on topics related to the theory and practice of the CONAHCYT and PRODEP research areas respectively with diverse approaches and perspectives, which contribute to the dissemination of the development of Science, Technology and Innovation that allow arguments related to decision-making and influence the formulation of international policies in the field of Science. The editorial horizon of ECORFAN-Mexico® extends beyond academia and integrates other segments of research and analysis outside that field, as long as they meet the requirements of argumentative and scientific rigour, in addition to addressing issues of general and current interest of the International Scientific Society.

Editorial Board

Arbitration Committee

VALERDI, Ricardo. PhD
Universidad de Arizona

RODRIGUEZ - ROBLEDO, Gricelda. PhD
Universidad Tecnológica de Morelia

CENDEJAS José. PhD
Universidad Tecnológica de Morelia

CORTES - MORALES, Griselda. PhD
Universidad Autónoma de Coahuila

FERREIRA - MEDINA, Heberto. PhD
Institute of Research in Ecosystems - UNAM Campus Morelia

GONZÁLEZ - SILVA, Marco Antonio. PhD
Universidad Politécnica Metropolitana de Hidalgo

CRUZ - BARRAGÁN, Aidee. PhD
Universidad de la Sierra Sur

PALMA, Oscar. PhD
Instituto Tecnológico de Conkal

BARRON, Juan. PhD
Universidad Tecnológica de Jalisco

SANDOVAL - GUTIÉRREZ, Jacobo. PhD
Universidad Autónoma Metropolitana

Assignment of Rights

By submitting a Scientific Work to ECORFAN Handbooks, the author undertakes not to submit it simultaneously to other scientific publications for consideration. To do so, the author must complete the Originality Form for his or her Scientific Work.

The authors sign the Authorisation Form for their Scientific Work to be disseminated by the means that ECORFAN-Mexico, S.C. in its Holding Mexico considers pertinent for the dissemination and diffusion of their Scientific Work, ceding their Scientific Work Rights.

Declaration of Authorship

Indicate the name of 1 Author and a maximum of 3 Co-authors in the participation of the Scientific Work and indicate in full the Institutional Affiliation indicating the Unit.

Identify the name of 1 author and a maximum of 3 co-authors with the CVU number -PNPC or SNI-CONAHCYT- indicating the level of researcher and their Google Scholar profile to verify their citation level and H index.

Identify the Name of 1 Author and 3 Co-authors maximum in the Science and Technology Profiles widely accepted by the International Scientific Community ORC ID - Researcher ID Thomson - arXiv Author ID - PubMed Author ID - Open ID respectively.

Indicate the contact for correspondence to the Author (Mail and Telephone) and indicate the Contributing Researcher as the first Author of the Scientific Work.

Plagiarism Detection

All Scientific Works will be tested by the PLAGSCAN plagiarism software. If a Positive plagiarism level is detected, the Scientific Work will not be sent to arbitration and the receipt of the Scientific Work will be rescinded, notifying the responsible Authors, claiming that academic plagiarism is typified as a crime in the Penal Code.

Refereeing Process

All Scientific Works will be evaluated by academic peers using the Double Blind method. Approved refereeing is a requirement for the Editorial Board to make a final decision which will be final in all cases. MARVID® is a spin-off brand of ECORFAN® specialised in providing expert reviewers all of them with PhD degree and distinction of International Researchers in the respective Councils of Science and Technology and the counterpart of CONAHCYT for the chapters of America-Europe-Asia-Africa and Oceania. The identification of authorship should only appear on a first page, which can be removed, in order to ensure that the refereeing process is anonymous and covers the following stages: Identification of ECORFAN Handbooks with their author occupancy rate - Identification of Authors and Co-authors - PLAGSCAN Plagiarism Detection - Review of Authorisation and Originality Forms-Assignment to the Editorial Board - Assignment of the pair of Expert Referees - Notification of Opinion - Statement of Observations to the Author - Modified Scientific Work Package for Editing - Publication.

ECORFAN Engineering and Applied Sciences

Volume I

The Handbook will offer volumes of selected contributions from researchers who contribute to the scientific dissemination activity of the Universidad Autónoma de Campeche in their areas of research in Social Sciences. In addition to having a total evaluation, in the hands of the directors of the Universidad Autónoma de Campeche, the quality and timeliness of its chapters, each individual contribution was refereed to international standards (RESEARCH GATE, MENDELEY, GOOGLE SCHOLAR and REDIB), the Handbook thus proposes to the academic community, recent reports on new developments in the most interesting and promising areas of research in the Social Sciences.

Martínez-Vargas, Sergio
Figueroa-Ramírez, Sandra Jazmín
Patiño-Carachure, Cristóbal
Sierra-Grajeda, Juan Manuel

Coordinators

Engineering and Applied Sciences T-I
Handbooks

Preface

The Faculty of Engineering and Technology of the Universidad Autónoma del Carmen (UNACAR), through the Educational Program of the Master's Degree in Materials and Energy Engineering, organized the 5th Master's Student Colloquium, held from August 28 to 31, 2023. The purpose of this event was to provide a space for the dissemination of research topics of the students of the different master's and doctoral programs offered by UNACAR and other graduate programs in the region. It is important to highlight that students from the Universidad Autónoma de Campeche, the Universidad Autónoma del Estado de Morelos, the Benemérita Universidad Autónoma de Puebla, the Universidad Autónoma Metropolitana and the Centro de Investigación Científica de Yucatán - Unidad de Energía Renovable participated in the event. This Handbook "Engineering and Applied Sciences" compiles the most relevant papers presented at the 5th Master's Student Colloquium 2023, and consists of 10 chapters focused on the topics of materials, energy systems, environment, electrochemistry and corrosion, as well as modeling and numerical simulation.

MARTÍNEZ-VARGAS, Sergio
FIGUEROA-RAMÍREZ, Sandra Jazmín
PATIÑO-CARACHURE, Cristóbal
SIERRA-GRAJEDA, Juan Manuel

Content

Page

Chapter 1 Effect of leading edge spherical tubercles on the aerodynamic performance of a 2D wind turbine airfoil at low reynolds numbers using computational fluid dynamics

Capítulo 1 Análisis numérico de la influencia de las protuberancias esféricas en la eficiencia aerodinámica de un perfil 2D de turbina eólica a números de reynolds bajos

BENAVIDES-ZADOROZHNA, David Alexander†*, BENAVIDES, Olena, SIERRA GRAJEDA, Juan Manuel Tadeo, FIGUEROA-RAMÍREZ, Sandra Jazmín

Universidad Autónoma del Carmen

ID 1st Author: *David Alexander, Benavides-Zadorozhna* / **ORC ID**: 0000-0002-3240-1322, **CVU CONAHCYT ID**: 1231482

ID 1st Co-author: *Olena, Benavides* / **ORC ID**: 0000-0002-8124-0326, **CVU CONAHCYT ID**: 339830

ID 2nd Co-author: *Juan Manuel Tadeo, Sierra-Grajeda* / **ORC ID**: 0000-0002-0565-6450, **CVU CONAHCYT ID**: 219284

ID 3rd Co-author: *Sandra Jazmín, Figueroa-Ramírez* / **ORC ID**: 0000-0003-1368-1741, **CVU CONAHCYT ID**: 164797

D. Benavides, O. Benavides, J. Sierra and S. Figueroa

*120134@mail.unacar.mx

Abstract

The majority of wind power is currently produced on high wind speed sites by large wind turbine, whereas small wind turbines often operate in light wind conditions. Small capacity wind turbines have not received the same engineering attention as their large counterparts. This is partially due to a number of unique problems that small wind turbines experience. The most relevant are: low operating Reynolds number (Re<500,000) and high angles of attack. Several studies have suggested that flow control devices such as the spherical tubercle could be used to increase lift before stall and generate more power in such situations. The aim of this study is to determine the effect of tubercle amplitude on aerodynamic performance of an airfoil at low-Re numbers (Re=300,000 & Re=400,000). Three amplitudes were considered in this study: A_1=0.005c, A_2=0.01c, and A_3=0.03c. A detailed 2D simulation study is carried out using a calibrated Transition SST k-ω turbulence model to obtain aerodynamic coefficients and flow characteristics. Results indicate that small tubercles perform better overall than larger tubercles. The airfoil with the smallest tubercle outperforms the unmodified airfoil at both studied Reynolds numbers at angles of attack $0° - 4°$. The analysis of the aerodynamic coefficients indicates that the improvement of the aerodynamic performance of the airfoils with tubercles is due to the reduction of the drag coefficient. Pressure, intermittency and wall shear stress contours suggest that the overall drag reduction is achieved through the decrease of friction drag.

Computational Fluid Dynamics, Spherical Tubercles, Airfoil Simulation

Resumen

En la actualidad, la mayor parte de la energía eólica se produce en emplazamientos con vientos fuertes mediante grandes aerogeneradores, mientras que los pequeños suelen funcionar con vientos flojos. Los aerogeneradores de pequeña potencia no han recibido la misma atención técnica que sus homólogos de gran tamaño. Esto se debe en parte a una serie de problemas específicos que experimentan los aerogeneradores pequeños. Los más importantes son el bajo número de Reynolds operativo (Re<500.000) y los elevados ángulos de ataque. Varios estudios han sugerido que los dispositivos de control de flujo, como el tubérculo esférico, podrían utilizarse para aumentar la sustentación antes de la entrada en pérdida y generar más potencia en estas situaciones. El objetivo de este estudio es determinar el efecto de la amplitud del tubérculo en el rendimiento aerodinámico de un perfil aerodinámico con números de Re bajos (Re=300.000 y Re=400.000). En este estudio se consideraron tres amplitudes: A1=0,005c, A2=0,01c, y A3=0,03c. Se lleva a cabo un estudio detallado de simulación 2D utilizando un modelo de turbulencia k-ω de Transition SST calibrado para obtener los coeficientes aerodinámicos y las características del flujo. Los resultados indican que los tubérculos pequeños presentan un mejor comportamiento general que los tubérculos más grandes. El perfil con el tubérculo más pequeño supera al perfil no modificado en los dos números de Reynolds estudiados para ángulos de ataque de 0° - 4°. El análisis de los coeficientes aerodinámicos indica que la mejora del rendimiento aerodinámico de los perfiles con tubérculos se debe a la reducción del coeficiente de resistencia. Los contornos de presión, intermitencia y esfuerzo cortante de pared sugieren que la reducción global de la resistencia aerodinámica se consigue mediante la disminución de la resistencia por fricción.

Dinámica de fluidos computacional, Tubérculos esféricos, Simulación de perfiles aerodinámicos

Introduction

Flow control devices arise from the need to manipulate a flow field to achieve a specific design goal. These devices are classified as passive if they require no additional power input and active if they require additional power to operate. Passive flow control devices modify the geometric shape of the wing to manipulate the pressure gradient. Tubercles are round protrusions on the leading edge that alter the flow field around a wing. These are classified as passive flow control devices. In addition to tubercles, other passive flow control devices such as leading edge extensions, pressure surface serrations, turbulent vortex generators, flaps and flexible coatings have also been studied. In contrast, active control involves the use of additional energy to operate devices such as actuators, which are often more complex and less economically effective, but offer performance advantages over passive control methods (Hansen *et al.*, 2011).

It has been suggested that tubercles in humpback whale fins function as lift-enhancing devices. According to several researchers, the mechanism responsible for the improved aerodynamic performance is attributed to the formation of vortices along the flow, which increases momentum exchange in the boundary layer (Custodio, 2007; Johari *et al*., 2007; Miklosovik *et al*., 2004; Pedro and Kobayashi, 2008). This can lead to improvements in wing performance, such as maintaining flow stickiness for a wider range of angles of attack, stall point delay and a higher maximum lift coefficient with minimal drag penalties. Other mechanisms have been suggested, such as unequal separation properties (Fish and Lauder, 2006, Johari *et al*., 2007; Pedro and Kobayashi, 2008; van Nierop *et al*., 2008), altered pressure distribution over the wing surface (van Nierop *et al*., 2008) and vortex lift (Miklosovic and Murray, 2007). In addition, it has been suggested that the incorporation of tubercles could reduce noise.

Small wind turbines often operate in light wind conditions, where the turbine blade experiences a low Reynolds number (Re <500,000) and therefore the boundary layer over much of the suction side (top surface of the airfoil) is laminar and cannot overcome the strong adverse pressure gradient (Marty, 2014). Therefore, the boundary layer can separate and create a laminar separation bubble (LSB) where the transition from laminar to turbulent flow is triggered (Marty, 2014). Once the transition to turbulence is reached, the flow re-attaches to the surface, but in some scenarios, the separated flow may not be able to re-attach to the surface and this may lead to an early stall (Karasu *et al*., 2018). Therefore, tubercles could be used to increase lift before stall and generate more power in these situations. Measurements have already been conducted on wind turbines with tubers and have indicated that there is a potential for a substantial increase in electrical power production, leading to a higher annual energy production. The background studies to the present one have quite substantial experimental requirements. To obtain more accurate measurements of smaller scale and more sensitive flows, finer instrumentation needs to be added and the complexity of the flow needs to be increased, which can lead to additional experimental errors. Therefore, numerical experimental methods emerge as viable alternatives to experimentation. Numerical simulations are more accessible, practical, systematic and reliable.

The objective of this study is to evaluate the performance of leading edge profiles with spherical tubercles at low Reynolds numbers (Re = 300,000 and 400,000) using computational fluid dynamics. Improvements in lift-to-drag ratios were achieved for small and medium-sized tubercles at the Reynolds numbers studied. These findings support the fact that leading edge profiles with tubercles could have a practical application in small wind turbines.

Methodology and Modelling

This section discusses the creation of the geometry, the domain configuration, and the transition and turbulence model. An established and reliable airfoil within the wind energy industry is the DU93W210 airfoil (coordinates provided by (Tang, 2012)), which will have the nomenclature A0. The proposed amplitudes for the spherical tubercles are defined in terms of the chord length, and their nomenclatures are: A1 = 0.005c, A2 = 0.01c and A3 = 0.03c where the chord length is 0.6135 m.

1.   Domain design

A rectangular domain is created around the airfoil with a width equal to the airfoil width. The inlet and outlet boundaries are kept at a distance of 10c (-x) and 12c (x) from the leading edge of the airfoil. The domain extends 10c above and below the profile to avoid confinement effects. A triangular mesh is generated around the airfoil with refinement zones around the airfoil and towards the flow out of the airfoil tail. The inflation layer around the airfoil was created with the first cell height method, where the desired y^+ value was set to 0.4 to capture the viscous underlayer. Additionally, the desired y^+ value is kept the same for all angles of attack because the calculated y^+ value does not exceed the $y^+ \sim 1$ criterion. The first cell height method uses the Reynolds number based on the characteristic scales of the geometry to calculate the wall friction coefficient C_f. It is therefore important to define the characteristic scales of the geometry, in this case it would be the chord length of the airfoil; L = 0,6135 m.

El The process for calculating and defining the value of y^+ is described in detail in the literature (Leading Engineering Application Providers, 2013). The height of the first layer is set to $1,8335 \times 10^{-5}$ m, and to keep the aspect ratio below 50, the airfoil is divided into 0.0009166 m elements. Thirty layers of inflation were created around the airfoil. The mesh quality achieved through this process is almost the same for all models.

The parameters to be evaluated are: average skewness, aspect ratio and orthogonal quality for each airfoil at an angle of attack of 0∘. According to the literature presented in Fluent (2009a), the mesh quality is excellent. The number of elements is the order $2.5 - 2.6 \times 10^6$, the number of nodes $1.27 - 1.35 \times 10^6$, lhe average obliquity quality is of the order of 8×10^{-2}, the aspect ratio quality is 1.42 and, finally, the orthogonal quality is 0.95.

2.   Modelling of transition phenomena and turbulence

Developed by Menter *et al.* (2006) and Langtry *et al.* (2006b, c) the Transition SST k - ω turbulence model is used to model turbulent flows where a significant proportion of the boundary layer is laminar, this is very important for aerodynamic applications at moderate Reynolds numbers Re ($\sim$ 105). In this Reynolds number regime, a significant proportion of the boundary layer is laminar and has an effect on the solution. Modelling the transition flows and the laminar flow region near the wall is of particular importance for the wind energy industry, because wind turbine blades depend on the aerodynamic performance of the airfoil surfaces. If the airfoil is optimised to operate at low Reynolds numbers, that could lead to an increase in electrical power output, leading to a higher annual energy production (Mauro *et al.*, 2017). The Transition SST k - ω model was developed with these needs in mind. Previous work has shown excellent accuracy of the four-equation Transition SST k-ω turbulence model. The formulation is based on the well-known k - ω SST turbulence model with two additional transport equations. The first is the intermittency transport equation γ (equation (1)), which is used to trigger the transition process. The production term Pγ (eq. (2)) controls the length of the transition region, and the dissipation term Dγ dissipates the intermittency fluctuations, allowing the boundary layer to become laminar again.

$$\frac{\partial(\rho\gamma)}{\partial t} + \nabla \cdot (\rho U\gamma) = \nabla \cdot \left(\left(u + \frac{u_t}{\sigma_\gamma}\right)\nabla_\gamma\right) + P_\gamma - D_\gamma \tag{1}$$

$$P_{\gamma,1} = F_{length}c_{a1}\rho S(\gamma F_{onset})^{c_a}(1 - c_{e1}\gamma) \tag{2}$$

$$F_{onset1} = \frac{Re_v}{2.193Re_{\theta c}} \tag{3}$$

The second is the transport equation for the transition momentum thickness Reynolds number (Eq. (5)), this equation defines a transition Reynolds number based on the momentum thickness. The formulation of the Transition SST k - ω model is presented extensively in Langtry *et al.* (2006b, c) and Langtry and Menter (2005), therefore, only a brief review of what is of particular interest for this work is discussed here.

$$\frac{\partial(\rho\overline{Re}_{\theta,t})}{\partial t} + \nabla \cdot (\rho U\overline{Re}_{\theta,t}) = \nabla \cdot \left[\left(\mu + \frac{\mu_t}{\sigma_{\theta,t}}\right)\nabla\overline{Re}_{\theta,t}\right] + P_{\theta t} \tag{4}$$

$$P_{\theta t} = 0.03\frac{\rho}{t}\left(Re_{\theta,t} - \overline{Re}_{\theta,t}\right)\left(1 - F_{\theta,t}\right) \tag{5}$$

Since the proposed transport equations do not model the physics of the transition, the source term is included to enforce $\overline{Re}_{\theta t}$ to take the empirical value of $Re_{\theta t}$, (everywhere in the flow except the boundary layer, because there the source is turned off). $F_{\theta t}$ is the same as the mixing function in the turbulence model SST k − ω. Where $F_{\theta,t} = 0$ in the free stream and $F_{\theta,t} = 1$ near the wall. The Reynolds number based on the thrust thickness is a measure of the distance from the leading edge of the airfoil to a certain point on the airfoil surface. Also, since the Reynolds number is a measure of distances, there will be a Reynolds number at which the transition occurs and this is denoted by $Re_{\theta t}$.

At a certain Reynolds number based on the thickness of the impulse from the leading edge, fluctuations will start to occur, this quantity is given by $Re_{\theta c}$. The suffix c is for the Reynolds number at which turbulent fluctuations start (critical Reynolds number), and this is before the transition occurs. The use of reliable empirical relationships (source terms) is needed to accurately calculate the local values of $Re_{\theta c}$ y $Re_{\theta t}$. The fact that the turbulence model is based on empirical relationships makes it suitable for the simulation of aerodynamic surfaces at low Reynolds numbers, if appropriate values are provided (Langtry and Menter, 2005).

Furthermore, scientific literature showed that, the use of transition turbulence models, at low Reynolds numbers (Aftab and Ahmad, 2017; Benini and Ponza, 2010), is essential to obtain an adequate CFD model of the airfoil and rotor airfoil aerodynamic behaviours. Moreover, a CFD study by Mauro *et al.* (2017) demonstrates an exceptional agreement between experimental data and simulation results of the calibrated Transition SST k - ω turbulence model. The calibration of the local correlation parameters $Re_{\theta c}$ y F_{length} was achieved through a micro-genetic algorithm. Correct calibration of these parameters allows accurate prediction of stagnation and flow separation, as well as obtaining reliable lift and drag coefficients that can be used in 2D CFD models. The authors claim that the calibrated local correlations can be used for the simulation of other aerodynamic surfaces within the Reynolds number range 300,000 and 1 million. This, therefore, will give this work experimental support. $Re_{\theta c}$ y F_{length} for a given Reynolds number can be defined as (Mauro *et al.*, 2017):

$$Re_{\theta c} = 3.9592e^{-16}Re^3 - 9.598e^{-9}Re^2 + 6.884e^{-4}Re + 984.0408 \tag{6}$$

$$F_{length} = 1.7808e^{-15}Re^3 - 2.1514e^{-9}Re^2 + 8.132e^{-4}Re - 91.2135 \tag{7}$$

3.   CFD solver setup

Commercial simulation software was used to perform a steady state analysis for angles of attack of 0∘-15∘ (in steps of 2∘), considering the Transition SST k - ω model. The Transition SST k - ω model has been well tested and designed for low Reynolds number aerodynamic applications. The Transition SST k - ω model was chosen over the other turbulence models because of its ability to accurately predict boundary layer velocity and boundary layer separation. Low Reynolds number models are also necessary for accurate pressure drop or drag calculations. The Reynolds numbers studied in this work are 300,000 and 400,000. Therefore, the inlet velocity is set at 7 m/s and 9.5 m/s respectively. For all simulations, the solver was set up as a steady-state, pressure-based, ACOPLED algorithm scheme with an absolute velocity formulation. The fluid is defined as air with density equal to 1.225 kg/m³ and, dynamic viscosity $\mu = 1.7894 \times 10^{-5} \frac{N \cdot s}{m^2}$. The turbulence intensity (TI = 0.1%) and turbulent viscosity ratio (TVR = 10) were defined across the velocity boundary.

This lower TI corresponds to that of a typical low-turbulence wind tunnel and implies a natural or separation-induced transition mechanism, according to Langtry and Menter (2005) and Langtry *et al.* (2006a). A least-squares cell-based scheme was used for the spatial discretisation of the gradient, while second-order upwind schemes were used for the pressure, momentum and turbulence equations. In the steady-state coupling solver, the Courant number allows control of the sub-iteration time step. In other words, even if the steady-state solver is used, a transient sub-iteration is performed and the time scale of the simulation can be adapted to the flow time scale. In attached flow conditions, the Courant number was set to 25. At AoAs > 10∘ the instability generated by stall and vortices was noted. Under these conditions, the Courant number must be reduced to adapt the time scale so that an accurate average of the lift and drag coefficients can be obtained. A convergence criterion of O(-4) on all residuals of the dependent variables is accepted as adequate for the present airfoil simulation. To provide the local correlation parameters F_{length} y $Re_{\theta c}$, a user-defined function (UFD) in C language was written and interpreted.

Results and discussion

The behaviour of spherical tuber leading edge profiles is consistent with previous results (Aftab and Ahmad, 2017; Johari *et al.*, 2007). As anticipated, small tubercles perform more efficiently in general than tubercles with larger amplitudes. The A1 airfoil showed a minor improvement in lift-to-drag ratio from AoA 0∘-4∘ at a Reynolds number of 300,000 (Graph 1a). However, past AoA 4∘, the improvements become less noticeable and at AoA 6∘, the aerodynamic performance starts to deteriorate. Airfoil A3 showed the greatest improvement at an angle of attack of 0∘, with a 12.86 % increase in lift-to-drag ratio; beyond this angle of attack, the airfoil suffers a significant deterioration in aerodynamic performance. The A2 airfoil shows no significant improvement in lift-to-drag ratio and instead experiences an overall decrease in aerodynamic performance for all angles of attack. Note that the tubercles anticipate the peak of the lift-to-drag ratio and do not retard the stall angle in this case. The maximum lift-to-drag ratio point for the unmodified airfoil is at AoA 8∘, while for A1 the maximum lift-to-drag ratio is at AoA 6∘, and for A2 and A3 at AoA 4∘.

This is in good agreement with Johari *et al*. (2007) and Miklosovik *et al*. (2004) TLE airfoils have lower stall angles and lower maximum lift coefficients than their unmodified versions. The A1 airfoil data follow a pattern and suggest that the non-intrusive tubercles have a small reduction in lift coefficient, but a significant decrease in drag. Similar conclusions can be drawn when analysing the lift-drag ratio when Re = 400,000 (Graph 1b).

Analysis of the static pressure and intermittency contours revealed that the type of drag that has the most significant impact in this case is pressure drag. Observe Fig. 2 (a1) and (a2), as the fluid passes over the surface of the airfoil sphere A3, it initially accelerates and therefore the pressure decreases in the direction of flow. Beyond a certain point, the flow begins to decelerate and therefore the pressure in the direction of flow increases; this pressure increase is called the adverse pressure gradient and has a significant effect on the flow near the wall. The turbulence produced by the tubercle promotes momentum exchange between the boundary layers and that is why the A3 airfoil achieves a 3.31% increase in the lift coefficient at AoA 0°. As the angle of attack increases, the pressure and drag induced become more noticeable in Fig. 2 (b1) and (b2). If the pressure increase is large enough, the flow will reverse direction and, since it cannot travel backwards, due to the approaching fluid, it detaches from the surface, resulting in flow separation (Houghton *et al*., 2017). This explains why the A3 airfoil experiences such a dramatic increase in drag beyond AoA 0°. Note in Fig. 2 (a2) that the laminar flow layer remains attached to the upper surface of the airfoil, while at an angle of attack of 8° Fig. 2 (b2), the vortices produce so much turbulence that they manage to break through the laminar flow layer, resulting in flow separation.

Graph 1 Lift-drag coefficient a) Re=300,000 and b) Re=400,000
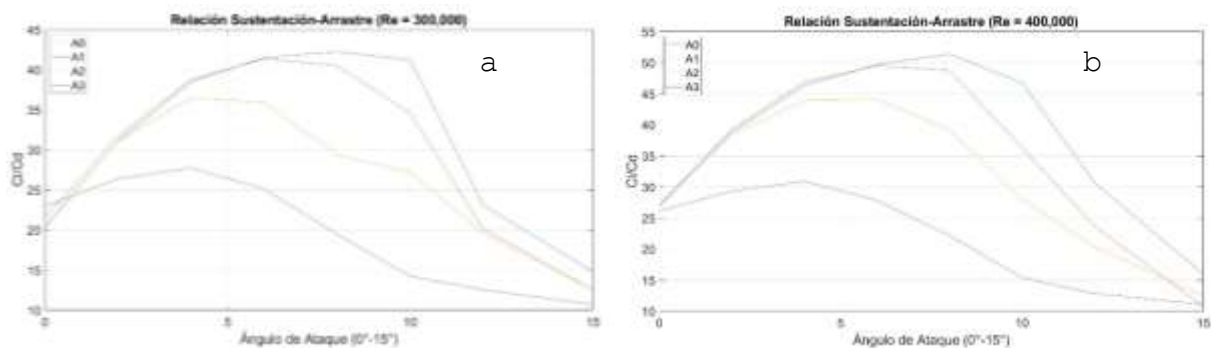
The tubercle in the A1 airfoil distributes the pressure forces in such a way that it thickens the laminar boundary layer of AoA 0° - 8°. However, this becomes less noticeable as the angle of attack increases. Due to the turbulence produced by the tubercle, the laminar flow layer is broken and the flow becomes unstable.

Graph 2 Pressure and intermittency contours for profile A3 a) AoA 0° and b) AoA 8°.
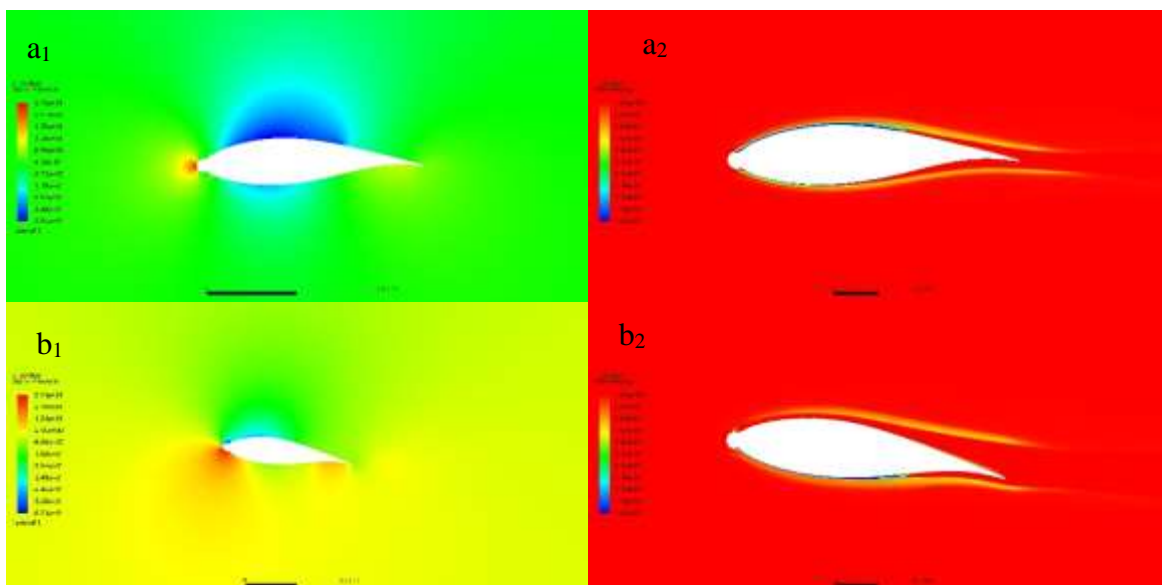
Conclusions

This paper investigated the aerodynamic performance of airfoils with spherical tubercles at the leading edges by numerical analysis of three different amplitudes and comparison with the unmodified airfoil. The Reynolds numbers studied in this work are $Re = 3 \times 10^5$ and $Re = 4 \times 10^5$. The Transition SST k - ω turbulence model was used to model the turbulence due to its ability to accurately predict the flow separation in the low Reynolds number regime, and the local correlation parameters F_{length} and $Re_{\theta c}$, were defined with the polynomial functions given by the work of Mauro *et al.* (2017). Smaller amplitude tubercles perform better overall than larger ones, but their overall efficiency does not exceed the unmodified aerodynamic surface area. The improved lift-to-drag ratio is attributed to reduced surface frictional drag. Static pressure contours, wall shear stress and intermittency contours suggest that the reduction in surface friction drag is caused by a more favourable pressure distribution around the airfoil. The correct pressure distribution allows for a thicker laminar boundary layer, which in turn helps to reduce wall frictional drag. Our work clearly has some limitations, as only a part of the full tubercle effect was studied in this paper. Despite this, our work could be the basis for developing methods to optimise tuber shape and size by providing accurate databases of aerodynamic coefficients of 2D aerodynamic surfaces with spherical tuber leading edges.

Acknowledgements

References

Aftab, S., Ahmad, K.A., 2017. CFD study on NACA 4415 airfoil implementing spherical and sinusoidal Tubercle Leading Edge. PLoS One 12 (8), e0183456. http://dx.doi.org/10.1371/journal.pone.0183456

Benini, E., Ponza, R., Laminar to turbulent boundary layer transition investigation on a supercritical airfoil using the γ -θ Transitional Model 40th Fluid Dynamics Conference and Exhibit, 28 June-1 2010, Chicago, Illinois, AIAA 2010-4289.

Custodio, D., 2007. The Effect of Humpback Whale-Like Leading Edge Protuberances on Hydrofoil Performance (M.S. Thesis). Worcester Polytechnic Inst., Worcester, MA.

Fish, F.E., Battle, J.M., 1995. Hydrodynamic design of the humpback whale flipper. J. Morphol. 225, 51–60. http://dx.doi.org/10.1002/jmor.1052250105.

Fish, F.E., Lauder, G.V., 2006. Passive and interactive flow control by swimming fishes and mammals. Annu. Rev. Fluid Mech. 38, 193–224.

Fluent, 2009a. ANSYS FLUENT 12.0 Theory Guide. ANSYS Inc., Section 6.2.2 Mesh Quality.

Hansen, K.L., Kelso, R.M., Dally, B.B., 2011. Performance variations of leadingedge tubercles for distinct airfoil profiles. AIAA J. 49 (1), 185–194. http://dx.doi.org/10.2514/1.j050631.

Houghton, E.L., Carpenter, P.W., Collicott, Steven H., Valentine, Daniel T., 2017. Chapter 1 - Basic concepts and definitions. In: Houghton, E.L., Carpenter, P.W., Collicott, Steven H., Valentine, Daniel T. (Eds.), Aerodynamics for Engineering Students, seventh ed. Butterworth-Heinemann, ISBN:9780081001943, pp. 1–86. http://dx.doi.org/10.1016/B978-0-08-100194-3.00001-8.

Johari, Hamid, Henoch, Charles, Custodio, Derrick, Levshin, Alexandra, 2007. Effects of leading-edge protuberances on airfoil performance. AIAA J. 45, 2634–2642. http://dx.doi.org/10.2514/1.28497.

Karasu, İ., Özden, M., Genç, M.S., 2018. Performance assessment of transition models for three-dimensional flow over NACA4412 wings at low Reynolds numbers. ASME J. Fluids Eng. 140 (12), 121102. http://dx.doi.org/10.1115/1.4040228.

Langtry, Robin, Gola, Janusz, Menter, Florian, 2006a. Predicting 2D airfoil and 3D wind turbine rotor performance using a transition model for general CFD codes. In: 44th AIAA Aerospace Sciences Meeting and Exhibit. AIAA 2006-395.

Langtry, Robin, Menter, Florian, 2005. Transition modeling for general CFD applications in aeronautics. In: AIAA 2005-522 43rd AIAA Aerospace Sciences Meeting and Exhibit.

Langtry, R.B., Menter, F.R., Likki, S.R., Suzen, Y.B., Huang, P.G., Volker, S., 2006b. A correlation-based transition model using local variables – Part I: model formulation In: Vienna, ASME Paper No. ASME-GT2004-53452.

Langtry, R.B., Menter, F.R., Likki, S.R., Suzen, Y.B., Huang, P.G., Volker, S., 2006c. A correlation-based transition model using local variables – Part II: test cases and industrial applications. ASME J. Turbomach. 128 (3), 423–434.

Leading Engineering Application Providers, 2013. Tips & Tricks: Estimating the first cell height for correct Y+. Available at: https://www.computationalfluiddynamics.com.au/tips-tricks-cfd-estimate-first-cellheight/.

Marty, J., 2014. Numerical investigations of separation-induced transition on high-lift low-pressure turbine using RANS and LES methods. Proc. Inst. Mech. Eng. A 39, ff. http://dx.doi.org/10.1177/0957650914548741ff, ffhal01080267f.

Mauro, S., Lanzafame, R., Messina, M., et al., 2017. Transition turbulence model calibration for wind turbine airfoil characterization through the use of a Micro-Genetic Algorithm. Int. J. Energy Environ. Eng. 8, 359–374. http://dx.doi.org/10.1007/s40095-017-0248-2.

Miklosovic, D.S., Murray, M.M., 2007. Experimental evaluation of sinusoidal leading edges. J. Aircr. 44, 1404–1407.

Miklosovik, D.S., Murray, M.M., Howle, L.E., Fish, F.E., 2004. Leading edge tubercles delay stall on humback whale flippers. Phys. Fluids 16 (5), L39–L42. http://dx.doi.org/10.1063/1.1688341.

Pedro, H.T.C., Kobayashi, M.H., 2008. Numerical study of stall delay on Humpback whale flippers. In: Proceedings of 46th AIAA Aerospace Sciences Meeting and Exhibit, 7-10th January, Reno, Nevada.

Tang, Xinzi, 2012. Aerodynamic Design and Analysis of Small Horizontal Wind Turbine Blades (Ph.D. thesis). University of Central Lancashire, UK, Available at: http://clok.uclan.ac.uk/7127/1/Tang%20Xinzi%20Final%20eThesis%20%28Master%20Copy%29.pdf.

van Nierop, Ernst, Alben, Silas, Brenner, Michael, 2008. How bumps on whale flippers delay stall: An aerodynamic model. Phys. Rev. Lett. 100, 054502

Chapter 2 Modeling of a cascaded Raman fiber optic laser

Capítulo 2 Modelización de un láser Raman de fibra óptica en cascada

PAGES-PACHECO, Angeles Yolanda†[1], DE LA CRUZ-MAY, Lelio[1], MEJIA-BELTRAN, Efrain[2] and FLORES-GIL, Aaron[1]

[1]*Universidad Autónoma del Carmen, Facultad de Ingeniería, Campus III, Avenida Central S/N, Esq. con Fracc. Mundo Maya, C.P. 24115, Ciudad del Carmen, Campeche, México.*
[2]*Centro de Investigación en Óptica, Lomas del Bosque 115, Colonia Lomas del Campestre, C.P. 37150, León, Guanajuato, México.*

ID 1st Author: *Angeles Yolanda, Pages-Pacheco* / **ORC ID**: 0000-0003-4535-7161, **CVU CONAHCYT ID**: 1005832

ID 1st Co-autor: *Lelio, De la Cruz-May* / **ORC ID**: 0000-0003-3918-0582, **CVU CONAHCYT ID**: 75160

ID 2nd Co-author: *Efraín, Mejía-Beltrán* / **ORC ID**: 0000-0001-8960-6604, **CVU CONAHCYT ID**: 20998

ID 3rd Co-author: *Aaron, Flores-Gil* / **ORC ID**: 0000-0002-2302-2056, **CVU CONAHCYT ID**: 121166

A.Pages, L. De la Cruz, E. Mejía and A. Flores

*institucional 060803@mail.unacar.mx

Abstract

We present a simulation that predicts the phenomenon of Stimulated Raman Scattering (SRS) by continuous wave (CW) laser in silica optical fibers for commercial use in telecommunications. Based on differential equations that describe the generation of Stokes, we also propose a constant that adjusts to the pumping depletion, which is related to Rayleigh backscattering. By introducing this constant into the equations describing the Stokes generation, the results of the numerical simulations approximated the experimental results by 97%.

Numerical modeling, fiber optic Raman laser, SRS, Rayleigh backscattering

Resumen

Presentamos una simulación que predice el fenómeno de la dispersión Raman estimulada (SRS) por láser de onda continua (CW) en fibras ópticas de sílice para uso comercial en telecomunicaciones. Basándonos en ecuaciones diferenciales que describen la generación de Stokes, proponemos también una constante que se ajusta al agotamiento de bombeo, la cual está relacionada con la retrodispersión de Rayleigh. Al introducir esta constante en las ecuaciones que describen la generación de Stokes, los resultados de las simulaciones numéricas se aproximaron en un 97% a los resultados experimentales.

Modelización numérica, Láser Raman de fibra óptica, SRS, Retrodispersión de Rayleigh

Introduction

The Stokes cascade generation in silica optical fibers is a nonlinear process that is based on the Raman process. This happens when radiation from a monochromatic optical light source of a specific wavelength propagates along the optical fiber, where the greatest amount of power is transferred but a small amount is scattered with a new wavelength (commonly 10^{-6}) (Agrawal, 2013). From this Raman scattering, the stimulated Raman scattering (SRS) is generated, which can be understood as the amplification of one of the wavelengths of the spontaneous Raman scattering (Blow & Wood, 1989) (in our study with a shift of ~60nm). This SRS or Stokes, grows like a laser signal and manages to store enough energy to generate spontaneous Raman scattering within the fiber, which with the increase in the power of the pump beam, generates the second Stokes, this successive process generates a Cascading Raman laser.

Fiber Raman lasers in cascades allow efficient laser operation for almost any wavelength, obtaining Stokes components that cover regions applicable to industry, medicine, military, communications, laser spectroscopy and materials processing such as cutting, welding, ablation, among others. (Supradeepa *et al*., 2017). Currently, the generation of a better wavelength shift has been achieved through special fibers with dopants such as boron and germanium, which have a large number of applications since they favor Raman scattering due to their generation of multiple Stokes lines, but They are very difficult to implement, because they have little robustness, poor quality (stability) due to their fragility and are excessively expensive (Mears *et al*., 1985). However, with the appropriate configuration and the correct design it is possible to obtain acceptable results with the use of silica fibers commonly used in telecommunications since they have an efficient Raman gain coefficient, reducing costs in their applications.

Research on the optimization of the Raman laser with silica fiber is very successful and there are analytical equations that describe the phenomenon of energy transfer between the Stokes components and the pump (Islam, 2004), however, a total energy transfer is not achieved. pumping to the first Stokes, but there is a remainder which we call pumping exhaustion. There is still a lack of studies on the effect of pump depletion that cannot be converted into Stokes waves. In various simulations (Vatnik *et al*., 2011, 2012) the energy transfer during the Stokes generation generates a power depletion as indicated (Agrawal, 2013), which does not agree with the published experimental results.

Nowadays, theoretical and experimental studies demonstrate that active media typically exhibit optical phenomena that can significantly affect cascade Raman generation. One of them is Rayleigh backscattering which occurs when a fraction of the light that is scattered is back reflected back to the beginning of the fiber within the optical waveguide (Turitsyn *et al*., 2014).

This can occur in any optical fiber and in all wave bands, having a strong compression effect on the laser linewidth that results in a decrease, broadening and shift of the wavelength in the spectrum of the coupled power after from undergoing Rayleigh backscattering (Zhu *et al*., 2014). Therefore, an adequate study is necessary in the analysis of the set of equations that appropriately predicts the Stokes generation and offers us the possibility of optimizing the laser performance by making fairly good predictions about the energy use of the Raman effect in conventional fibers to manufacture lasers.

In this study, we perform a numerical simulation based on experimental results obtained on commercial silica fibers used in telecommunications. Applying differential equations that predict the generation of Stokes considering the proposal of a constant that limits the power transfer that intervenes between the pumping and the appearance of the Stokes, which is related to Rayleigh backscatter, achieving agreement with the experimental data.

Numerical model

So far, only a few articles have been dedicated to the theoretical description of the properties of fiber Raman lasers. Most of these works present results from numerical modeling of spectral behavior. The simplest model describes the evolution of pump power and signal power along a fiber, z, and can be modeled by coupled equations, respectively. The classical non-cascade SRS process with CW pumping is expressed through the differential equations of Equation (1) (AuYeung & Yariv, 1979; Peng *et al*., 2019):

$$\frac{dP_P^+}{dz} = -\alpha_P P_P^+ - \frac{v_P}{v_S}\frac{g_{RP}}{A_{eff}} P_P^+ (P_S^+ + P_S^-)$$

$$\frac{dP_S^+}{dz} = -\alpha_S P_S^+ + \frac{g_{RS}}{A_{eff}} P_S^+ (P_P^+)$$ (1)

$$\frac{dP_S^-}{dz} = \alpha_S P_S^- - \frac{g_{RS}}{A_{eff}} P_S^- (P_P^+)$$

Where P_P^+, P_S^+ *and* P_S^- represent the pumping and Stokes powers, respectively (superscripts + and − indicate forward and backward propagation);α_P *and* α_S are the fiber attenuations for the pump wave and Stokes wave, respectively; g_{RP} *and* g_{RS} are the Raman gain coefficients for pumping and Stokes, respectively; *A* represents the effective Stokes area in the fiber and z refers to the position along the axis of the optical fiber.

However, these equations are not sufficient to detail the correct relationship of the SRS, so it is necessary to consider the cascade effect of the Stokes by adding to the previous formulas elements that will develop the energy exchange that occurs between the pumping and the Stokes. An improvement in the approximation of the differential equations would be as follows for 3 Stokes (Ecuación (2)) (Chen *et al*., 2020):

$$\frac{dP_P^+}{dz} = -\alpha_P P_P^+ - \frac{\lambda_{S1}}{\lambda_P}\frac{g_{RP}}{A_{effp}} (P_P^+ - \alpha_{Rp})(P_{S1}^+ + P_{S1}^-)$$

$$\frac{dP_{S1}^+}{dz} = -\alpha_{S1} P_{S1}^+ + \frac{g_{RS1}}{A_{effp}} P_{S1}^+ (P_P^+ - \alpha_{Rp}) - \frac{g_{RS1}}{A_{effs1}}\frac{\lambda_{S2}}{\lambda_{S1}} (P_{S1}^+ - \alpha_{Rs1})(P_{S2}^+ + P_{S2}^-)$$

$$\frac{dP_{S1}^-}{dz} = \alpha_{S1} P_{S1}^- - \frac{g_{RS1}}{A_{effp}} P_{S1}^- (P_P^+ - \alpha_{Rp}) + \frac{g_{RS1}}{A_{effs1}}\frac{\lambda_{S2}}{\lambda_{S1}} (P_{S1}^- - \alpha_{Rs1})(P_{S2}^+ + P_{S2}^-)$$

$$\frac{dP_{S2}^+}{dz} = -\alpha_{S2} P_{S2}^+ + \frac{g_{RS2}}{A_{effs1}} P_{S2}^+ (P_{S1}^+ + P_{S1}^- - \alpha_{Rs1}) - \frac{g_{RS2}}{A_{effs2}}\frac{\lambda_{S3}}{\lambda_{S2}} (P_{S2}^+ - \alpha_{Rs2})(P_{S3}^+ + P_{S3}^-)$$ (2)

$$\frac{dP_{S2}^-}{dz} = \alpha_{S2}P_{S2}^- - \frac{g_{RS2}}{A_{effs1}}P_{S2}^-(P_{s1}^+ + P_{s1}^- - \alpha_{Rs1}) + \frac{g_{RS2}}{A_{effs2}}\frac{\lambda_{S3}}{\lambda_{S2}}(P_{S2}^- - \alpha_{Rs2})(P_{S3}^+ + P_{S3}^-)$$

$$\frac{dP_{S3}^+}{dz} = -\alpha_{S3}P_{S3}^+ + \frac{g_{RS3}}{A_{effs2}}P_{S3}^+(P_{s2}^+ + P_{s2}^- - \alpha_{Rs2})$$

$$\frac{dP_{S3}^-}{dz} = \alpha_{S3}P_{S3}^- - \frac{g_{RS3}}{A_{effs2}}P_{S3}^-(P_{s2}^+ + P_{s2}^- - \alpha_{Rs2})$$

In this case, the elements were Incorporated $P_{S1}^+, P_{S1}^-, P_{S2}^+, P_{S2}^-, P_{S3}^+, P_{S3}^-$ which correspond to the forward and backward propagation for each of the Stokes; $\lambda_P, \lambda_{s1}, \lambda_{s2}, \lambda_{s3}$ represents the wavelengths at which pumping and Stokes occur; and it was necessary to add the parameter $\alpha_{Rp}, \alpha_{Rs1}, \alpha_{Rs2}$ which represents a factor that limits the energy conversion from the pumping power to the first Stokes, and from this to the next and so on. This Rayleigh backscattering factor is observed experimentally with the shift in the wavelength of the spectrum of the residual power of the pumping, affecting the energy conversion of the residual power by restricting it and preventing it from being completely exhausted during the growth of the first Stokes, it is possible to obtain this value through the experimental results and is unique for each optical fiber with an approximate value of $e^{\wedge(-\alpha L)}$.

For the purpose of modeling the SRS, we must consider that increasing the pump power at the entrance of the optical fiber causes the pump beam to generate Raman scattering along the optical fiber, and generally, a great conversion of pump wave to Stokes waves. During this process there are three waves propagating within the fiber: a pump wave that propagates in the forward direction of the beam, which in turn generates a Stokes wave that propagates forward (in the same direction as the beam wave). pump) to the end of the optical fiber and a Stokes wave that propagates backwards, dispersing in the opposite direction to the pump wave due to the influence of the reflectivity at the end of the fiber.

Applying the set of equations (2), a simulation was developed in the Matlab software considering boundary conditions necessary to describe the propagation $P_P^+(0) = P_0$, $P_S^+(0) = RP_S^-(0)$ and $P_S^-(L) = RP_S^+(L)$; where R represents the reflectivity of the power at the end of the optical fiber. The analysis process was divided into two stages based on the boundary conditions: the first analyzes the forward propagation of the pump beam from 0 to L and the second analyzes the behavior of the backward propagation from L to 0.

Forward Propagation

This simulation proposes an analysis applying silica fibers commonly used in telecommunications such as the 1060XP fiber and the LEAF to apply it in the design of fiber optic Raman lasers, for this we take into account the length of the optical fiber, the value of the pump power and the parameters provided by the manufacturer such as numerical aperture (NA), core radius (a), fiber attenuation (αt), considering the pumping wavelength and emission of the first and second Stokes (1064nm, 1115nm and 1175nm). From these values and taking the value of the Raman gain previously proposed (de la Cruz-May *et al.*, 2013), the simulation stipulates as a starting point the injection of a fictitious photon at z=0 using the following relationship: $P = h\nu B_{eff}$, where h is Planck's constant, ν is the frequency represented by the following relationship $\boldsymbol{\nu = c/\lambda}$ for which c is the speed of light and λ is the wavelength; and B_{eff} is the bandwidth of the effective gain given by Equation (3).

$$B_{eff} = \frac{\Delta V_R}{2}\left[\frac{\pi\alpha_n A_{effn}}{g_n P(z=0)}\right]^{1/2} \qquad\qquad B(3)$$

Because ΔV_R is the full width of the Raman gain and has a value of 13.2 THz, α_n would be the fiber attenuation, g_n is the Raman gain coefficient and A_{effn} is the effective area. Taking into consideration the characteristics and technical parameters provided by the manufacturer of the optical fibers. In the forward SRS we consider initial parameters choosing the backward Stokes waves as zero for the moment. Which are described in Equation 4:

$P_0 = i$; where i is a power interval
$P_1 = h * v_1 * B_{eff1}$
$P_2 = 0$
$P_3 = h * v_2 * B_{eff2}$ $\qquad$ (4)
$P_4 = 0$
$P_5 = h * v_3 * B_{eff3}$
$P_6 = 0$

In this case P_1, P_3 and P_5 correspond to the residual pumping power, Stokes 1 and Stokes 2, respectively. These values will serve as a starting point for solving the proposed differential equations, evaluating them in an interval from 0 to L (L refers to the length of the optical fiber).

Back propagation

The next stage in the simulation is to contemplate the propagation of the retroreflected Stokes waves through their path in the fiber from L to 0. Therefore, for this stage new initial values were considered, incorporating the results obtained in Equations (4). and considering the influence of reflectivity during propagation. These are detailed as follows,

$P_{pf} = P_P^+(L)$
$P_{1f} = P_{s1}^+(L)$
$P_{1b} = R\, P_{s1}^+(L)$
$P_{2f} = P_{s2}^+(L)$ $\qquad$ (5)
$P_{2b} = R\, P_{s2}^+(L)$
$P_{3f} = P_{s3}^+(L)$
$P_{3b} = R\, P_{s3}^+(L)$

Where P_{pf} is the value of the pump power at the end of the optical fiber, $P_{1f}, P_{2f}\ and\ P_{3f}$ correspond to the power at the output of the optical fiber of the first, second and third Stokes with forward propagation respectively obtained with equations (4) and $P_{1b}, P_{2b}\ and\ P_{3b}$ represents the power at the end of the optical fiber of the first, second and third Stokes with backward propagation respectively. Due to the experimental setup, the reflectivity value is ~4% for all cases where the Stokes wave is retroreflected. Each of these parameters will be analyzed again in the differential equations (2), considering an evaluation of L to 0 as a reference to the fact that all calculations will begin at the end of the optical fiber.

For example, the following figure shows the evolution of the pumping and Stokes powers along the fiber considering the 4% reflectivity, obtained in simulation for a single Stokes in the 1060XP fiber. In Figure 1, it can be seen that the pumping power gradually decreases until it reaches a limit and stops giving up energy, remaining until the exit end of the fiber. When the energy exchange with pumping occurs, Stokes 1 increases slowly until it reaches a maximum energy level and begins to decrease; This process occurs during the forward advancement of power along the distance L in the optical fiber.

However, when analyzing the behavior of the propagation from L to 0 we can observe that the lines that correspond to the backward Stokes have a greater power compared to the forward propagation, this is the same for any of the Stokes that corresponds to what is indicated by the theory and reported by other authors (AuYeung & Yariv, 1979; Vatnik *et al.*, 2012). In the case of forward Stokes power, it reaches a maximum energy and subsequently decreases until it is exhausted, while backward Stokes power increases exponentially.

Figure 1 Pump and Stokes propagation within a 1 Km 1060XP fiber with a power of 8W
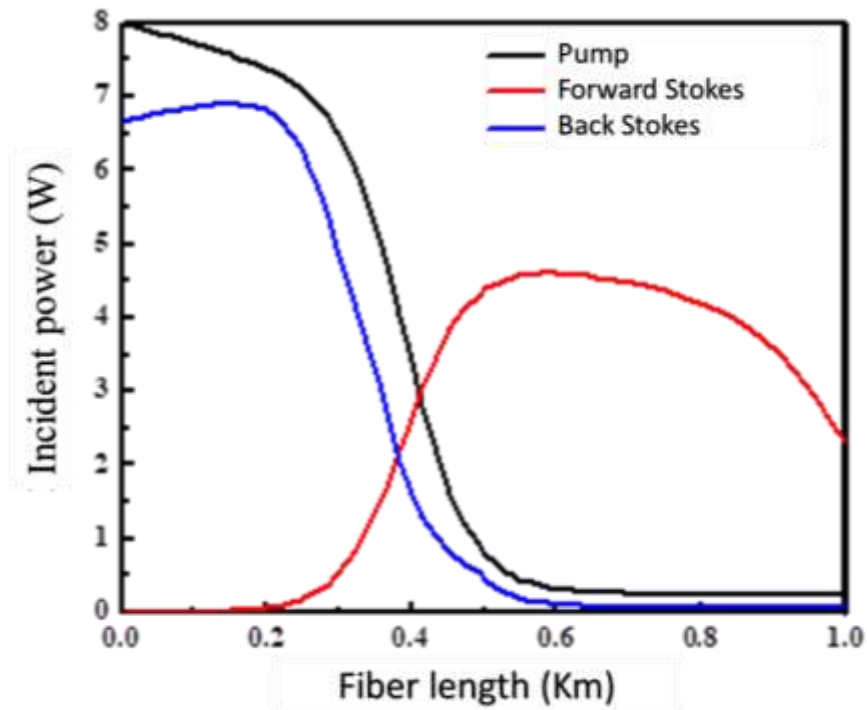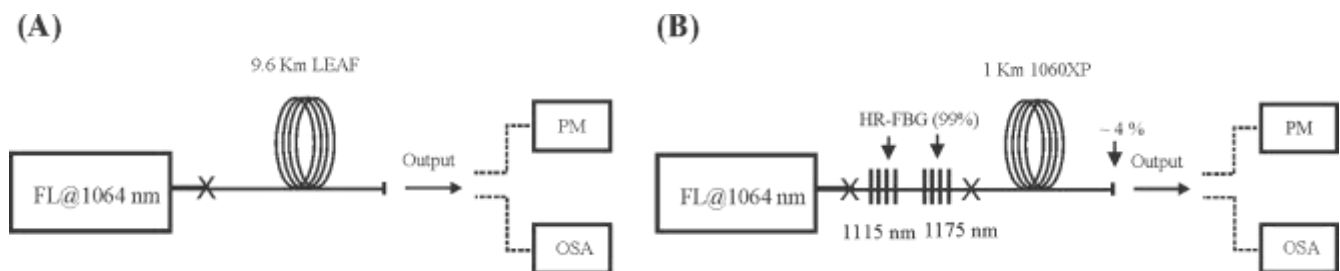

Reference Source: Own Elaboration

Analysis of results

To evaluate the reliability of the data obtained through the simulation, a comparison was made with the experimental results, considering the same technical conditions and the same coupled powers. The results show the evolution of the pumping and Stokes powers along the fiber considering the reflectivity, obtained in simulation.

The simulation provided the data generated by equations (2), managing to obtain the propagation values that were unified as follows $Residual\ power = P_p^+$, Prime Stokes Power $(P_{s1} = P_{s1}^+ + P_{s1}^-)$ and Second Stokes Power $(P_{s2} = P_{s2}^+ + P_{s2}^-)$ to obtain the final powers at the output of the optical fiber and replicate the Stokes generation.

To corroborate the efficiency of the simulation, two types of silica fibers used in telecommunications were considered: 1060XP and LEAF, both with experimental results already published in (de la Cruz May *et al.*, 2023), each with different lengths. As can be seen in Figure 2, each of them was subjected to a special configuration, the LEAF fiber was analyzed under the free running configuration and the 1060XP fiber in a configuration applying Bragg gratings with the aim of speeding up Stokes' generation. Comparing the simulation with these experimental results under specific conditions will allow us to see the scope of the simulation.

Figure 2 Experimental configuration of the study fibers: (A) 9.6 km of LEAF fiber in a free-running configuration, (B) 1 km of 1060XP fiber in a configuration with Bragg gratings
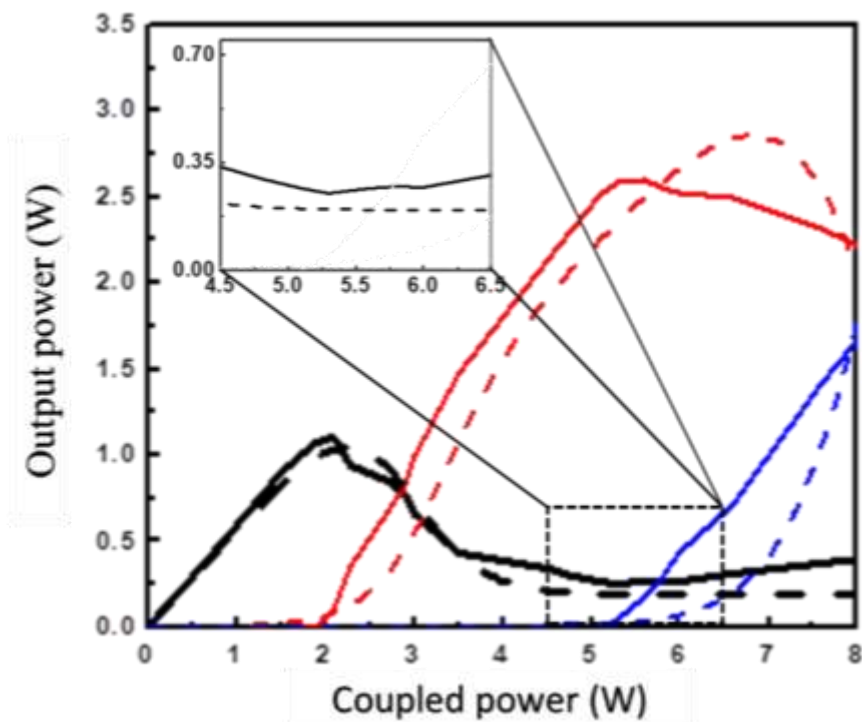

Reference Source: Own Elaboration

Based on the experimental data published on the 1060XP fiber obtained by (de la Cruz May *et al.*, 2023; Juárez-Hernández *et al.*, 2016) using a coupled power of 8 W it is possible to obtain 2 Stokes as seen in the Graph 1. When comparing with the simulation result, a 92% agreement was achieved in the Stokes generation, but the spectra obtained with the simulation present a small gap with respect to the coupled power. When analyzing pumping depletion, the constant that we introduced in the differential equations (2) was close to 80% in the closest section between the experimental line. However, the simulation for the 1060XP fiber was not able to fully reproduce the experimental results, due to the incorporation of Bragg gratings in the optical fiber, which for the development of the experiment is advantageous due to the faster obtaining of the Stokes generation; however, it causes a delay in pump depletion which could also be due to the limited length of the study fiber which turns out to be very short.

Graphic 1 Comparison of the experimental results with the simulation of the 1060XP fiber (Dashed line: simulation and Solid line: published experimental results) (de la Cruz May *et al.*, 2023): Black line corresponds to the pumping power, red to the foreground Stokes and blue to second Stokes

Reference Source:Own Elaboration

In the case study of the LEAF fiber based on the results published in (de la Cruz May *et al.*, 2023; Juárez-Hernández *et al.*, 2016), a free running configuration was used with a length even longer than in the 1060XP fiber, the comparison with the experimental data and the simulation results contemplates a coupled power of 4 W that allows the generation of the first and second Stokes as can be seen in Graph 2.
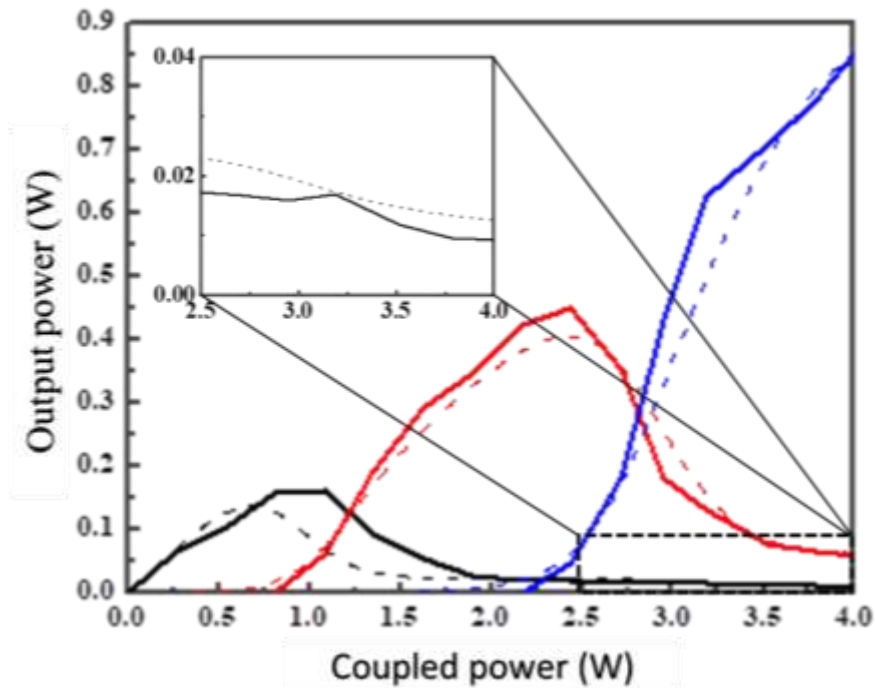
Graphic 2 Comparison of the experimental results with the simulation of the LEAF fiber (Dashed line: simulation result and Solid line: published experimental results) (de la Cruz May *et al.*, 2023): Black line corresponds to the pumping power, red to the first Stokes and blue to the second Stokes

Reference Source: Own Elaboration

With these results, we managed to reproduce the experimental results of Stokes generation for the first and second Stokes. However, there is still a gap with respect to pumping power. The results of the pumping depletion simulation in this study achieved a 99% coincidence in the closest section of the experimental line and the simulation line, considering that the experimental configuration improves the stability of the results and being a fiber of greater length it was possible to observe that not only the transfer of pumping power is restricted but that the exchange of power from the first to the Second Stokes is also affected by Rayleigh backscatter. Therefore, the incorporation of the proposed factor in equations (2) managed to adequately replicate the depletion for pumping and for the successive transfer between the Stokes.

Conclusions

We have presented a simulation that models a fiber optic Raman laser describing the SRS phenomenon, considering the interactions between the pump power with the propagation of Stokes waves towards the end of the optical fiber and the Stokes wave that is retroreflected at the beginning of the fiber. Considering already existing differential equations for the generation of the SRS in cascade for 3 Stokes, a parameter not contemplated in other publications was proposed and incorporated that is related to the influence of Rayleigh backscatter that prevents the pumping power and the Stokes from being exhausted. completely by ceding power to successive Stokes. By comparing the already published experimental results of the 1060XP and LEAF fiber with the results obtained through simulation, trying to replicate the SRS with the appropriate behavior of the power when transferring to the Stokes, it was possible to predict the generation of Stokes in 97% considering both fibers of different lengths, results that will be useful for future analyzes in the design of Raman lasers applying optical fibers for use in telecommunications. Furthermore, by incorporating the proposed parameter into our differential equations, the correct power depletion could be achieved by modeling the published experimental results with good precision, obtaining almost 100% agreement for the LEAF fiber in a free-travel configuration; although the same results could not be achieved for the 1060XP fiber by applying gratings, so it is necessary to continue working to correctly predict the SRS phenomenon for any type of silica fiber. Finally, this set of differential equations can be used to optimize the laser power, offering similar and more realistic results with respect to those obtained experimentally.

References

Agrawal, G. P. (2013). Nonlinear Fiber Optics. In *Nonlinear Science at the Dawn of the 21st Century* (pp. 195–211). Springer Berlin Heidelberg. https://doi.org/10.1007/3-540-46629-0_9 https://opg.optica.org/josab/fulltext.cfm?uri=josab-28-12-A1&id=224263

AuYeung, J., & Yariv, A. (1979). Theory of cw Raman oscillation in optical fibers. *Journal of the Optical Society of America*, *69*(6), 803. https://doi.org/10.1364/JOSA.69.000803 https://opg.optica.org/josa/abstract.cfm?uri=josa-69-6-803

Blow, K. J., & Wood, D. (1989). Theoretical Description of Transient Stimulated Raman Scattering in Optical Fibers. *IEEE Journal of Quantum Electronics*. https://doi.org/10.1109/3.40655 https://ieeexplore.ieee.org/abstract/document/40655

Chen, Y., Yao, T., Xiao, H., Leng, J., & Zhou, P. (2020). Theoretical Analysis of Heat Distribution in Raman Fiber Lasers and Amplifiers Employing Pure Passive Fiber. *IEEE Photonics Journal*, *12*(6), 1–13. https://doi.org/10.1109/JPHOT.2020.3038350 https://ieeexplore.ieee.org/abstract/document/9261093

de la Cruz May, L., Mejia Beltran, E., Benavides, O., Flores Gil, A., Pages Pacheco, A. Y., & Alvarez-Chavez, J. A. (2023). Maximum Pump Power Coupled in Raman Resonator for Maximum Power Delivered at 1115 and 1175 nm. *Photonics*, *10*(5), 531. https://doi.org/10.3390/photonics10050531 https://www.mdpi.com/2304-6732/10/5/531

de la Cruz-May, L., Mejia, E. B., Benavides, O., Vasquez Jimenez, J., Castro-Chacon, J., & May-Alarcon, M. (2013). Novel Technique for Obtaining the Raman Gain Efficiency of Silica Fibers. *IEEE Photonics Journal*, *5*(4), 6100305–6100305. https://doi.org/10.1109/JPHOT.2013.2271900 https://ieeexplore.ieee.org/abstract/document/6552987

Islam, M. N. (2004). Raman amplifiers for telecommunications: physical principles to systems. *Active and Passive Optical Components for WDM Communications IV*. https://doi.org/10.1117/12.580682 https://www.spiedigitallibrary.org/conference-proceedings-of-spie/5595/0000/Raman-amplifiers-for-telecommunications-physical-principles-to-systems/10.1117/12.580682.full?SSO=1

Juárez-Hernández, M., Mejía, E. B., de la Cruz-May, L., & Benavides, O. (2016). Stokes-to-Stokes and anti-Stokes-to-Stokes energy transfer in a Raman fibre laser under different cavity configurations. *Laser Physics*, *26*(11), 115105. https://doi.org/10.1088/1054-660X/26/11/115105 https://iopscience.iop.org/article/10.1088/1054-660X/26/11/115105/meta

Mears, R. J., Reekie, L., Poole, S. B., & Payne, D. N. (1985). Neodymium-Doped Silica Single-Mode Fibre Lasers. *Electronics Letters*. https://doi.org/10.1049/el:19850521 https://ui.adsabs.harvard.edu/abs/1985ElL....21..738M/abstract

Peng, X., Zhang, P., Wang, X., Guo, H., Wang, P., & Dai, S. (2019). Modeling and simulation of a mid-IR 43 μm Raman laser in chalcogenide glass fibers. *OSA Continuum*. https://doi.org/10.1364/osac.2.002281 https://opg.optica.org/osac/fulltext.cfm?uri=osac-2-8-2281&id=415551

Supradeepa, V. R., Feng, Y., & Nicholson, J. W. (2017). Raman fiber lasers. *Journal of Optics*, *19*(2), 023001. https://doi.org/10.1088/2040-8986/19/2/023001 https://iopscience.iop.org/article/10.1088/2040-8986/19/2/023001/meta

Turitsyn, S. K., Babin, S. A., Churkin, D. V., Vatnik, I. D., Nikulin, M., & Podivilov, E. V. (2014). Random distributed feedback fibre lasers. *Physics Reports*, *542*(2), 133–193. https://doi.org/10.1016/j.physrep.2014.02.011 https://www.sciencedirect.com/science/article/abs/pii/S0370157314001215

Vatnik, I. D., Churkin, D. V., & Babin, S. A. (2012). Power optimization of random distributed feedback fiber lasers. *Optics Express*, *20*(27), 28033. https://doi.org/10.1364/OE.20.028033 https://opg.optica.org/oe/fulltext.cfm?uri=oe-20-27-28033&id=246691

Vatnik, I. D., Churkin, D. V., Babin, S. A., & Turitsyn, S. K. (2011). Cascaded random distributed feedback Raman fiber laser operating at 1.2 μm. *Optics Express*, *19*(19), 18486. https://doi.org/10.1364/OE.19.018486 https://opg.optica.org/oe/fulltext.cfm?uri=oe-19-19-18486&id=222349

Zhu, T., Huang, S., Shi, L., Huang, W., Liu, M., & Chiang, K. (2014). Rayleigh backscattering: a method to highly compress laser linewidth. *Chinese Science Bulletin*, *59*(33), 4631–4636. https://doi.org/10.1007/s11434-014-0603-0 https://link.springer.com/article/10.1007/s11434-014-0603-0

Chapter 3 Evaluation of the inhibition efficiency of the Coccoloba Uvífera extract, through weight loss in 1M HCl and 3.5% NaCl media

Capítulo 3 Evaluación de la eficiencia de inhibición del extracto de la Coccoloba Uvífera, mediante la pérdida de peso en los medios de 1M HCl y 3.5% NaCl

HUCHIN-CHAN, Nancy del Carmen†, FIGUEROA-RAMÍREZ, Sandra Jazmín*, SIERRA-GRAJEDA, Juan Manuel Tadeo and PORCAYO-CALDERÓN, Jesús

Universidad Autónoma del Carmen, Campus III. Facultad de Ingeniería, Avenida Central S/N.Esq. con Fracc. Mundo Maya, C.P. 24115, Ciudad del Carmen, Campeche, México

ID 1st Author: *Nancy del Carmen, Huchin-Chan* / **ORC ID**: 0000-0003-1405-4563, **CVU CONAHCYT ID**: 785518

ID 1st Co-author: *Sandra Jazmín, Figueroa-Ramírez* / **ORC ID**: 0000-0003-1368-1741, **CVU CONAHCYT ID**: 164797

ID 2nd Co-author: *Juan Manuel Tadeo, Sierra Grajeda* / **ORC ID**: 0000-0002-0565-6450, **CVU CONAHCYT ID**: 219284

ID 3rd Co-author: *Jesús, Porcayo Calderón* / **ORC ID**: 0000-0002-6943-3926, **CVU CONAHCYT ID**: 6173

N. Huchin, S. Figueroa, J. Sierra and J. Porcayo

*sfigueroa@pampano.unacar.mx

Abstract

In the present investigation, the leaf extract of Coccoloba Uvifera (CU) is obtained with the help of the ethanol solvent through the maceration process; It is implemented as a green corrosion inhibitor for 1018 steel in acid and saline solutions. The percentage of corrosion efficiency was evaluated by the weight loss method, which was carried out in two media: 1 M HCl and 3.5% NaCl at times of 27 and 258 h at room temperature. The results indicate that CU can act as an efficient corrosion inhibitor, the maximum inhibition efficiency was achieved at the concentration of 600 ppm after 27 h of immersion in both media (1 M HCl and 3.5% NaCl). The formation of the protective film retards the invasion of aggressive ions and inhibits the corrosion of carbon steel in acidic and saline environments.

Acero 1018, *Coccoloba uvifera*, Inhibition efficiency, Extracts, Weight loss

Resumen

En la presente investigación, se obtiene el extracto de la hoja *de Coccoloba Uvifera (CU)*, con ayuda del solvente de etanol por medio del proceso de maceración; se implementa como inhibidor verde de corrosión para el acero 1018 en soluciones ácidas y salinas. El porcentaje de eficiencia de corrosión fue evaluado por el método de pérdida de peso, el cual se realizó en dos medios: 1 M HCl y 3.5% NaCl en los tiempos de 27 y 258 h a temperatura ambiente. Los resultados indican que *CU* puede actuar como un eficiente inhibidor de corrosión, la máxima eficiencia de inhibición se alcanzó en la concentración de 600 ppm después de 27 h de inmersión en ambos medios (1 M HCl y 3.5% NaCl). La formación de la película protectora retarda la invasión de iones agresivos e inhibir la corrosión del acero al carbono en medios ácidos y salinos.

Acero 1018, *Coccoloba uvifera*, Eficiencia de inhibición, Extractos, Pérdida de peso

1. Introduccion

90% of the pipelines, furnaces and distillation towers that make up the structural area of the oil and gas industry, are constituted by 1018 steel (Li Pubo, 2023)which is singularized by its low maintenance and acquisition costs (Haddadi Seyyed Arash, 2019). In our environment these buildings are fickle to suffer the effect of corrosion; being an impacting factor in the industrial area. Corrosion is a phenomenon that damages the internal or external conformation of metals; it occurs due to electrochemical interaction that is generated in the environment naturally or artificially (Chaubey Namrata, 2021). The impact it has on steel leads to the degradation of the quality of the metal and the safety of structures (Salleh Siti Zuliana, 2021). Corrosion currently causes economic losses in the industrial area, damaging safety measures, environment and health. Therefore, it is necessary to implement alternatives or anti-corrosion treatments for metal that is exposed to this type of media.

Inhibitors have become known as one of the methods for the coating of metals to prevent corrosion and are classified into inorganic and organic (Zhou Zongyi, 2023); among the characteristics of inorganic inhibitors is known the high potential for inhibition in corrosive media and its composition, derived from chemicals, which generate environmental impact, health and the high cost of acquisition that maintain, prompting the search for another method that is more feasible (Zhang Yanli, 2022).

On the other hand, in recent years researchers have focused on implementing organic or green corrosion inhibitors, derived from plant extracts that are a complete mixture of various organic compounds (flavonoids, alkaloids, catechins, terpenoids, and coenzymes) that adhere and protect the metal from the effect of corrosion; In addition, they are biodegradable and have a lower acquisition cost (Oyewole Olamide, 2022) In the Gulf of Mexico there is a wide biodiversity of flora, mainly the Coccoloba Uvífera plant is identified, which is colloquially known as sea grape, this species has been used as food, ornamental and part of its stem as fuel; it is also a plant that can be found at any time of the year, facilitating its acquisition.. For this reason, in the present work, Coccoloba Uvifera (CU) extract, which is produced by the maceration process and used as a green corrosion inhibitor on 1018 steel in two media: 1 M HCl and 3.5% NaCl, is studied. The corrosion inhibition efficiency is evaluated by the weight loss technique in different exposure periods at 27 and 258 hours at room temperature.

2.   Methodology to develop

2.1.   Obtaining the extract from leaves

The leaves of Coccoloba Uvifera plant were collected in Playa Norte, Ciudad del Carmen, Campeche, cleaned with tap water, distilled water and left to dry. Then, they are cut into small fractions and placed in the oven at 70 °C for 4 days; later they are crushed in a mill and sieved with mesh No. 60. The extract is obtained by the maceration method; using 25 g of leaf powder and as a solvent (ethanol), it is left in agitation for 72 hours. The extract is placed in the rotary evaporator at 40 rpm and 60 °C. Finally, the extract is concentrated in the oven at 50°C for 3 days. The stock solution is prepared from the dried extract, ethanol and distilled water. Figure 1.1 shows the process for obtaining the extract from Coccoloba Uvifera leaves.

Figure 1.1 Process for obtaining Coccoloba Uvifera leaf extract
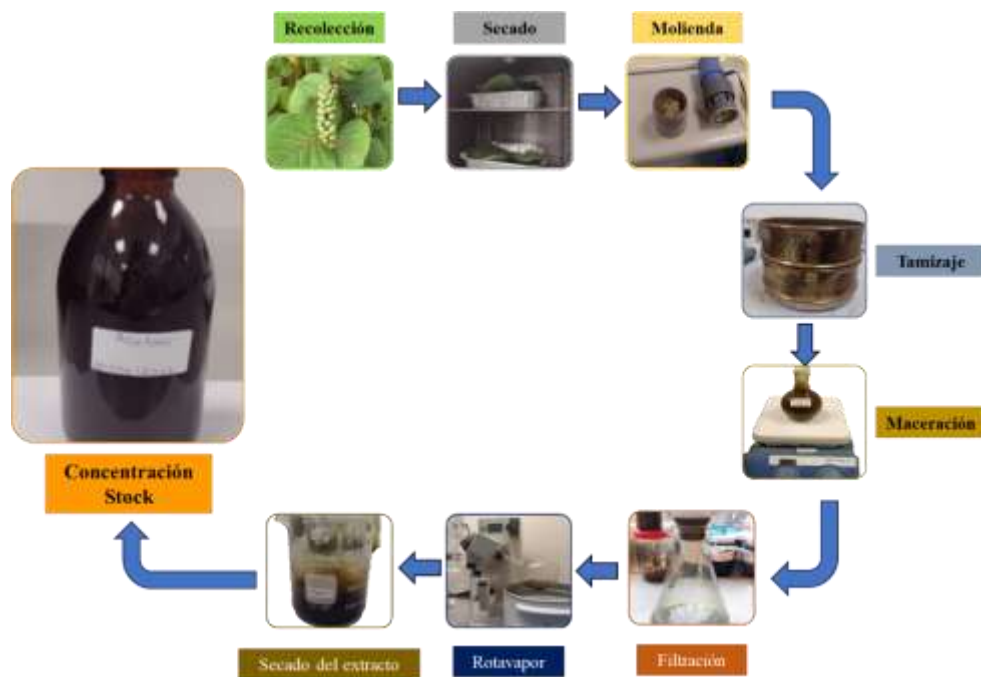
Source of Consultation: Own Elaboration.

2.2.   Specimen preparation

From a cylindrical bar of AISI 1018 steel (diameter 1 inch) the specimens are obtained, which are cut to a height of 2 cm. They are then drilled with a 1/32 drill bit, this space will allow the wire to pass through, for the development of the weight loss technique. Finally, the specimens are polished with silicon carbide sandpaper numbered 60-600 and cleaned with distilled water and acetone. The specimens are stored in a desiccator so that they do not oxidize in the environment.

2.3.   Weight loss method

Considering the ASTM G1 standard, weight loss is performed. The corrosion rate of the specimens was determined using 1 M HCl and 3.5% NaCl as corrosive medium and different concentrations of the inhibitor (200, 400, 600, 800 and 1000 ppm). The immersion time was 27 hours and 258 hours at room temperature. The test was performed in triplicate.

   The corrosion rate is obtained by means of the following equation:

$$Velocidad\ de\ corrosión\left(\frac{mm}{año}\right) = K\,\frac{\Delta W}{DAT} \tag{1}$$

   Where: K= constant $8.76\square 104$, ΔW= initial weight-final weight (g), A= the exposure area (cm2), D= density of the material (g/cm3) and T= the exposure time (h).

To calculate the inhibitor efficiency:

$$\%Eficiencia\ del\ inhibidor = \frac{Vcorr-Vinh}{Vcorr}\ x\ 100 \tag{2}$$

In which Vcorr corresponds to the corrosion rate of the specimen in acid and saline media, i.e. without inhibitor (blank) and Vinh refers to the corrosion rate of the specimen when inhibitor is present

Figure 1.2 1018 steel specimens subjected to weight loss analysis

Source Of Consultation: Own Elaboration

3. Results and discussions

3.1. Evaluation of the extract using the weight loss technique

Table 1.1 shows the comparison of the corrosion rate results (mm/year) obtained on 1018 steel using different concentrations of the inhibitor in 1 M HCl and immersion times. In both times, it is observed that as the inhibitor concentration increases, the corrosion rate decreases; it is important to note that this behavior is observed up to a concentration of 600 ppm, at higher concentrations the rate increases due to the fact that corrosion is promoted on the material. It is also observed that the longer the exposure time, the higher the corrosion rate
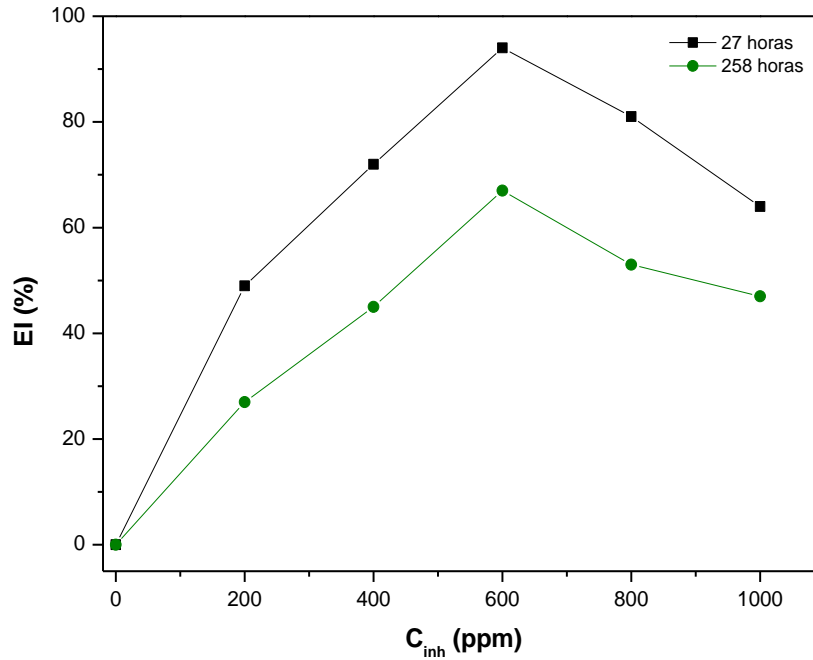
Table 1.1 Corrosion rate values obtained on 1018 steel at different concentrations of the inhibitor in 1 M HCl medium at different exposure times

Concentration (ppm)	Corrosion rate (mm/year)	
	27 horas	258 horas
0	1.49	1.26
200	0.76	0.96
400	0.42	0.67
600	0.09	0.43
800	0.28	0.58
1000	0.54	0.64

Source of Consultation: Own elaboration

Graph 1.1 shows the percentages of inhibition efficiency for 1 M HCl reveals that the percentage of efficiency for the time of 27 hours increases proportionally until reaching the concentration of 600 ppm where it obtains 93%, then it tends to decay until concluding with a percentage similar to that of the concentration of 400 ppm. On the other hand, for the exposure period of 258 h, it is perceived that the displacement takes place proportionally; being the concentration of 600 ppm the one that acquires a percentage of 67% of inhibition and begins to decrease.

Graph 1.1 Inhibitor efficiency values obtained on 1018 steel with different inhibitor concentrations in 1 M HCl
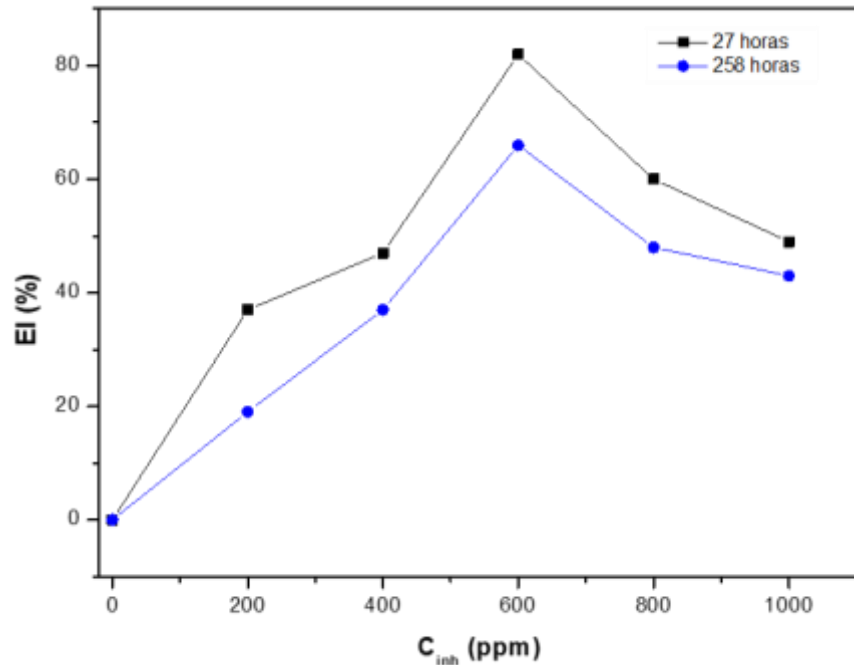

Source of Consultation: Own elaboration

On the other hand, Table 1.2 shows the results obtained in the 3.5% NaCl medium. A similar behavior to the previous case is observed, where the 600 ppm concentration shows low corrosion rate values. Comparing the results in both exposure times, lower values are observed at longer exposure times. This behavior is due to the interaction of the saline medium with the inhibitor.

Table 1.2 Corrosion rate values obtained on 1018 steel at different concentrations of the inhibitor in 3.5% NaCl medium at different exposure times

C_{inh} (ppm)	Corrosion rate (mm/year)	
	27 hours	258 hours
0	3.37	0.20
200	2.11	0.17
400	1.77	0.13
600	0.60	0.07
800	1.31	0.11
1000	1.99	0.12

Source of Consultation: Own elaboration

Graph 1.2 shows the inhibition efficiency percentages of steel 1018 in 3.5% NaCl. The behavior is very similar to the acid medium; however, in the chloride medium, slightly lower efficiencies are obtained, but the current inhibitor lasts longer, presenting values around 60% for 258 hours of exposure.

Graph 1.2 Inhibitor efficiency values obtained on 1018 steel with different inhibitor concentrations in 3.5% NaCl

Source of Consultation: Own Elaboration

In order to compare the results obtained in this study with the literature, Table 1.3 shows the inhibitor, material and the percentage of inhibition efficiencies of green extracts. It is observed that the results of the Coccoloba Uvifera extract present similar percentages to the reported extracts; therefore, it can be deduced that the ECU works as a good corrosion inhibitor for both study media.

Table 1.3 Comparison of the efficiency percentages of extracts from green inhibitors using different metals and corrosive media obtained by the weight loss technique

Inhibitor	Type of metal	Inhibition efficiency percentage (%)	
Medium: HCl			
Coccoloba Uvífera	Steel 1018	27 h	258 h
		93.6%	67.0%
Eleusine Indica (Vashishth Priya, 2022)	Iron		91.3%
Ligularia Fischeri (Prabakaran Mayakrishnan, 2016)	Mild steel		92%
Mentha Pulegium (Khadraoui A., 2016)	Carbon steel		81%
Medium: NaCl			
Coccoloba Uvífera	Steel 1018	27 h	258 h
		82.0%	66.0%
Catharanthus Roseus (Palaniappan N, 2019)	Mild steel		84.0%
Hojas de Anabasis aretioides (Berrani Assia, 2018)	Mild steel		86.0%
Raíz de Anabasis (Berrani Assia, 2018)	Mild steel		87.0%

Source of Consultation: Own Elaboration

4. Conclusions

According to the results obtained from the evaluation of the efficiency of the Coccoloba Uvifera extract by weight loss in the 1 M HCl and 3.5% NaCl media at exposure times of 27 and 258 h (at room temperature). In the acid medium, the concentration of 600 ppm presented at 27 hours of exposure an inhibition efficiency of 93%, consequently, a lower corrosion rate. At times greater than 258 hours, the efficiency was around 67%. In the saline medium, it is also observed that the 600 ppm concentration acts at a shorter exposure time; for the case of 27 hours, an inhibition efficiency of 88% is obtained and the corrosion rate of 0.60, for the case of 258 hours, an efficiency of 66% is observed; for this exposure cycle, the corrosion rate decreases. Comparing both media, it was observed that the inhibitor in chloride medium acts for a longer exposure time.

In general, it was observed that the concentration of 600 ppm is the one with the highest percentage of inhibition efficiency and minimum corrosion values in the evaluation of weight loss for these media. Likewise, it was determined that the inhibitor acts better in shorter exposure times, referring to the 27 h that were being worked, it is deduced that this is due to the fact that the evaluation was performed at laboratory level.

5.   Acknowledgments

6.   References

Berrani Assia, B. H. (2018, 10 31). Evaluation of inhibitory effect of the methanolic extract of the two parts from anabasis aretioides plant against the corrosion of E 24 steel in a neutral solution NaCl 3.5%. *Analytical and Bioanalytical Electrochemistry, 10*. Retrieved from https://www.researchgate.net/publication/328694922_Evaluation_of_inhibitory_effect_of_the_methan olic_extract_of_the_two_parts_from_anabasis_aretioides_plant_against_the_corrosion_of_E_24_steel_ in_a_neutral_solution_NaCl_35/citation/download

Chaubey Namrata, S. A. (2021, 01 01). Frontiers and advances in green and sustainable inhibitors for corrosion applications: A critical review. *Journal of Molecular Liquids*. doi:https://doi.org/10.1016/j.molliq.2020.114385

Haddadi Seyyed Arash, A. E. (2019, 06 15). A detailed atomic level computational and electrochemical exploration of the Juglans regia green fruit shell extract as a sustainable and highly efficient green corrosion inhibitor for mild steel in 3.5 wt% NaCl solution. *Journal of Molecular Liquids, 284*. doi: https://doi.org/10.1016/j.molliq.2019.04.045

Khadraoui A., K. A. (2016, 04 01). xtraction, characterization and anti-corrosion activity of Mentha pulegium oil: Weight loss, electrochemical, thermodynamic and surface studies. *Journal of Molecular Liquids, 216*. doi:https://doi.org/10.1016/j.molliq.2016.02.005

Li Pubo, S. Z. (2023, 03 01). Enhancing corrosion resistance of magnesium alloys via combining green chicory extracts and metal cations as organic-inorganic composite inhibitor. *Corrosion Communications, 9*. doi:https://doi.org/10.1016/j.corcom.2022.06.002

Oyewole Olamide, A. T. (2022, 12 01). Anti-corrosion using rice straw extract for mild steel in 1.5 M H2SO4 solution. *Results in Engineering, 16*. doi:https://doi.org/10.1016/j.rineng.2022.100684

Palaniappan N, C. I.-B. (2019, 12 10). Experimental and DFT studies on the ultrasonic energy-assisted extraction of the phytochemicals of Catharanthus roseus as green corrosion inhibitors for mild steel in NaCl medium. *Royal Society Of Chemistry*, 13. doi:: 10.1039/c9ra08971c

Prabakaran Mayakrishnan, K. S.-H.-M. (2016, 02 01). Highly efficient Ligularia fischeri green extract for the protection against corrosion of mild steel in acidic medium: Electrochemical and spectroscopic investigations. *Journal of the Taiwan Institute of Chemical Engineers, 59*. doi:https://doi.org/10.1016/j.jtice.2015.08.023

Salleh Siti Zuliana, Y. A. (2021, 07 01). lant extracts as green corrosion inhibitor for ferrous metal alloys: A review. *Journal of Cleaner Production, 304*. doi:https://doi.org/10.1016/j.jclepro.2021.127030

Seyyed Arash Haddadi, E. A. (2019). A detailed atomic level computational and electrochemical exploration of the Juglans regia green fruit shell extract as a sustainable and highly efficient green corrosion inhibitor for mild steel in 3.5 wt% NaCl solution. *ELSEVIER*, 18. doi:https://doi.org/10.1016/j.molliq.2019.04.045 0167-7322/©

Vashishth Priya, B. H. (2022, 11 01). Thermodynamic and electrochemical investigation of inhibition efficiency of green corrosion inhibitor and its comparison with synthetic dyes on MS in acidic medium. *Journal of Molecular Liquids, 365*. doi:https://doi.org/10.1016/j.molliq.2022.120042

Zhang Yanli, Q. Y. (2022, 09 01). Inhibitor loaded functional HNTs modified coatings towards corrosion protection in reinforced concrete environment. *Progress in Organic Coatings, 170*. doi:https://doi.org/10.1016/j.porgcoat.2022.106971

Zhou Zongyi, M. X. (2023, 03 01). A novel green corrosion inhibitor extracted from waste feverfew root for carbon steel in H2SO4 solution. *Results in Engineering, 17*. doi:https://doi.org/10.1016/j.rineng.2023.100971

Chapter 4 Development of chemometric models to predict physical and chemical properties in biodiesel-diesel mixtures

Capítulo 4 Desarrollo de modelos quimiométricos para predecir propiedades físicas y químicas en mezclas biodiesel-diésel

RODRIGUEZ-PEREZ, Osniel Lázaro†*, ANGUEBES-FRANSESCHI, Francisco, ABATAL, Mohamed and MAY-TZUC, Oscar Jesús

Universidad Autónoma del Carmen, Campus III, Facultad de Ingeniería, Avenida Central S/N, Esq. con Fracc. Mundo Maya, C.P. 24115, Ciudad del Carmen, Campeche, México.

ID 1st Author: *Osniel Lázaro, Rodríguez-Pérez* / **ORC ID:** 0009-0000-7889-4508, **CVU CONAHCYT ID:** 1165367

ID 1st Co-author: *Francisco, Anguebes-Franseschi* / **ORC ID:** 0000-0002-5364-1165, **CVU CONAHCYT ID:** 217824

ID 2nd Co-author: *Mohamed, Abatal* / **ORC ID:** 0000-0003-2479-8769, **CVU CONAHCYT ID:** 203026

ID 3rd Co-author: *Oscar Jesús, May-Tzuc* / **ORC ID:** 0000-0001-7681-821, **CVU CONAHCYT ID:** 627799

Abstract

Renewable energies are necessary to cushion the warming of the earth; biodiesel can be used as a substitute for diesel, with the advantage that it is friendly to the environment. At present, the analyzes carried out on biodiesel by conventional methods are expensive and harmful to the environment. Therefore, the objective of this work is to build calibration models to predict properties of biodiesel and biodiesel-diesel mixtures based on Raman spectroscopy. The physical and chemical properties of biodiesel and blends were determined in accordance with ASTM D 6751 and EN 14214 standards, which were: free acidity index, flash point, density, specific gravity at 29.5 °C, °API density, weight specific, kinematic viscosity at 40°C and freezing point. For the construction of the models, the MATLAB numerical software was used together with its artificial neural network computational package. Model training was performed with 70% of the data, while the remaining 30% were used for testing and validation. The statistical criteria used for the accuracy of the chemometric models were the root mean square error (RMSE), mean absolute percentage error (MAPE) and the correlation coefficient (R^2). The results of the correlation coefficients between the real and predicted values obtained for each chemometric model were higher than 0.99%. The predictive capacity of the chemometric models was evaluated using the t-student test of paired data, where the t-student (tc) confidence values of each model were within the range of external validation (tv= ± 2.11). The results of the t-student demonstrate the predictive reliability of the models to determine the values of the physical and chemical properties carried out by the conventional methods indicated in the ASTM D6751 and EN 14214 standards.

Biodiesel, Diesel-biodiesel mixtures, Physicochemical properties, Raman spectroscopy and chemometric models

Resumen

Las energías renovables son necesarias para amortiguar el calentamiento de la tierra; el biodiesel puede emplearse como sustituto del diésel, con la ventaja que es amigable con el medio ambiente. En la actualidad los análisis realizados al biodiesel por métodos convencionales son costosos y perjudiciales con el medio ambiente. Por esto, el objetivo de este trabajo es construir modelos de calibración para predecir propiedades de biodiesel y mezclas de biodiesel-diésel fundamentado en la espectroscopia Raman. Las propiedades físicas y químicas del biodiesel y mezclas se determinaron conforme a las normas ASTM D 6751 y EN 14214, las cuales fueron: el índice de acidez libre, punto de inflamación, densidad, gravedad específica a 29.5 °C, densidad °API, peso específico, viscosidad cinemática a 40°C y punto de congelación. Para la construcción de los modelos se utilizó el software numérico MATLAB en conjunto de su paquete computacional de red neuronal artificial. El entrenamiento de los modelos se realizó con el 70 % de los datos, mientras que el 30 % restante se destinaron para las pruebas y validación. Los criterios estadísticos utilizados para la precisión de los modelos quimiométricos fueron el error cuadrático medio (RMSE), error de porcentaje absoluto medio (MAPE) y el coeficiente de correlación (R^2). Los resultados de los coeficientes de correlación entre los valores reales y predichos obtenidos para cada modelo quimiométrico fueron superiores al 0.99%. La capacidad de predicción de los modelos quimiométricos fue evaluada mediante la prueba *t-student* de datos apareados, donde los valores de confianza *t-student* (tc) de cada modelo estuvieron dentro del rango de validación externa (tv= ± 2.11). Los resultados del *t-student* demuestran la confiabilidad de predicción de los modelos para determinar los valores de las propiedades físicas y químicas realizadas por los métodos convencionales indicados en las normas ASTM D6751 y EN 14214.

Biodiesel, Mezclas diésel-biodiesel, Propiedades fisicoquímicas espectroscopia Raman y Modelos quimiométricos

1. Introduction

Currently, the main driver for the development of research on alternative energy sources is the urgent need to mitigate global warming and its consequences for living beings. For this, CO2 reduction is fundamental, since high concentrations of this greenhouse gas (GHG) are the main consequence of global warming [1]. However, the technologies that emit this type of gas are still economically unfeasible to eliminate. The power generation sector has a significant potential to reduce CO2 emissions, as it is responsible for almost 37.5 % of CO2 emissions worldwide [1].

A vital role can be played by renewable energy resources in reducing CO2 emissions. According to El-Sharkawy *et al*. [2] it is mentioned that if the share of renewable energy increases by 39 % by 2050 in combination with electricity generation, CO2 emissions can be reduced by up to 50 %. Currently, most of the world's energy demand is met by fossil fuels such as oil, coal and natural gas. Among the most consumed petroleum derivatives is diesel, which is widely used in transportation, agriculture, construction and power generation. However, the rapid rate of depletion of fossil oil, as well as environmental degradation due to vehicular and industrial pollution that directly affects the stable global ecosystem, has led to the search for new solutions to replace conventional diesel. Among the most viable alternatives to replace petrodiesel is biodiesel, which is a renewable fuel, biodegradable, non-toxic, does not alter the carbon cycle, has high lubricity and its characteristics are very similar to those of conventional diesel. This biofuel is a mixture of long-chain fatty acid esters (C14-C20), which is manufactured by the transesterification reaction of vegetable oils or animal fats with an alcohol in the presence of a catalyst. Also, its sulfur content is lower than the standard limit of conventional diesel, this being one of its main advantages, both for environmental care and for the life of combustion engines [3] [4]. Something very favorable is its miscibility with diesel, which allows blends of these two fuels in any proportion. Biomixes also emit less GHG when burned compared to conventional diesel [5]. Because of this, biodiesel production increased by 700% between 2005 and 2015 [6], reaching a global production of 48.3 billion liters in 2019 and demand in 2022 reached a record 170 billion liters, surpassing the levels observed in 2019 before the Covid-19 pandemic [7] [8].

The commercialization and use of biodiesel depend on its physicochemical properties, which are determined by specification limits depending on the type of regulation in the region being used. For example, standards have been established in the United States (ASTM D6751), Europe (EN 14214), Brazil, South Africa, Australia and other parts of the world. Both ASTM D6751 and EN 14214 efficiently detail biodiesel specifications, and these standards are commonly used as a reference or basis for other standards and their analyses. However, the conventional methods used to determine the physicochemical properties of biodiesel are slow and expensive, some are not accessible in some facilities, are environmentally destructive, and can cause human injury.
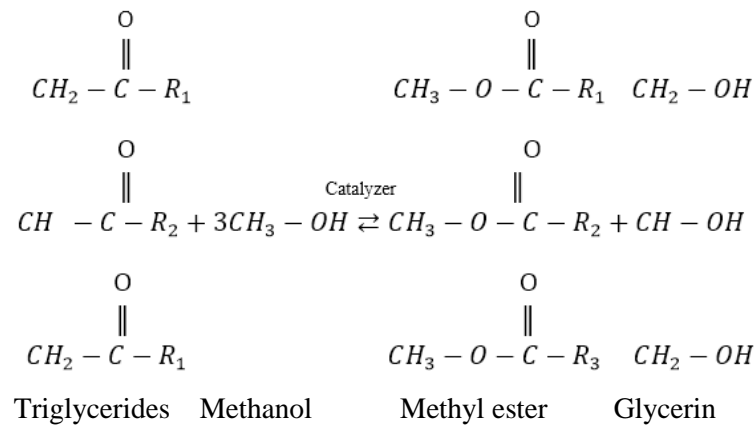
Therefore, this work is focused on determining in a different way the physicochemical properties of biodiesel, in a simple, non-destructive way and with a high level of accuracy. Consequently, chemometric models will be developed through artificial intelligence based on Raman spectroscopy, which have the priority of predicting properties such as: free acidity index, copper strip corrosion at 40 °C and 100 °C, sulfated ash content, flash point, density, specific gravity at 29.5 °C, density °API, specific weight, kinematic viscosity at 40°C and freezing point, complying with the established standards of ASTM D 6751 and EN 14214.

2. Materials and Methods

2.1 Materials

The materials used in this study were methanol (99.9% purity), phenolphthalein and sodium hydroxide (98.3%). The raw materials were chicken fat and pork fat. Chicken fat and skin were purchased from a chicken stand at a price of $5.00 MX per kilogram (kg) and washed thoroughly with tap water to remove debris such as blood, viscera, and bones. It was then cut into small pieces to be melted in a container at a temperature of 110°C for 5 hours (h); the solid components of the lipid fraction of the fat (glycerides) were then separated in a fine mesh strainer. On the other hand, the pork fat used for the preparation of biodiesel was acquired through a butcher's shop at a price of $40.00 MX per kg. Then, it was heated in a DIDADEC TECHNOLOGIE model CDF/010 tray dryer at 50 °C to reduce its viscosity.

For the transesterification of both biodiesels, an automated batch reactor, Didatec model RQ-DT-135/EL, was used. Animal fats (chicken fat and pork fat) were used as raw material, methanol was used as solvent and a sodium hydroxide (NaOH) catalyst, which were homogenized, forming sodium methoxide (CH3O-Na+). The presence of a catalyst is necessary to increase the reaction rate and yield of the transesterification process. In the industry the main catalysts used are alkaline catalysts (NaOH and KOH), thanks to the fact that they have very good solubility in methanol and their price is quite low in the market [9]. The reaction conditions were: 4 hours of duration, at a temperature of 56 ℃ and an agitation speed of 450 rpm. The chemical reaction of transesterification is shown in Figure 2.1.

Figure 2.1 Chemical reaction of biodiesel transesterification

$$CH_2 - \overset{\overset{\textstyle O}{\|}}{C} - R_1 \qquad\qquad CH_3 - O - \overset{\overset{\textstyle O}{\|}}{C} - R_1 \quad CH_2 - OH$$

$$CH\ \ - \overset{\overset{\textstyle O}{\|}}{C} - R_2 + 3CH_3 - OH \overset{\text{Catalyzer}}{\rightleftarrows} CH_3 - O - \overset{\overset{\textstyle O}{\|}}{C} - R_2 + CH - OH$$

$$CH_2 - \overset{\overset{\textstyle O}{\|}}{C} - R_1 \qquad\qquad CH_3 - O - \overset{\overset{\textstyle O}{\|}}{C} - R_3 \quad CH_2 - OH$$

Triglycerides   Methanol   Methyl ester   Glycerin

Source: (S. Rezania et al., 2019)

When the time of the reaction was finished, the mixture was extracted in 2 test tubes of 1000 ml and 2000 ml; leaving it to rest for 12 h; after which, and after settling the mixture, it was possible to differentiate the fatty acid methyl ester from the glycerin. Next, the fatty acid methyl ester and the glycerin were separated in different containers. Then, the fatty acid methyl ester was washed with distilled water using a 1000 ml separatory funnel to remove the remaining glycerol residues in the mixture. Two filtration methods were used to eliminate suspended solids; the first was gravimetric filtration with 11 µm Whatman paper and then with Purolite rigth 10 ion exchange resin. As mentioned above, biodiesel is a biofuel that is completely miscible with conventional diesel and its mixtures in any of its proportions have the possibility of improving the qualities of the fuel. The proportions used to prepare the diesel-biodiesel blends were: D-10, D-20, D-40, D-50, D-60, D-80, D-90. The nomenclature of the blends represents the percentage by mass of diesel and the remainder is the percentage by mass of biodiesel; for example, D-10 is defined as 10 percent diesel and 90 percent biodiesel. These blends were performed on an Ohasus brand digital pelletizing balance, with an uncertainty of ± 0.2 g.

2.2 Physicochemical análisis

The physicochemical properties of the diesel-biodiesel samples were determined in accordance with established standards and methods (ASTM D6751 and EN14214). The properties determined for the blends were: free acid number, copper strip corrosion at 40 °C and 100 °C, sulfated ash contents, flash point, density, specific gravity at 29.5 °C, density °API, specific weight, viscosity and freezing point. A detailed description of the procedure for obtaining each physicochemical property will be given below.

2.2.1 Free acid number

The acidity index was determined using method EN 14104 of Standard EN14214, which uses an alcoholic solution as titrant and phenolphthalein as color indicator. A method very similar to the one mentioned is the simple green visual method, which is the one used in this work to obtain the values of the acid number. The acid number is defined as the amount of milligrams of KOH or NaOH (mg) necessary to neutralize the free fatty acids present in one gram of oil or fat and is a measure of the degree of hydrolysis of a fat [10].

2.2.2 Flash point

The flash point is determined from the ASTM D-92 method, which is similar to the ASTM D-93 method of ASTM D6751. This method called "Cleveland open cup", defines the flash and ignition temperatures of all petroleum products, except those fuels that have an open cup flash temperature below 79°C and below 400°C. Approximately 70 ml of test sample is placed in a test vessel. The temperature of the vessel is rapidly increased by means of a burner and then the flame is controlled to generate a slower temperature rise steadily as the flash point is approached [11].

2.2.3 Density, specific gravity, API density and specific weight

These properties are determined using the ASTM D 1298 method of ASTM 6751. The method describes how to perform the analyses of density, specific gravity, API density and specific gravity. At present, density meters are reliable and efficient equipment to obtain the analyses described above. For this reason, the Anton Paar DMA 4100M density meter was used to analyze these properties.

2.2.4 Kinematic viscosity at 40 °C

The kinematic viscosity was specified according to ASTM D 445 of ASTM D 6751. Kinematic viscosity can be measured based on the time measurement of a known volume of sample flowing under gravity, passing through a calibrated glass capillary tube (viscometer) at ambient conditions [12]. Also, kinematic viscosity is related to dynamic viscosity through density. Having the value of the dynamic viscosity, the kinematic viscosity of a fluid can be calculated, observe the following Equation (Eq.1):

$$v = \frac{\mu}{\rho} \tag{1}$$

where:
v: kinematic viscosity
μ: dynamic viscosity
ρ: density

The results of the kinematic viscosity analysis for each mixture were obtained from Eq. 1, where the dynamic viscosity is analyzed with the Anton Paar Physica MCR 101 rheometer and the density with the Anton Paar DMA 4100M density meter.

2.2.5 Freezing point

The freezing point is determined using the ASTM D 97 method of the ASTM D 6751 standard, for which a wide-mouth container is taken and ice and salt are placed inside. Then, test tubes with biodiesel and diesel-biodiesel blends are placed in the container. When the formation of solids (ice) begins in the biodiesel and the blends inside the tubes, the temperature is measured and this will be the freezing point value of that fuel [13].

2.3 Raman Spectroscopy

Raman spectroscopy is an analytical technique in the near-infrared range, based on the phenomenon of inelastic molecular vibration/rotation that causes frequency changes due to energy exchange with matter through the collision of molecules [14]. Samples of diesel-biodiesel blends were analyzed in quintuplicate using a QE65000 Raman spectrometer (Ocean Optics, Edinburgh, UK) equipped with a symmetrical cross Czerny-Turner optical bench, 101 mm focal length, an RPB 785 fiber optic test and a Hamamatsu S7031-1006 detector with a spectral range between 780 and 940 nm. The spectrometer was operated with SPECTRA SUIT software (version 2.0.162, Ocean Optics, Edinburgh, UK) to establish the interface between the computer and the Raman equipment. To perform the analysis of the samples, 30 mL of each mixture was deposited in an amber glass vial and subsequently a laser beam was applied at 785 nm with a power of 20 mW for 10 s. All Raman spectra were collected in the range of -81 to 2104 cm-1 at 25 °C. Data between 0-99 cm-1 and 1902-2104 cm-1 were omitted because they had higher spectral noise. Therefore, the spectral data between 100 and 1901 cm-1 were used.

2.4 Development of chemometric models,

For the development of the chemometric models, an experimental database was created, where the absorbances of the Raman spectra of the blends of both biodiesels (matrix X) and the results of the physicochemical properties (vector Y) were used. Microsoft Excel 2013 (Microsoft, Redmond, WA, USA) was used to create the matrices. Matrix X consisted with a composition of 850 wavelength values and 18 samples between of the diesel-biodiesel blends (15 300 absorbance samples) and matrix Y had for each physicochemical property one column and 18 samples in the rows. Subsequently, the X matrix was exported to Quasar v1.7.0 software to initially pre-process the data for a better fit.

The dimensionality of the data was then reduced using principal component analysis (PCA). The first step of the pretreatment was to minimize noise and spectral errors of the chemometric models, developed by mathematical and statistical treatments: auto-scaling and centering. Also, a first order derivative and the standard variable normalizations (SNV) and minimum-maximum (min-max) were used to achieve a greater correction of the spectrum; thus, obtaining an X-matrix transformation of 740 wavelength values and 18 samples. In the PCA, 740 wavelengths were reduced to 8 CP components with an explained variance of 97 %. For the construction, training and evaluation of the chemometric models, MATLAB numerical software was used in conjunction with its artificial neural network (ANN) Toolbox computational package (Demuth and Beale, 2021). For the predictability of the developed models, ANN employed back-propagation learning, with the Levenberg-Marquardt supervision algorithm, which has proven to be one of the most prominent in weight and bias optimization [12]. The model was trained with 70 % of the data (12 samples) and 30 % of the remaining data (6 samples) was used for model testing and validation. The indicators or statistical criteria used for the accuracy of the chemometric models were the root mean square error (RMSE), mean absolute percentage error (MAPE) and the correlation coefficient (R2); and the paired data T-student's test was used to evaluate the reliability of the chemometric models. Figure 2.2 shows the schematic diagram of the development of the chemometric models.

Figure 2.2 Schematic diagram of the process of development and evaluation of chemometric models for the estimation of physicochemical properties
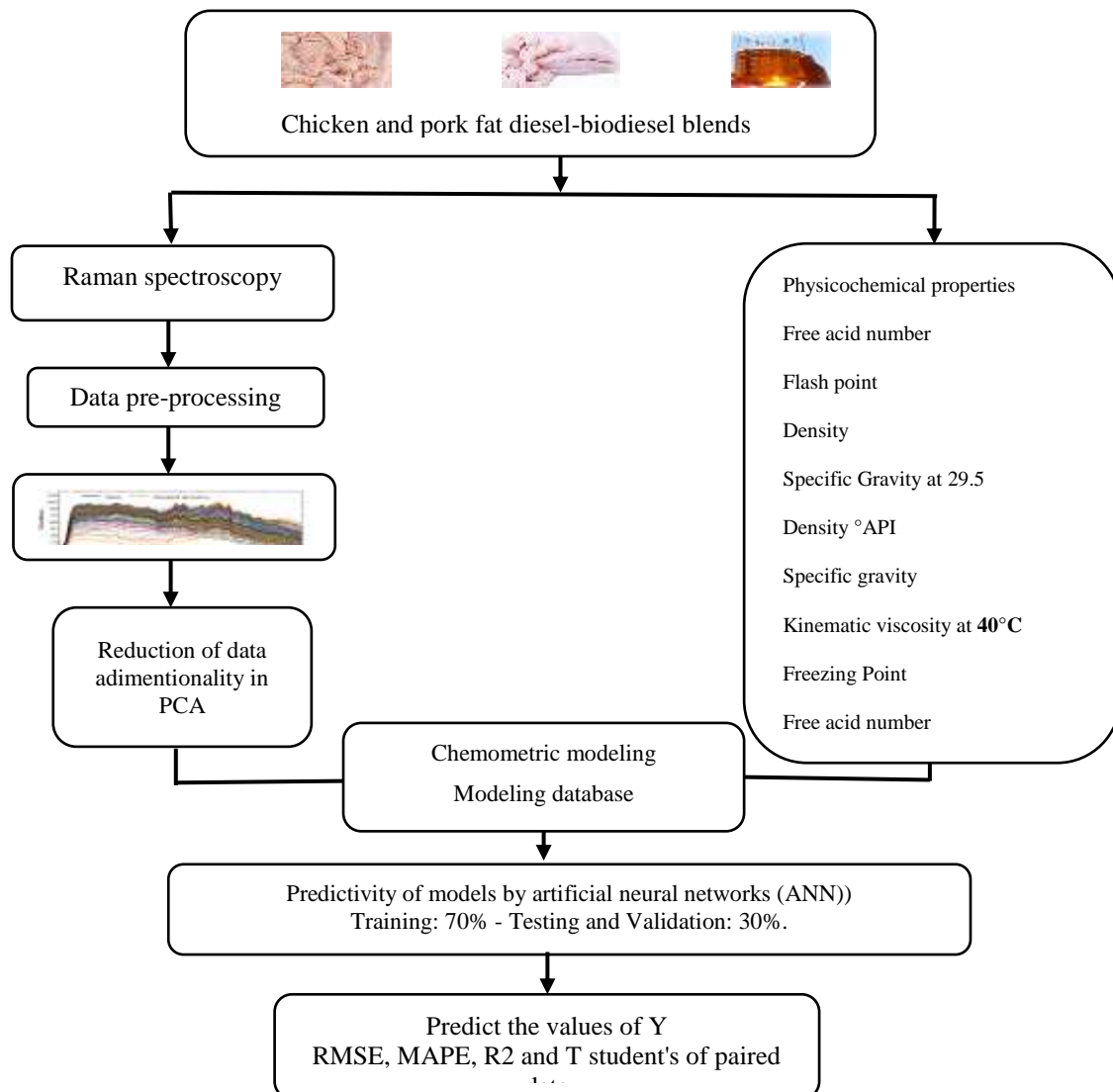
Source: Own Elaboration

3. Analysis and results

3.1 Interpretation of Raman Spectra

3.1.1 Raman spectra of chicken diesel-biodiesel blends of chicken fat.

Figure 3.1 shows that the Raman spectra obtained on the chicken fat diesel-biodiesel samples have spectral bands covering the following ranges: 260-542, 550-685, 685-711, 950-1100, 1180-1325, 1363-1447 and 1460-1750 cm-1:

The region between 260-542 cm-1 is related to the stretching and bending vibrations of C-O, C-C-O and C-C-C that form the molecular structure of fatty acid methyl ester [15].

The spectral region between 685-711 cm-1 is assigned to the stretching vibrations of C-O and C-C-O, and to the bending vibrations of O-C-O. On the other hand, the band between 711-950 cm-1 is a product of the C-C and C-H stretching vibrations present in the fatty acid methyl ester [16].

The region present between 950-1100 cm-1 is attributed to the bending vibrations of the C-H and C-O-H bonds of the fatty acid methyl ester [17].

The spectral region between 1180-1325 presents 2 peaks, these correspond to the stretching vibrations of the C-O, C-O-C bonds and the bending C-H and O-C-H vibrations [18].

The peak between 1363-1447 is due to the bending and oscillation vibrations of the C-H and O-H functional groups [18].

**Figure 3.1** Absorbance bands present in chicken diesel-biodiesel blends
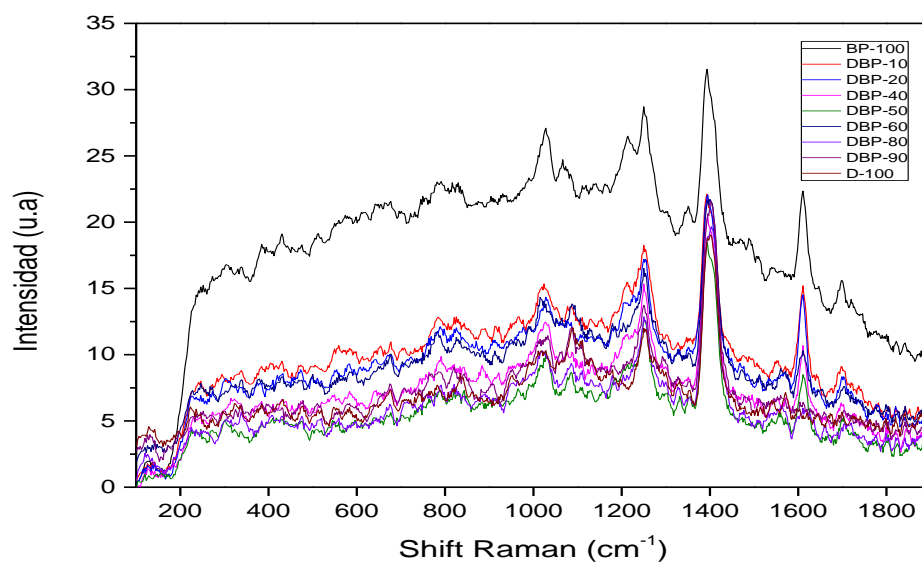
Source: Own Elaboration

Finally, the region between 1460-1750 are concerning the symmetric angular deformation of CH3, CeH, C=O axial deformation of aliphatics, saturated esters and asymmetric angular deformation in the CH2 plane, respectively [8].

3.1.1 Spectrum of pork fat diesel-biodiesel blends

Figure 3.2 corresponds to the Raman spectra of the pork fat diesel-biodiesel samples, these have spectral bands covering the ranges 750-900, 925-1140, 1186-1300, 1350-1460 and 1525-1740.

The region between 750 - 900 cm-1 is attributed to the C-C and CH stretching vibrations present in the fatty acid methyl ester [19].

Figure 3.2 Absorbance bands present in diesel-biodiesel blends of swine
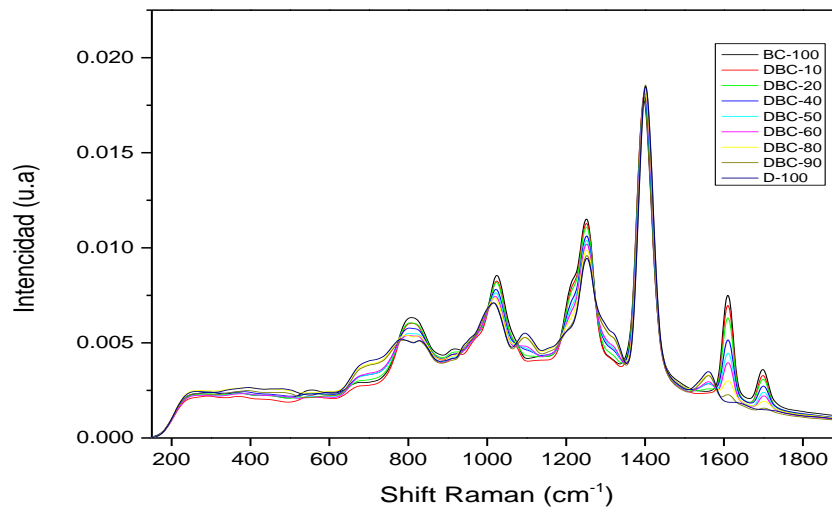
Source: Own Elaboration

The region between 925-1140 cm-1 these correspond to deformation vibrations in C-H and methylene (CH2) bonds, as well as COH bending vibrations identified in the bands 940-1074, bending vibrations of C-H and C-O-H bonds of esters, and to bending vibrations of C-N bonds of amino acids and proteins [17][18][20].

The spectral region between 1186-1300 cm-1corresponds to C-H and O-C-H vibrations, while the spectral bands 1350-1460 cm-1are due to bending and oscillation vibrations of C-H and O-H functional groups [18].

Finally, the spectral region between 1525-1740 cm-1 are due to the bending vibrations of the O-H functional group [21].

3.2 Physicochemical properties of chicken and pork fat biodiesels

The results of the conventional analyses of the physicochemical properties for the diesel-biodiesel blends are shown in Tables 3.1 and 3.2.

Table 3.1 Propiedades fisicoquímica del biodiesel de grasa de pollo y sus mezclas diésel-biodiesel

Mixtures	Acid number (mgKOH)	Flash point (°C)	Density (kg/m3)	Specific gravity 29.5°C	API density 15°C	Specific gravity	Viscosity (mm2/s)	Freezing point (°C)
$B-100$	0,340	162	878.0	0.8720	881.0	0.8800	3.35	4
$D-10$	0.310	144	871.5	0.8657	875.1	0.8731	3.27	1
$D-20$	0.280	132	865.0	0.8591	868.6	0.8665	2.69	-3
$D-40$	0.250	108	851.8	0.8459	855.5	0.8534	2.67	-5
$D-50$	0.200	100	846.0	0.8399	849.6	0.8475	2.38	-6
$D-60$	0.170	96	843.9	0.8379	847.6	0.8454	2.37	-7
$D-80$	0.140	90	829.0	0.8228	832.8	0.8305	1.70	-10
$D-90$	0.060	84	823.5	0.8172	827.2	0.8250	1.68	-12
$D-100$	0.056	78	816.9	0.8110	820.7	0.8180	1.54	-14

Source: Own Elaboration

Table 3.2 Physicochemical properties of pork fat biodiesel and its diesel-biodiesel blends

Mixtures	Acid number (mgKOH)	Flash point (°C)	Density (kg/m3)	Specific gravity 29.5°C	API density 15°C	Specific gravity	Viscosity (mm2/s)	Freezing point (°C)
$B - 100$	0,310	160	870.0	0.8640	874.0	0.8720	3.67	11
$D - 10$	0.250	142	868.6	0.8625	872.3	0.8702	3.49	8
$D - 20$	0.220	124	862.2	0.8561	865.8	0.8637	3.19	6
$D - 40$	0.200	108	850.3	0.8441	854.0	0.8518	2.70	3
$D - 50$	0.170	100	843.1	0.8370	846.9	0.8447	2.42	1
$D - 60$	0.140	96	838.7	0.8326	842.5	0.8403	2.35	-2
$D - 80$	0.110	91	828.2	0.8220	832.0	0.8297	1.86	-7
$D - 90$	0.080	82	821.2	0.8151	825.0	0.8227	1.76	-10
$D - 100$	0.056	78	816.9	0.8110	820.7	0.8180	1.54	-14

Source: Own Elaboration

3.3 Chemometric models

3.3.1 Free Acid Number (InAc)

The InAc indicates the percentage (%) of free fatty acids in the biodiesel; this parameter corresponds to the amount of mg of KOH necessary for the neutralization of free fatty acids in one gram of fat [22]. It is very important to determine this property in the biofuel, since a high value of InAc can cause severe corrosion in internal combustion engine fuel systems [28]. The InAc obtained in chicken biodiesel (BP) and pig biodiesel (BC) were 0.34 mg KOH/g and 0.31 mg KOH/g respectively, these values are acceptable within the EN 14214 standard and were similar to [16]. For its part, the InAc of the BP had agreement with [23] [24][25], while the BC to [26] [27][28] [29][30][31].

To determine the chemometric models for each of the physicochemical properties, an analysis was made to know, with which; number of neurons would have a better fit. Five measurements were taken for each of the following neurons (n) 2, 4, 6, 8, 10 and 12, then the best of these was chosen, the selected measurements were compared and the one with the best prediction was determined. In the case of InAc the best prediction regression model was with 10n (see Table 3.3), its training (tr), validation (vl) and test (ts) statistical criteria were: R2tr=1.0000; R2vl=0.9937; R2ts=0.9975; MAPEtr=0.4194; MAPEvl=5.1968; MAPEts=2.2981; RMSEtr=0.0006; RMSEvl=0.0046 RMSEts=0.0040. The correlation coefficients between the actual and predicted values obtained in the 10n regression model, are observed in Figure 3.3, their results are: tr=0.99988, vl=0.99254, ts=0.99997 and yield (R)=0.99927. These results are superior to [32], [33] and similar to [34]

Table 3.3 Statistical criteria for chemometric models for InAc

Neurons	R^2tr	R^2vl	R^2ts	MAPEtr	MAPEvl	MAPEts	RMSEtr	RMSEvl	RMSEts
2	0.9946	0.9073	0.9633	4.9419	6.7808	6.9857	0.0069	0.0139	0.0166
4	0.9969	0.9300	0.9651	2.4173	3.7752	3.7997	0.0054	0.0093	0.0089
6	1.0000	0.9984	0.9878	0.0692	2.0431	5.6964	0.0001	0.0034	0.0089
8	0.9920	0.9949	0.9681	2.4082	1.6780	3.7489	0.0084	0.0041	0.0144
10	1.0000	0.9937	0.9975	0.4194	5.1968	2.2981	0.0006	0.0046	0.0040
12	1.0000	0.9923	0.9958	0.0066	2.8385	3.8166	0.0000	0.0061	0.0056

Source: Own Elaboration

Figure 3.3 Free acidity regression model, results of correlation coefficients: a) Training b) Validation c) Testing d) Performance
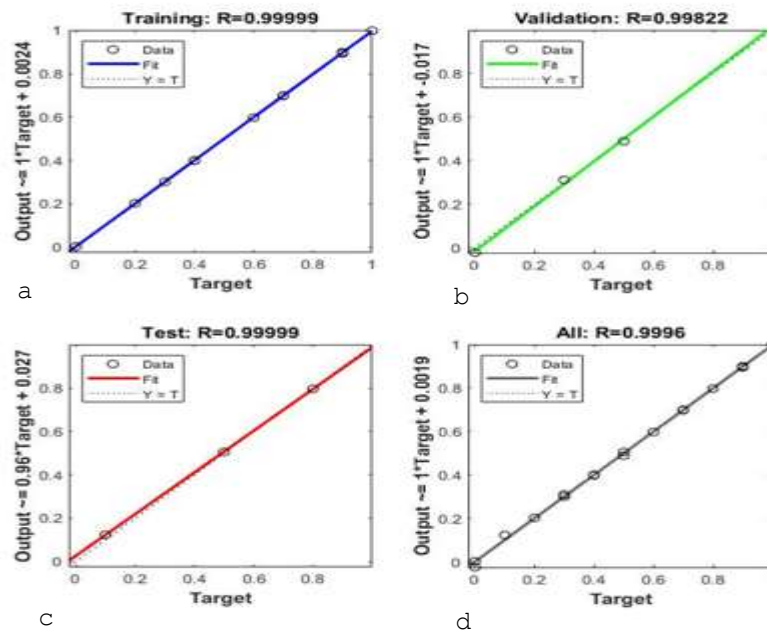
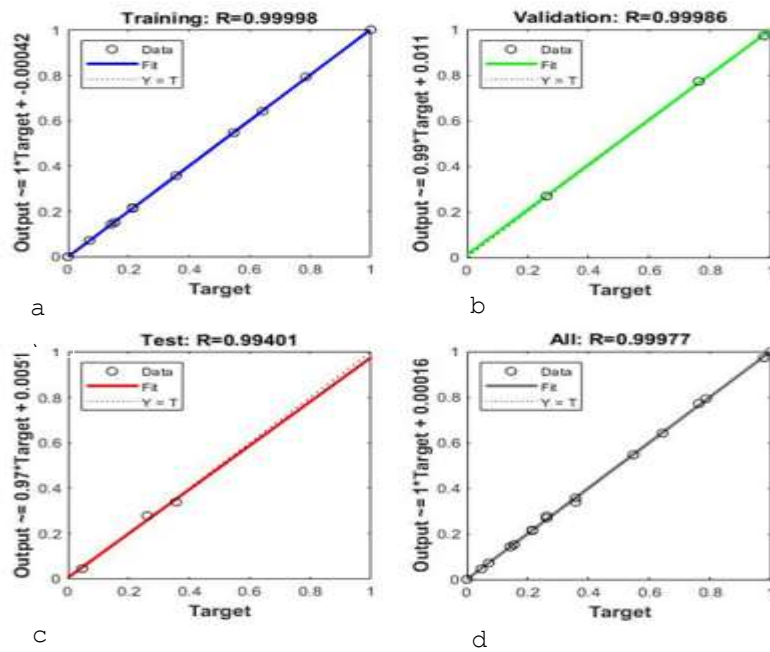*Source: Own Elaboration*

3.3.2 Flash Point (PI)

One of the advantages of biodiesel over conventional diesel is that its IP is higher, which provides greater safety for handling, transportation and storage, thus reducing the risk of fire [23], [35]. According to Kirubakara *et al.* [23] mentions that after finishing the transesterification process, methanol should be removed from the final mixture to increase the flash point temperature. The results of the PI analysis for BP and BC were 162 °C and 160 °C, respectively, which are within the permissible parameters of ASTM D 6751. The BP result was similar to [25], while for BC it was similar to [36], [37]. In the case of PI the best fit model was with 4n (see Table 3.4), showing the following statistical indicators: R2tr=0.9999; R2vl=0.9994; R2ts=0.9876; MAPEtr=0.1013; MAPEvl=0.4491; MAPEts=0.7159; RMSEtr=0.2083; RMSEvl=0.6223; RMSEts=1.2099. Figure 3.4 shows the regression model obtained with 4n, where the correlation coefficients between the actual and predicted values were: Ent=0.99988, Val=0.99254, Pb=0.99997 and R=0.99927 respectively. The model results are superior to [18][32][4][4][38][33].

Table 3.4 Statistical criteria for chemometric models for the PI

Neuronas	R^2tr	R^2vl	R^2ts	MAPEtr	MAPEvl	MAPEts	RMSEtr	RMSEvl	RMSEts
2	0.9925	0.9956	0.9991	0.9946	0.5082	0.1864	2.1871	1.0343	0.3216
4	0.9999	0.9994	0.9876	0.1013	0.4491	0.7159	0.2083	0.6223	1.2099
6	0.9991	0.9970	0.9904	0.5382	0.6243	2.0388	0.8509	0.6759	2.2110
8	0.9992	0.9987	0.9953	0.6587	0.5638	1.2461	0.7888	0.6996	1.5200
10	0.9994	0.9728	0.9875	0.5187	2.6246	2.3487	0.6065	4.3206	3.0875
12	0.9999	0.9976	0.9940	0.1366	0.9302	0.8835	0.3281	1.0011	1.2195

Source: Own Elaboration

Figure 3.6 IP regression model, results of correlation coefficients: a) Training b) Validation c) Test d) Performance

Source: Own Elaboration

3.3.3 Density, specific gravity 29.5 ºC (GE 29.5), API density (D API) and specific gravity (PE)

Density is a ratio expressed as mass per unit volume; it depends on the state of aggregation in which the substance is found and its temperature. Measuring density gives an idea of the mass content of the substance, being directly related to the energy of the fuel; the higher this value is, the better the profitability [39]. The density of biodiesel varies according to the nature of the raw material and influences the atomization efficiency [23]. The obtained values of specific gravity at 29.5 °C (GE 29.5), API density at 15°C (D API) and specific gravity (PE) are directly related to density. The density for BP and BC were 878 kg/m3 and 870 kg/m3 respectively, complying with EN 14214 standards and were similar to each other at [40][41].

Individually the density result of BP was similar to [35][42][39][23][43][44][45][46][47], while BC had agreement with [48][49][50][30]. The best fit chemometric model for density also, was with 4n (see Table 3.5), showing the following statistical criteria: R2tr=0.9985; R2vl=0.9721; R2ts=0.9972; MAPEtr=0.0512; MAPEvl=0.2060; MAPEts=0.1026; RMSEtr=0.7348; RMSEvl=1.9425; RMSEts=0.9753. Figure 3.5 shows the regression model obtained with 4n, where the correlation coefficients between the actual and predicted values were: Ent=0.99987, Val=0.99991, Pb=1 and R=0.99981. The values obtained in the model are higher than [18][32][32][51][38][33].

Table 3.5 Statistical criteria for density chemometric models.

Neuronas	R^2tr	R^2vl	R^2ts	MAPEtr	MAPEvl	MAPEts	RMSEtr	RMSEvl	RMSEts
2	0.9998	0.9998	0.9799	0.0268	0.0245	0.2610	0.3111	0.2315	2.4225
4	0.9985	0.9721	0.9972	0.0512	0.2060	0.1026	0.7348	1.9425	0.9753
6	0.9997	0.9934	0.9934	0.0293	0.1358	0.1550	0.3172	1.2116	1.5827
8	1.0000	0.9989	0.9714	0.0052	0.0662	0.2736	0.0562	0.6683	3.1331
10	0.9849	0.9341	0.9982	0.1963	0.3293	0.0863	2.2421	3.0298	0.8133
12	0.9999	0.9580	0.9951	0.0113	0.3012	0.1557	0.1456	4.0157	1.4155

Source: Own Elaboration

Figure 3.5 Density regression model, results of correlation coefficients: a) Training b) Validation c) Testing d) Performance
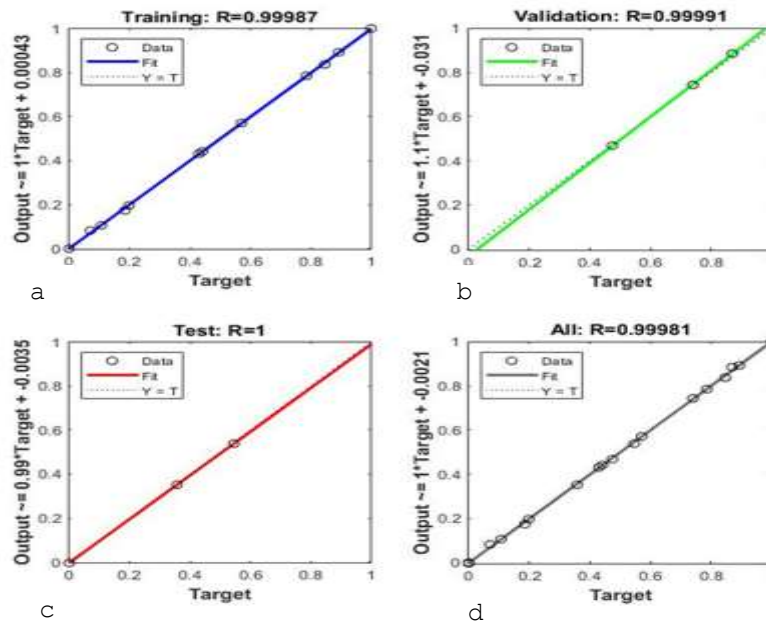
Source: Own Elaboration

The GE 29.5 results for BP and BC were 0.872 and 0.864, respectively. The chemometric model with the best fit was the 6n, reporting the following statistical criteria: R2tr=0.9997; R2vl=0.9988; R2ts=0.9943; MAPEtr=0.0245; MAPEvl=0.0550; MAPEts=0.1248; RMSEtr=0.0003; RMSEvl=0.0005; RMSEts=0.0012, see Table 3.6. The regression model obtained is shown in Figure 3.6, which shows the results of the correlation coefficients between the actual and predicted values of GE 29.5: Ent=0.99992, Val=0.99941, Pb=0.99930 and R=0.99963.

Table 3.6 Statistical criteria for chemometric models for GE 29.5 °C

Neuronas	R^2tr	R^2vl	R^2ts	MAPEtr	MAPEvl	MAPEts	RMSEtr	RMSEvl	RMSEts
2	0.9933	0.9965	0.9959	0.1030	0.1036	0.1123	0.0014	0.0009	0.0014
4	0.9998	0.9595	0.9522	0.0216	0.2234	0.1867	0.0003	0.0020	0.0024
6	0.9997	0.9988	0.9943	0.0245	0.0550	0.1248	0.0003	0.0005	0.0012
8	0.9999	0.9980	0.9504	0.0119	0.0932	0.6056	0.0001	0.0009	0.0055
10	0.9987	0.9986	0.9919	0.0466	0.0715	0.1828	0.0006	0.0007	0.0023
12	0.9964	0.9499	0.9911	0.0983	0.2807	0.1456	0.0012	0.0026	0.0017

Source: Own Elaboration

Figure 3.6 Regression model of GE 29.5, results of the correlation coefficients: a) Training b) Validation c) Testing d) Performance
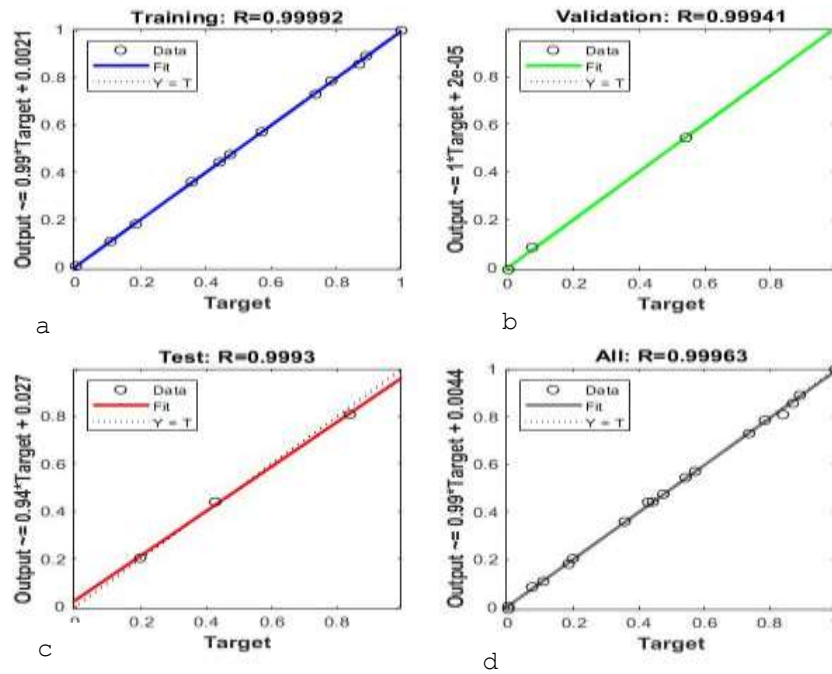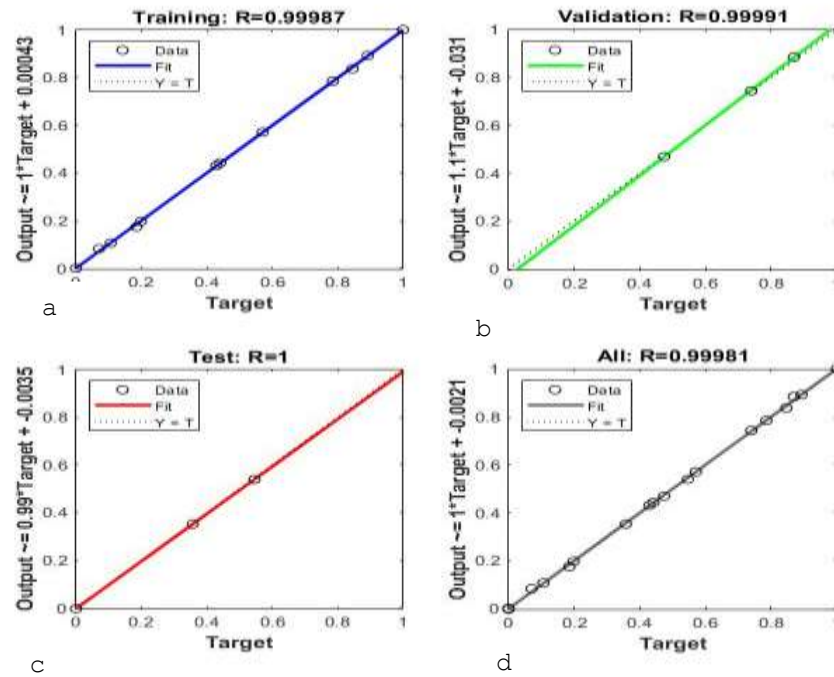

Source: Own Elaboration

The results of the analyses for D API for BP and BC were 881 °API and 874 °API respectively; the highest statistical criterion of the chemometric models was with 12n, with a fit of: R2tr=0.9997; R2vl=0.9964; R2ts=0.9994, MAPEtr=0.0238; MAPEvl=0.0587; MAPEts=0.0377; RMSEtr=0.3321; RMSEvl=0.6048; RMSEts=0.3361 (see Table 3.7). Figure 3.7 represents the regression model obtained for 12n, showing the results of the correlation coefficients between the actual and predicted values: Ent=0.99987, Val=0.99991, Pb=1 and R=0.99981.

Table 3.7 Statistical criteria of the chemometric models for D-API

Neuronas	R^2tr	R^2vl	R^2ts	MAPEtr	MAPEvl	MAPEts	RMSEtr	RMSEvl	RMSEts
2	1.0000	0.8523	0.9742	0.0046	0.2096	0.3322	0.0550	1.7900	3.0628
4	0.9858	0.9984	0.9603	0.0866	0.0662	0.1541	2.4164	0.6686	1.7198
6	1.0000	0.9901	0.9956	0.0001	0.0847	0.1286	0.0009	0.7845	1.5948
8	1.0000	0.9648	0.9992	0.0055	0.5066	0.0600	0.0538	5.0751	0.5385
10	1.0000	0.9956	0.9836	0.0042	0.1368	0.1414	0.0558	1.2156	1.6253
12	0.9997	0.9964	0.9994	0.0238	0.0587	0.0377	0.3321	0.6048	0.3361

Source: Own Elaboration

Figure 3.7 D-API regression model, results of correlation coefficients: a) Training b) Validation c) Testing d) Performance
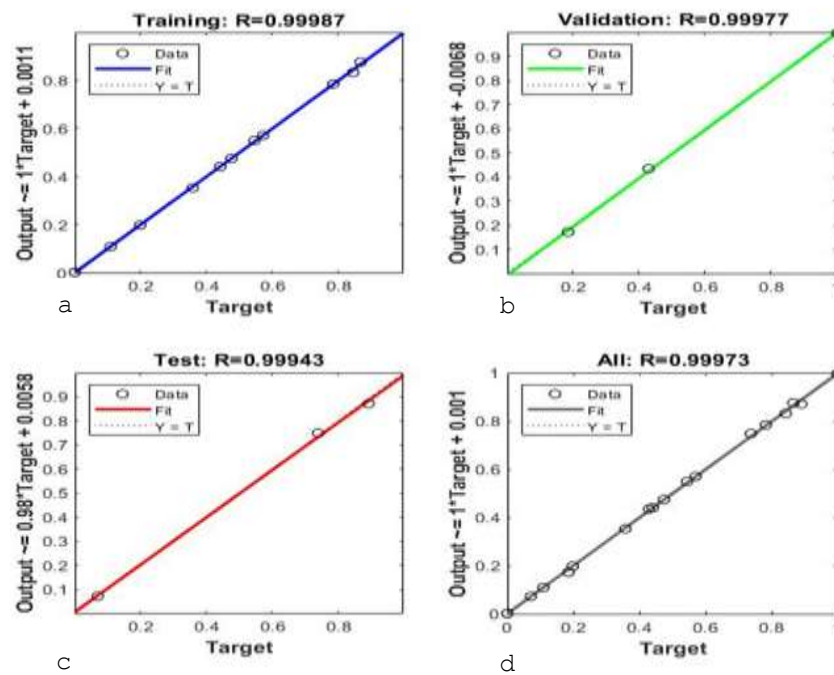

Source: Own Elaboration

The PE for BP and BC was 0.880 and 0.872 respectively; the chemometric model that showed the best statistical criteria was the 10n, with the following values: R2tr=0.9997; R2vl=0.9994; R2ts=0.9986, MAPEtr=0.0224; MAPEvl=0.0548; MAPEts=0.0773; RMSEtr=0.0003; RMSEvl=0.0005; RMSEts=0.0008 (see Table 3.8). The 10n regression model is depicted in Figure 3.8, where the correlation coefficients between the actual and predicted values are defined: Ent=0.99987, Val=0.99977, Pb=0.99943 and R=0.99973

Table 3.8 Statistical criteria of the chemometric models for PE.

Neuronas	R^2tr	R^2vl	R^2ts	MAPEtr	MAPEvl	MAPEts	RMSEtr	RMSEvl	RMSEts
2	0.9997	0.9821	0.9842	0.0311	0.1413	0.2671	0.0003	0.0013	0.0027
4	1.0000	0.9929	0.9867	0.0037	0.1157	0.2489	0.0000	0.0013	0.0023
6	0.9987	0.9813	0.9821	0.0662	0.1438	0.2618	0.0007	0.0017	0.0029
8	0.9979	0.9983	0.9658	0.0775	0.0408	0.4593	0.0009	0.0005	0.0045
10	0.9997	0.9994	0.9986	0.0224	0.0548	0.0773	0.0003	0.0005	0.0008
12	1.0000	0.9979	0.9877	0.0084	0.0904	0.1461	0.0001	0.0009	0.0015

Source: Own Elaboration

Figure 3.8 PE regression model, results of correlation coefficients: a) Training b) Validation c) Testing d) Performance

Source: Own Elaboration

### 3.3.4 Kinematic Viscosity at 40ºC (VCa40ºC)

The kinematic viscosity is one of the most important properties, since it affects the atomization of the fuel in the combustion chamber and, with it implies the formation of carbon residues in the engine [39]. The viscosity of biodiesel is mainly influenced by the experimental conditions and the magnitude of the transesterification reaction. Therefore, it is the main reason why fats and oils are transesterified to biodiesel, since this process significantly reduces this property [23]. The VCa40ºC of both biodiesel met the parameters of ASTM D 6751 and their values were 3.35 mm2/s and 3.67 mm2/s for both BP and BD. The VCa40ºC result for BP was similar to [24][44][23], while for BC it was [29][31]. For VCa40ºC the best fitting chemometric model was with 10n, which showed the following statistical prediction criteria: R2tr=0.9997; R2vl=0.9639; R2ts=0.9991, MAPEtr=0.2598; MAPEvl=3.2887; MAPEts=1.0709; RMSEtr=0.0109; RMSEvl=0.0635; RMSEts=0.0250 (see Table 3.9). Figure 3.9 shows the 10n regression model, numerically explaining the actual and predicted values of the correlation coefficients: Ent=0.99988, Val=0.99254, Pb=0.99997 and R=0.99927. The model values are higher than [18] [32] [32] [52] [51] [51] [3] [27] and similar to [53].

Table 3.9 Statistical criteria of chemometric models for VCa40ºC.

Neuronas	R^2tr	R^2vl	R^2ts	MAPEtr	MAPEvl	MAPEts	RMSEtr	RMSEvl	RMSEts
2	0.9997	0.9989	0.9947	0.3259	0.9939	1.4828	0.0128	0.0232	0.0450
4	0.9985	0.9962	0.9972	0.8441	1.5894	1.3159	0.0244	0.0414	0.0428
6	0.9995	0.9825	0.9521	0.5016	1.3561	2.9474	0.0169	0.0423	0.0900
8	0.9994	0.9989	0.9915	0.4864	0.5917	2.5321	0.0161	0.0144	0.0538
10	0.9997	0.9639	0.9991	0.2598	3.2887	1.0709	0.0109	0.0635	0.0250
12	0.9993	0.9832	0.9983	0.4604	1.3628	1.5344	0.0160	0.0518	0.0400

Source: Own Elaboration

Figure 3.9 Regression model of VCa40°C, results of the correlation coefficients: a) Training b) Validation c) Testing d) Performance
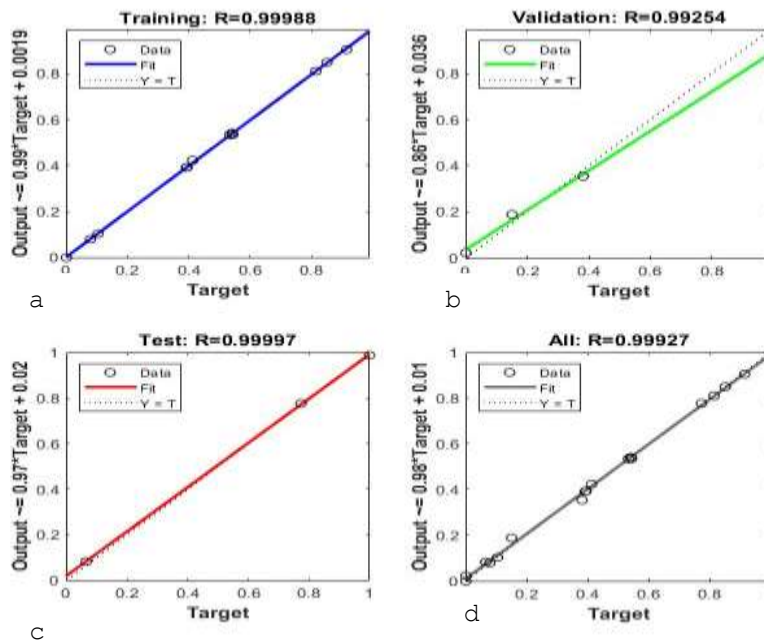
Source: Own Elaboration

3.3.5   Punto de congelación (PC)

The PC is the temperature at which a substance in a liquid state becomes a solid state [54]. At this point, the biofuel becomes semi-solid and loses the ability to flow freely. The impurities present without purification are the main cause that raise the pour point [23]. The PC for BP and BC were 4 °C and 11 °C, showing results of temperatures that are not favorable for the winter season [55]. The BP result agreed with [41][37] [46] while BC was similar to [36], [56].

The chemometric model that showed the highest accuracy for CP was de10n, with the statistical indicators: R2tr=0.9999; R2vl=0.9985; R2ts=0.9989, MAPEtr=-0.2702; MAPEvl=2.3893; MAPEts=0.5172; RMSEtr=0.0630; RMSEvl=0.2439; RMSEts=0.2131 (see Table 3.10). Figure 3.10 shows the correlation coefficients between the actual and predicted values of the regression model for 10n, showing the following results: Ent=0.99998, Val=0.99979, Pb=0.99996 and R=0.99986. The results of the PC model exceed [32][53].

Table 3.10   Statistical criteria for chemometric models for PC

Neuronas	R^2tr	R^2vl	R^2ts	MAPEtr	MAPEvl	MAPEts	RMSEtr	RMSEvl	RMSEts
2	0.9833	0.9985	0.9949	-1.7303	2.9711	-0.0051	0.7811	0.4158	0.3549
4	0.9979	0.9633	0.9748	6.6122	-17.877	-11.541	0.2924	1.0418	1.6706
6	0.9997	0.9971	0.9955	2.6554	-3.6504	-10.311	0.1250	0.4824	0.4660
8	0.9974	0.9993	0.9867	-1.5480	2.2415	5.8914	0.3541	0.2202	0.7317
10	0.9999	0.9985	0.9989	-0.2702	2.3893	0.5172	0.0630	0.2439	0.2131
12	0.9990	0.9974	0.9907	-0.7183	14.9598	20.9216	0.2201	0.3564	0.5797

Source: Own Elaboration

Figure 3.10 PC regression model, results of correlation coefficients: a) Training b) Validation c) Testing d) Performance
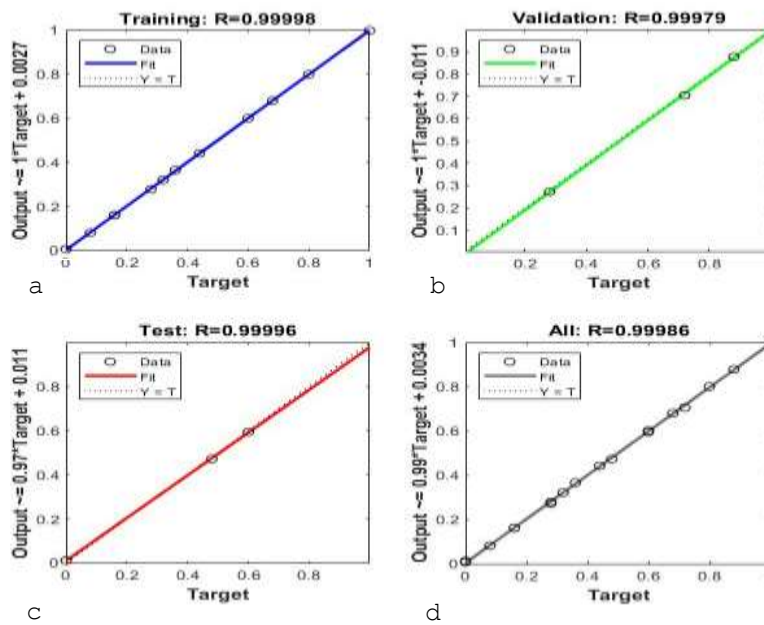
Source: Own Elaboration

3.3.6. Student's t-test on paired data

T-student's test is one of the most popular statistical techniques used to test whether the mean difference between two groups is statistically significant [57]. This test was used to evaluate the precision reliability of the results predicted by chemometric models and the results of physicochemical properties by conventional methods. T-student's distribution used the tailed test with a 95% confidence interval and with an external validation value of the T student's test (tv)= ± 2.11. Table 3.11 shows the confidence values of the T student's test (tc) for the physicochemical properties compared to the tv.

Table 3.11 T-student's paired data t-test results for physicochemical properties

Property	tv	tc	-tv > tc > tv
Free acid number	±2.11	1.40	Complied with
Flash point	±2.11	0.60	Complied with
Density	±2.11	0.30	Complied with
Specific gravity 29.5 ºC	±2.11	-0.92	Complied with
API density	±2.11	-1.10	Complied with
Specific gravity	±2.11	0.30	Complied with
Kinematic viscosity	±2.11	0.42	Complied with
Freezing point	±2.11	-0.42	Complied with

Source: Own Elaboration

In the definition of this test, we found that the tc results for all physicochemical properties are within the confidence interval of ±2.11, which is that there are no significant differences between the experimental data obtained by ASTM D6751 and EN 14214 and those predicted by the chemometric models. Therefore, with the paired data T-student's test it is demonstrated that the chemometric models have a predictive capacity to determine the values of the physicochemical properties as reliable as the analyses performed by conventional methods indicated by ASTM D6751 and EN 14214.

Conclusions

From the results obtained in this work, the following conclusions can be drawn:

The values of the physical and chemical properties of the diesel-biodiesel blends (D-10, D-20, D-40, D-50, D-60, D-80 and D-90) were within the range of values established in the ASTM D 6751 and EN 14214 standards.

The chemometric models built by means of neural networks from Raman spectroscopy information, allowed predicting: density, specific weight, API density, flash point, freezing point, kinematic viscosity of diesel/biodiesel blends with a precision and certainty similar to the standard methods established in the American and European norms.

The chemometric models obtained in this work allow determining: density, specific gravity, API density, flash point, freezing point, kinematic viscosity of diesel/biodiesel blends, requiring less working time. In addition, by not using reagents, they are more environmentally friendly.

The paired data T-student test was another useful statistical tool to determine the predictive ability of the chemometric models. The T-student confidence values (tc) for each model were within the range of external validation (tv= ± 2.11).

References

[1] L. Al-Ghussain, "Global warming: review on driving forces and mitigation," *Environmental Progress and Sustainable Energy*, vol. 38, no. 1. John Wiley and Sons Inc., pp. 13–21, Jan. 01, 2019. doi:10.1002/ep.13041. https://aiche.onlinelibrary.wiley.com/doi/10.1002/ep.13041.

[2] M. A. El-Sharkawy, "Global warming: Causes and impacts on agroecosystems productivity and food security with emphasis on cassava comparative advantage in the tropics/subtropics," *Photosynthetica*, vol. 52, no. 2, pp. 161–178, 2014, doi: 10.1007/s11099-014-0028-7. https://link.springer.com/article/10.1007/s11099-014-0028-7.

[3] K. R. Bukkarapu and A. Krishnasamy, "A critical review on available models to predict engine fuel properties of biodiesel," *Renewable and Sustainable Energy Reviews*, vol. 155, p. 111925, Mar. 2022, doi: 10.1016/j.rser.2021.111925. https://www.sciencegate.app/document/10.1016/j.rser.2021.111925.

[4] K. R. Bukkarapu and A. Krishnasamy, "Predicting engine fuel properties of biodiesel and biodiesel-diesel blends using spectroscopy based approach," *Fuel Processing Technology*, vol. 228, Jun. 2022, doi: 10.1016/j.fuproc.2022.107227 https://www.sciencegate.app/document/10.1016/j.rser.2021.111925.

[5] S. Sayyed, R. K. Das, and K. Kulkarni, "Performance assessment of multiple biodiesel blended diesel engine and NOx modeling using ANN," *Case Studies in Thermal Engineering*, vol. 28, Dec. 2021, doi: 10.1016/j.csite.2021.101509. https://www.sciencedirect.com/science/article/pii/S2214157X21006729.

[6] R. L. Naylor and M. M. Higgins, "The rise in global biodiesel production: Implications for food security," *Global Food Security*, vol. 16. Elsevier B.V., pp. 75–84, Mar. 01, 2018. doi: 10.1016/j.gfs.2017.10.004. https://www.sciencedirect.com/journal/global-food-security/vol/12/suppl/C.

[7] H. M. Khan *et al.*, "Production and utilization aspects of waste cooking oil based biodiesel in Pakistan," *Alexandria Engineering Journal*, vol. 60, no. 6, pp. 5831–5849, Dec. 2021, doi: 10.1016/j.aej.2021.04.043. https://www.sciencedirect.com/journal/alexandria-engineering-journal/vol/61/issue/10.

[8] International Energy Agency, "Renewable Energy Market Update - June 2023," Paris, Jun. 2023. Accessed: Aug. 21, 2023. [Online]. Available: https://www.iea.org/reports/renewable-energy-market-update-june-2023. https://www.iea.org/reports/renewable-energy-market-update-june-2023.

[9] S. Rezania *et al.*, "Review on transesterification of non-edible sources for biodiesel production with a focus on economic aspects, fuel properties and by-product applications," *Energy Conversion and Management*, vol. 201. Elsevier Ltd, Dec. 01, 2019. doi: 10.1016/j.enconman.2019.112155. https://www.sciencedirect.com/science/article/abs/pii/S0196890419311616.

[10] J. A. Aricetti and M. Tubino, "A green and simple visual method for the determination of the acid-number of biodiesel," *Fuel*, vol. 95, pp. 659–661, May 2012, doi: 10.1016/j.fuel.2011.10.058. https://www.sciencedirect.com/journal/fuel/vol/96/suppl/C.

[11] S. K. Tulashie and F. Kotoka, "The potential of castor, palm kernel, and coconut oils as biolubricant base oil via chemical modification and formulation," *Thermal Science and Engineering Progress*, vol. 16, May 2020, doi: 10.1016/j.tsep.2020.100480. https://www.sciencedirect.com/journal/thermal-science-and-engineering-progress/vol/19/suppl/C.

[12] A. T. Hoang, "Prediction of the density and viscosity of biodiesel and the influence of biodiesel properties on a diesel engine fuel supply system," *Journal of Marine Engineering & Technology*, vol. 20, no. 5, pp. 299–311, Oct. 2021, doi: 10.1080/20464177.2018.1532734. https://www.tandfonline.com/doi/full/10.1080/20464177.2018.1532734.

[13] S. Banik *et al.*, "Production of biodiesel from neem seed oil," *Bangladesh Journal of Scientific and Industrial Research*, vol. 53, no. 3, pp. 211–218, Sep. 2018, doi: 10.3329/bjsir.v53i3.38268. https://doaj.org/toc/2224-7157.

[14] G. W. Auner *et al.*, "Applications of Raman spectroscopy in cancer diagnosis," *Cancer and Metastasis Reviews*, vol. 37, no. 4, pp. 691–717, Dec. 2018, doi: 10.1007/s10555-018-9770-9. https://pubmed.ncbi.nlm.nih.gov/30569241/.

[15] H. E. Tahir *et al.*, "Rapid prediction of phenolic compounds and antioxidant activity of Sudanese honey using Raman and Fourier transform infrared (FT-IR) spectroscopy," *Food Chem*, vol. 226, pp. 202–211, Jul. 2017, doi: 10.1016/j.foodchem.2017.01.024. https://www.sciencedirect.com/journal/food-chemistry.

[16] S. Li, Y. Shan, X. Zhu, X. Zhang, and G. Ling, "Detection of honey adulteration by high fructose corn syrup and maltose syrup using Raman spectroscopy," *Journal of Food Composition and Analysis*, vol. 28, no. 1, pp. 69–74, Nov. 2012, doi: 10.1016/j.jfca.2012.07.006. https://www.sciencedirect.com/journal/journal-of-food-composition-and-analysis

[17] S. P. Kek, N. L. Chin, Y. A. Yusof, S. W. Tan, and L. S. Chua, "Classification of entomological origin of honey based on its physicochemical and antioxidant properties," *Int J Food Prop*, vol. 20, no. sup3, pp. S2723–S2738, Dec. 2017, doi: 10.1080/10942912.2017.1359185. https://www.sciencedirect.com/journal/journal-of-food-composition-and-analysis.

[18] A. Belay, W. K. Solomon, G. Bultossa, N. Adgaba, and S. Melaku, "Physicochemical properties of the Harenna forest honey, Bale, Ethiopia," *Food Chem*, vol. 141, no. 4, pp. 3386–3392, Dec. 2013, doi: 10.1016/j.foodchem.2013.06.035. https://www.sciencedirect.com/search?qs=Physicochemical%20properties%20of%20the%20Harenna%20forest%20honey%2C%20Bale%2C%20Ethiopia.

[19] F. Anguebes-Franseschi *et al.*, "Raman spectroscopy and chemometric modeling to predict physical-chemical honey properties from campeche, Mexico," *Molecules*, vol. 24, no. 22, Nov. 2019, doi: 10.3390/molecules24224091. https://www.mdpi.com/1420-3049/24/22/4091.

[20] M. Oroian and S. Ropciuc, "Romanian honey authentication using voltammetric electronic tongue. Correlation of voltammetric data with physico-chemical parameters and phenolic compounds," *Comput Electron Agric*, vol. 157, pp. 371–379, Feb. 2019, doi: 10.1016/j.compag.2019.01.008. https://dl.acm.org/doi/10.1016/j.compag.2019.01.008.

[21] A. D. V. Máquina, B. V. Sitoe, J. E. Buiatte, D. Q. Santos, and W. B. Neto, "Quantification and classification of cotton biodiesel content in diesel blends, using mid-infrared spectroscopy and chemometric methods," *Fuel*, vol. 237, pp. 373–379, Feb. 2019, doi: 10.1016/j.fuel.2018.10.011. https://www.sciencedirect.com/journal/fuel/vol/218/suppl/C.

[22] O. Aboelazayem, M. Gadalla, and B. Saha, "Derivatisation-free characterisation and supercritical conversion of free fatty acids into biodiesel from high acid value waste cooking oil," *Renew Energy*, vol. 143, pp. 77–90, Dec. 2019, doi: 10.1016/j.renene.2019.04.106. https://www.sciencedirect.com/journal/renewable-energy/vol/142/suppl/C

[23] M. Kirubakaran and V. Arul Mozhi Selvan, "A comprehensive review of low cost biodiesel production from waste chicken fat," *Renewable and Sustainable Energy Reviews*, vol. 82, pp. 390–401, Feb. 2018, doi: 10.1016/j.rser.2017.09.039. https://www.sciencedirect.com/journal/renewable-energy/vol/142/suppl/C.

[24] E. Fayyazi, B. Ghobadian, G. Najafi, and B. Hosseinzadeh, "An ultrasound-assisted system for the optimization of biodiesel production from chicken fat oil using a genetic algorithm and response surface methodology," *Ultrason Sonochem*, pp. 313–320, Mar. 2015, doi: http://dx.doi.org/10.1016/j.ultsonch.2015.03.007. https://www.sciencedirect.com/science/article/abs/pii/S1350417715000693

[25] K. Srinivasa Rao AssoProf, M. Engineering, and B. S. K Sundara Siva Rao Professor, "Experimental Studies on the Characteristics of Diesel Engine with Chicken Fat Methyl Ester," 2013. [Online]. Available: https://www.researchgate.net/publication/236864493. https://www.researchgate.net/publication/236864493_Experimental_Studies_on_the_Characteristics_of_Diesel_Engine_with_Chicken_Fat_Methyl_Ester.

[26] J. M. Dias, M. C. M. Alvim-Ferraz, M. F. Almeida, J. D. Méndez Díaz, M. Sánchez Polo, and J. Rivera Utrilla, "Biodiesel production using calcium manganese oxide as catalyst and different raw materials," *Energy Convers Manag*, vol. 65, pp. 647–653, Jan. 2013, doi: 10.1016/j.enconman.2012.09.016. https://www.sciencedirect.com/science/article/abs/pii/S0196890412003664.

[27] C. B. Ezekannagha, C. N. Ude, and O. D. Onukwuli, "Optimization of the methanolysis of lard oil in the production of biodiesel with response surface methodology," *Egyptian Journal of Petroleum*, vol. 26, no. 4, pp. 1001–1011, Dec. 2017, doi: 10.1016/j.ejpe.2016.12.004. https://www.sciencedirect.com/science/article/pii/S1110062116301556.

[28] N. Joy, J. Jayaraman, A. Mariadhas, P. Appavu, R. Tiwari, and R. Sarkar, "Effect of EGR on performance and emission of CI engine using biodiesel blend of pork lard," in *AIP Conference Proceedings*, American Institute of Physics Inc., Dec. 2020. doi: 10.1063/5.0034496. https://pubs.aip.org/aip/pof/search-results?page

[29] I. Ambat, V. Srivastava, S. Iftekhar, E. Haapaniemi, and M. Sillanpää, "Effect of different co-solvents on biodiesel production from various low-cost feedstocks using Sr–Al double oxides," *Renew Energy*, vol. 146, pp. 2158–2169, Feb. 2020, doi: 10.1016/j.renene.2019.08.061. https://www.sciencedirect.com/science/article/abs/pii/S0960148119312492.

[30] R. U. Azike and W. A. Raji, "Optimization of Biodiesel Production from Pig Lard using Sodium Hydroxide as Catalyst," *Nigerian Research Journal of Engineering and Environmental Sciences*, pp. 529–534, 2019, Accessed: Dec. 14, 2022. [Online]. Available: https://www.researchgate.net/profile/Wuraola.

[31] I. J. Stojković, M. R. Miladinović, O. S. Stamenković, I. B. Banković-Ilić, D. S. Povrenović, and V. B. Veljković, "Biodiesel production by methanolysis of waste lard from piglet roasting over quicklime," *Fuel*, vol. 182, pp. 454–466, Oct. 2016, doi: 10.1016/j.fuel.2016.06.014. https://www.sciencedirect.com/science/article/abs/pii/S0016236116304665.

[32] M. Agarwal, K. Singh, and S. P. Chaurasia, "Prediction of Biodiesel Properties from Fatty Acid Composition using Linear Regression and ANN Techniques," *Indian Chemical Engineer*, vol. 52, no. 4, pp. 347–361, Dec. 2010, doi: 10.1080/00194506.2010.616325. https://www.researchgate.net/search/publication.

[33] Gómez Rodríguez Karla Aída, "Estimación de propiedades del diésel y su uso en la determinación de un índice de calidad," Centro de Investigación Científica de Yucatán. AC, Mérida,Yucatán,2021.Accessed:May,13,2023.[Online].Available:https://cicy.repositorioinstitucional.m x/jspui/bitstream/1003/2120/1/PCER_M_Tesis_2021_Karla_Aida_Gomez_Rodriguez.pdf.

[34] M. Rajendra, P. C. Jena, and H. Raheman, "Prediction of optimized pretreatment process parameters for biodiesel production using ANN and GA," *Fuel*, vol. 88, no. 5, pp. 868–875, May 2009, doi: 10.1016/j.fuel.2008.12.008. https://www.sciencedirect.com/science/article/abs/pii/S0016236108005024.

[35] I. B. Banković-Ilić, I. J. Stojković, O. S. Stamenković, V. B. Veljkovic, and Y.-T. Hung, "Waste animal fats as feedstocks for biodiesel production," *Renewable and Sustainable Energy Reviews*, vol. 32, pp. 238–254, Apr. 2014, doi: 10.1016/j.rser.2014.01.038. https://www.sciencedirect.com/science/article/abs/pii/S1364032114000495

[36] B. R. Moser, "Biodiesel production, properties, and feedstocks," *In Vitro Cellular and Developmental Biology - Plant*, vol. 45, no. 3. pp. 229–266, Jun. 2009. doi: 10.1007/s11627-009-9204-z. https://link.springer.com/article/10.1007/s11627-009-9204-z.

[37] V. T. Wyatt, M. A. Hess, R. O. Dunn, T. A. Foglia, M. J. Haas, and W. N. Marmer, "Fuel properties and nitrogen oxide emission levels of biodiesel produced from animal fats," *J Am Oil Chem Soc*, vol. 82, no. 8, pp. 585–591, Aug. 2005, doi: 10.1007/s11746-005-1113-2. https://link.springer.com/article/10.1007/s11746-005-1113-2

[38] M. I. Jahirul *et al.*, "Investigation of correlation between chemical composition and properties of biodiesel using principal component analysis (PCA) and artificial neural network (ANN)," *Renew Energy*, vol. 168, pp. 632–646, May 2021, doi: 10.1016/j.renene.2020.12.078. https://link.springer.com/article/10.1007/s11746-005-1113-2.

[39] R. Behçet, H. Oktay, A. Çakmak, and H. Aydin, "Comparison of exhaust emissions of biodiesel–diesel fuel blends produced from animal fats," *Renewable and Sustainable Energy Reviews*, vol. 46, pp. 157–165, Jun. 2015, doi: 10.1016/j.rser.2015.02.015.

[40] F. Toldrá-Reig, L. Mora, and F. Toldrá, "Trends in Biodiesel Production from Animal Fat Waste," *Applied Sciences*, vol. 10, no. 10, p. 3644, May 2020, doi: 10.3390/app10103644. https://www.sciencedirect.com/science/article/abs/pii/S1364032115001033.

[41] M. Keihani, H. Esmaeili, and P. Rouhi, "Biodiesel Production from Chicken Fat Using Nano-calcium Oxide Catalyst and Improving the Fuel Properties via Blending with Diesel," *Biodiesel Production from Chicken Fat Using Nano-calcium Oxide Catalyst and Improving the Fuel Properties via Blending with Diesel*, pp. 522–529, May 2018, doi: DOI:10.22036/pcr.2018.114565.1453. https://www.researchgate.net/publication/325360075_Biodiesel_Production_from_Chicken_Fat_Using_Nano-calcium_Oxide_Catalyst_and_Improving_the_Fuel_Properties_via_Blending_with_Diesel.

[42] M. N. Mohiddin, A. A. Saleh, A. N. R. Reddy, and S. Hamdan, "A Study on Chicken Fat as an Alternative Feedstock: Biodiesel Production, Fuel Characterisation, and Diesel Engine Performance Analysis," *International Journal of Automotive and Mechanical Engineering*, vol. 15, no. 3, pp. 5535–5546, Oct. 2018, doi: 10.15282/ijame.15.3.2018.10.0425. https://www.researchgate.net/publication/328121172_A_Study_on_Chicken_Fat_as_an_Alternative_Feedstock_Biodiesel_Production_Fuel_Characterisation_and_Diesel_Engine_Performance_Analysis.

[43] T. M. Mata, N. Cardoso, M. Ornelas, S. Neves, and N. S. Caetano, "Sustainable production of biodiesel from tallow, lard and poultry fat and its quality evaluation," in *Chemical Engineering Transactions*, Italian Association of Chemical Engineering - AIDIC, 2010, pp. 13–18. doi: 10.3303/CET1019003. https://www.cetjournal.it/index.php/cet/article/view/8349.

[44] A. B. Fadhil, I. K. Saeed, L. I. Saeed, and M. H. Altamer, "Co-solvent ethanolysis of chicken waste: Optimization of parameters and characterization of biodiesel," *Energy Sources, Part A: Recovery, Utilization, and Environmental Effects*, vol. 38, no. 19, pp. 2883–2890, Oct. 2016, doi: 10.1080/15567036.2015.1065299. https://www.tandfonline.com/doi/abs/10.1080/15567036.2015.1065299?journalCode=ueso20.

[45] V. Hariram *et al.*, "Biodiesel Extraction from Chicken Fat and Its Effect on the Performance and Emission Characteristics of the Diesel Engine," *Nature Environment and Pollution Technology*, vol. 20, no. 4, Dec. 2021, doi: 10.46488/NEPT.2021.v20i04.041. https://www.researchgate.net/publication/356857545_Biodiesel_Extraction_from_Chicken_Fat_and_Its_Effect_on_the_Performance_and_Emission_Characteristics_of_the_Diesel_Engine

[46] Ramos, Dias, Puna, Gomes, and Bordado, "Biodiesel Production Processes and Sustainable Raw Materials," *Energies (Basel)*, vol. 12, no. 23, p. 4408, Nov. 2019, doi: 10.3390/en12234408. https://www.mdpi.com/1996-1073/12/23/4408.

[47] N. Kinnal, G. Sujaykumar, S. W. D'costa, and G. S. Girishkumar, "Investigation on Performance of Diesel Engine by Using Waste Chicken Fat Biodiesel," *IOP Conf Ser Mater Sci Eng*, vol. 376, p. 012012, Jun. 2018, doi: 10.1088/1757-899X/376/1/012012. https://iopscience.iop.org/article/10.1088/1757-899X/376/1/012012/pdf.

[48] T. M. Mata, N. Cardoso, M. Ornelas, S. Neves, and N. S. Caetano, "Evaluation of Two Purification Methods of Biodiesel from Beef Tallow, Pork Lard, and Chicken Fat," *Energy & Fuels*, vol. 25, no. 10, pp. 4756–4762, Oct. 2011, doi: 10.1021/ef2010207. https://pubs.acs.org/doi/full/10.1021/ef2010207?src=recsys.

[49] C. B. Ezekannagha, C. N. Ude, and O. D. Onukwuli, "Optimization of the methanolysis of lard oil in the production of biodiesel with response surface methodology," *Egyptian Journal of Petroleum*, vol. 26, no. 4, pp. 1001–1011, Dec. 2017, doi: 10.1016/j.ejpe.2016.12.004. https://www.sciencedirect.com/science/article/pii/S1110062116301556.

[50] R. Foroutan, R. Mohammadi, and B. Ramavandi, "Waste glass catalyst for biodiesel production from waste chicken fat: Optimization by RSM and ANNs and toxicity assessment," *Fuel*, vol. 291, p. 120151, May 2021, doi: 10.1016/j.fuel.2021.120151. https://www.sciencegate.app/document/10.1016/j.fuel.2021.120151#google_vignette.

[51] V. Kumbhar, A. Pandey, C. R. Sonawane, A. S. El-Shafay, H. Panchal, and A. J. Chamkha, "Statistical analysis on prediction of biodiesel properties from its fatty acid composition," *Case Studies in Thermal Engineering*, vol. 30, p. 101775, Feb. 2022, doi:10.1016/j.csite.2022.101775. https://www.sciencegate.app/document/10.1016/j.csite.2022.101775

[52] X. Meng, M. Jia, and T. Wang, "Neural network prediction of biodiesel kinematic viscosity at 313K," *Fuel*, vol. 121, pp. 133–140, Apr. 2014, doi: 10.1016/j.fuel.2013.12.029. https://www.sciencegate.app/document/10.1016/j.csite.2022.101775.

[53] M. Mostafaei, "Prediction of biodiesel fuel properties from its fatty acids composition using ANFIS approach," *Fuel*, vol. 229, pp. 227–234, Oct. 2018, doi: 10.1016/j.fuel.2018.04.148. https://www.sciencedirect.com/science/article/abs/pii/S0016236118307841

[54] B. Su et al., "Effect of Pour Point Depressants Combined with Dispersants on the Cold Flow Properties of Biodiesel-Diesel Blends," JAOCS, Journal of the American Oil Chemists' Society, vol. 98, no. 2, pp. 163–172, Feb. 2021, doi.org/10.1002/aocs.12456, https://aocs.onlinelibrary.wiley.com/doi/abs/10.1002/aocs.12456.

[55] Md. E. Hoque, A. Singh, and Y. L. Chuan, "Biodiesel from low cost feedstocks: The effects of process parameters on the biodiesel yield," *Biomass Bioenergy*, vol. 35, no. 4, pp. 1582–1587, Apr. 2011, doi: 10.1016/j.biombioe.2010.12.024. https://www.sciencedirect.com/science/article/abs/pii/S0961953410004824.

[56] R. O. Dunn, "Effects of minor constituents on cold flow properties and performance of biodiesel," Progress in Energy and Combustion Science, vol. 35, no. 6. pp. 481–489, Dec. 2009. doi: 10.1016/j.pecs.2009.07.002. https://www.sciencedirect.com/science/article/abs/pii/S0360128509000331.

[57] P. Mishra, U. Singh, C. Pandey, P. Mishra, and G. Pandey, "Application of student's t-test, analysis of variance, and covariance," *Ann Card Anaesth*, vol. 22, no. 4, p. 407, 2019, doi: 10.4103/aca.ACA_94_19. https://pubmed.ncbi.nlm.nih.gov/31621677/.

Chapter 5 The behavior of the pigment discoloration Permalon Rhodamine B 400% red in a liquid medium after exposure to a non-thermal plasma of different electrical power at atmospheric pressure

Capítulo 5 Comportamiento de la decoloración del pigmento Permalon Rhodamine B 400% red en medio líquido, tras su exposición ante un plasma no térmico de diferente potencia eléctrica a presión atmosférica

ÁVILA-MARES, Isidro Mildred†, ALARCÓN-HERNÁNDEZ, Fidel Benjamín*, FUENTES-ALBARRÁN, María del Carmen and GADEA-PACHECO, José Luis

Universidad Autónoma del Estado de Morelos, Facultad de Ciencias Biológicas.

ID 1st Author: *Isidro Mildred, Ávila-Mares* / **ORC ID**: 0009-0008-5869-0215, **CVU CONAHCYT ID**: 1321815

ID 1st Co-author: *Fidel Benjamín, Alarcón-Hernández* / **ORC ID**: 0000-0002-2465-0898, **CVU CONAHCYT ID**: 131028

ID 2nd Co-author: *María Del Carmen, Fuentes-Albarrán* / **ORC ID**: 0000-0003-1308-1332, **CVU CONAHCYT ID**: 171814

ID 3rd Co-author: *José Luis, Gadea-Pacheco* / **ORC ID**: 0000-0001-9341-9289, **CVU CONAHCYT ID**: 160429

I. Ávila, F. Alarcón, M. Fuentes, J. Gadea

* honorato@uaem.mx

Abstract

The behavior of the discoloration of the pigment Permalon Rhodamine B 400% red in a liquid medium (120 mg/L) derived from exposure to a non-thermal air plasma at atmospheric pressure was quantified experimentally. Observed changes in dilution were measured as a function of plasma generation electrical power (40.0 W, 60.0 W, 80.0 W, and 100.0 W), as well as exposure time (150 minutes per power). Solution-generated effects were monitored by UV/VIS spectrophotometry measurements (absorbance; $\lambda = 533$ nm), pH, and temperature change. The absorbance of the solution increased at the beginning of the treatments to decrease after a particular time (15 minutes). The maximum effect was observed at 100.0 W (maximum power used) at minute 150; it decreased by about 2% (maximum decrease at higher power), pH by 43%, and temperature increased from 27 to 58 °C. The results showed that the change in the discoloration of the pigment in a liquid medium directly depends on the working electrical power of the plasma and the exposure time to the treatment of the solution.

Absorbance, pH, Non-thermal plasma, Water treatment

Resumen

Se cuantificó experimentalmente el comportamiento de la decoloración del pigmento Permalon Rhodamine B 400% red en medio líquido (120 mg/L) derivado de la exposición ante un plasma no térmico de aire a presión atmosférica. Se midieron los cambios observados en la dilución como función de la potencia eléctrica de generación del plasma (40.0 W, 60.0 W, 80.0 W y 100.0 W), así como del tiempo de exposición (150 minutos por potencia). Los efectos generados en la solución se monitorearon mediante medidas de espectrofotometría UV / VIS (absorbancia; $\lambda = 533$ nm), pH y cambio de temperatura. La absorbancia de la solución incrementó al inicio de los tratamientos para después de cierto tiempo (15 minutos) disminuir. El máximo efecto se observó a 100.0 W (máxima potencia utilizada) al minuto 150, disminuyó cerca de un 2 % (máximo decremento a mayor potencia), el pH un 43 % y la temperatura incrementó de 27 a 58 °C. Los resultados mostraron que el cambio en la decoloración del pigmento en medio líquido depende directamente de la potencia eléctrica de trabajo del plasma y del tiempo de exposición al tratamiento de la solución.

Absorbancia, pH, Plasma no térmico, Tratamiento de aguas

1. Introduction

At present, the deterioration of water quality together with the problems of depletion of water supplies are one of the many problems faced by modern society in obtaining and using uncontaminated water. In particular, this situation is aggravated by the fact that wastewater is not fully restored in terms of pollution and thus becomes yet another source of contaminants of various kinds; such as microorganisms, bacteria, pesticides, lubricants, synthetic fertilizers, as well as synthetic dyes (Sharma *et al*., 2022; Goscianska *et al*., 2015; Yagub *et al*., 2014; Zhao *et al*., 2013).

Specifically, synthetic dyes have an increasing percentage of use within the cosmetics, paper, textile, food and fur industries among several others, so their use generates an increase in the volume of wastewater from these industries (Varjani *et al*., 2020). It is known that the presence of certain concentrations of dyes in water bodies interferes with the biological cycles within them, as it destroys the original ecosystem due to its toxicity and lack of degradability, which represents a serious problem for the health of people, but mainly for aquatic life (Forgacs *et al*., 2004).

In particular, Rhodamine B dye is one of the dyes that is used in multiple industries and therefore is made with high frequency. It is used in the textile industry, in the manufacture of pens, paints, dyes, explosives, carbon sheets, stamp inks and even in the manufacture of cookies (Hamdaoui, 2011; Imam and Babamale, 2020).

It should be noted that Rhodamine B is one of the most toxic dyes present in textile wastewater due to its high stability and non-biodegradability. Likewise, its high staining capacity is a characteristic that makes it harmful in bodies of water, as it prevents the passage of light and inhibits the bioprocesses of aquatic plants and microorganisms that cohabit there (Sharma *et al*., 2022).

On the other hand, Rhodamine B has shown fluorescence emission bands under certain conditions, and in its pure state forms highly fluorescent H-aggregates in glycerol, ethylene glycol, methanol and butanol under ambient conditions. The pH-dependent absorption and emission spectra for a fixed concentration of Rhodamine B in the solvents reveal a red shift in the respective absorption and emission maxima (Radiul *et al.*, 2022). This last characteristic is an important factor to consider in the treatments used to decrease the absorbance of Rhodamine B.

From this perspective, the objective of the present experimental study is to observe the effect on the change in absorbance of a solution of Permalon Rhodamine B 400% network in liquid medium, as well as the pH and temperature after exposure for a specific time to an air plasma of different electrical power at atmospheric pressure.

It is known that air plasmas at atmospheric pressure have the ability to generate various molecules (e.g., ozone or H_2O_2), as well as multiple species (charged particles) that when reacting with water produce -OH radicals, OH+ ion, atomic hydrogen and atomic oxygen radicals, which can contribute to the degradation of the compounds in it discharged (Panda and Mathews, 2014).

Knowing and understanding the behavior of the change in absorbance or decrease in the coloration of the solution of interest through this research, gives a guideline to establish a methodology that contributes to the treatment of industrial wastewater with similar characteristics, using an air plasma at atmospheric pressure.

The methodology section presents the chemical characteristics of the dye under study, as well as the techniques chosen to determine the variables of interest according to the experimental device used. The results section shows the graphs of absorbance, pH and temperature change of the solution obtained after the experimentation; from which the most relevant observations are presented in the conclusions section.

2. Experimental Methodology

Rhodmin *B Pigment*

Rhodamine B pigment (CI 45170) was used without any purification, physical or chemical changes. Its formula and molecular weight are $C_{28}H_{31}ClN_2O_3$ and 479.01 g/mol respectively. All experiments were started with a dye stock solution of 120 mg/L (Rhodamine B in distilled water). Such concentration value was considered in response of the resolution of absorbance measurements obtained by the spectrophotometer used. Higher concentration did not allow clarity at the absorbance maximum. The chemical structure of the pigment is shown in Fig. 2.1.

Figure 2.1 Chemical structure of *Rhodamine B*
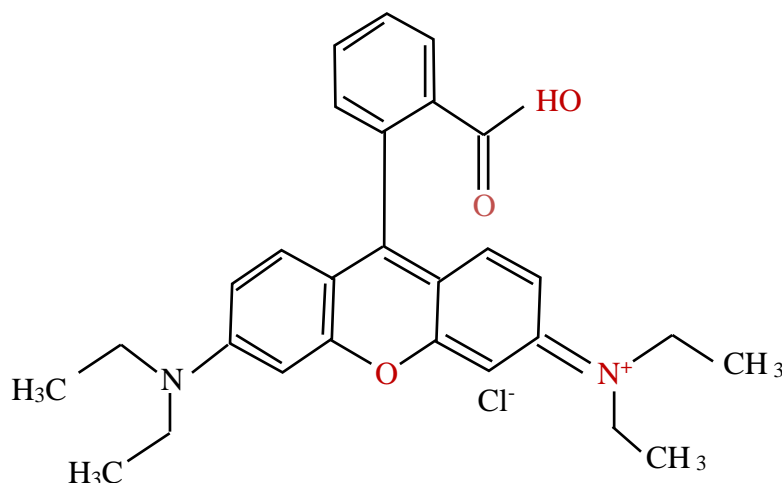
Source of Reference: Own Image

Experimental System

The experimental system is similar to the one used in our previous works (Alarcón *et al.*, 2019; Alarcón *et al.*, 2022a; Alarcón *et al* 2022b; Alarcón *et al* 2022c). A schematic of this is shown in Figure 2.2. It is basically composed of the following parts: hermetically sealed glass chamber with a capacity of 1.0 L, two tungsten electrodes, a mercury thermometer, and a high voltage source. In this device, one electrode is always immersed in the solution of interest, while the other one is adjusted at a distance of about 2 mm so that the plasma is generated. In particular, the plasma is formed at the interface of the air contained inside the reaction chamber and the solution of interest, as shown in the schematic. The thermometer is always immersed in the solution and can measure the temperature at all times.

Figure 2.2 Schematic of the experimental setup
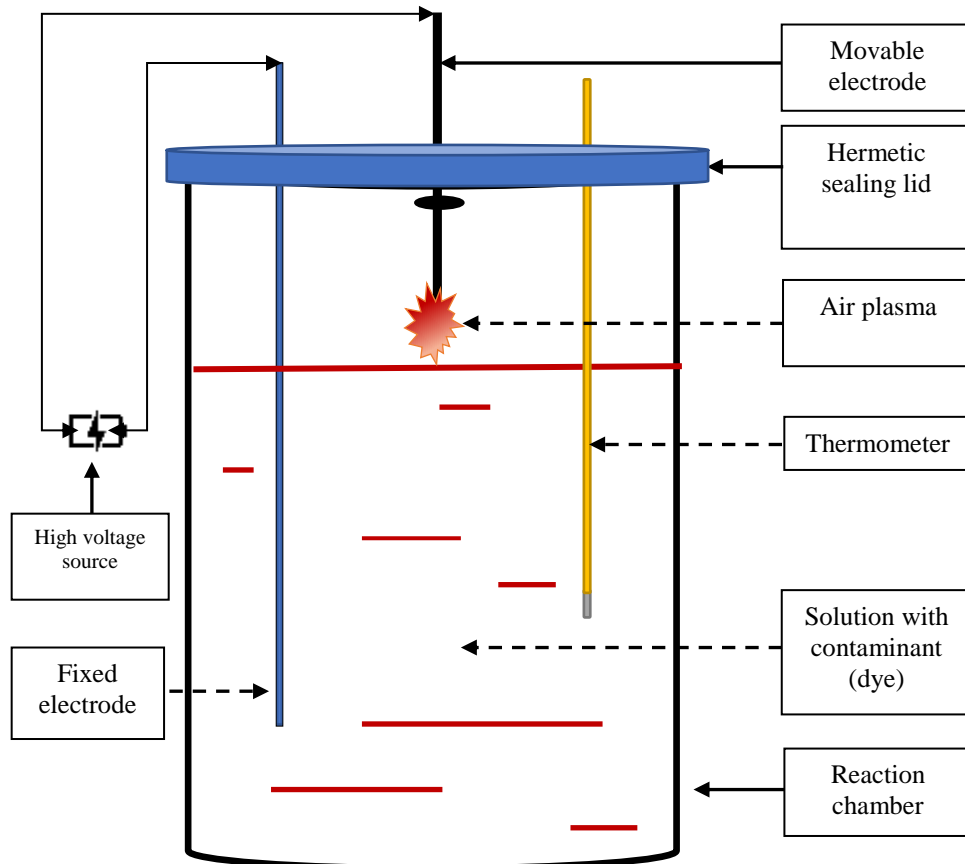
Source of Reference: Own Image

To subject the solution to plasma treatments, the following process is performed: 500 ml of the solution at a concentration of 120 mg/L are deposited in the reaction chamber of the experimental device used, the plasma generation parameters (voltage and current) are set on the high voltage source (SPELLMAN SL600), the moving electrode is adjusted and then the non-thermal plasma is generated. In particular, four plasma treatments of different electrical powers were considered at an initial temperature of 27 °C; the final temperature depends on the plasma power. Table 2.1 shows the parameters used for each treatment. Four replicates were performed for each treatment. The results presented are the average value of the measurements taken.

Table 1.1 Parameters considered for this experiment

Treatment	Exposure time (minutes)	Concentration (mg/L)	Electrical power (W)
T1	150	120	40
T2	150	120	60
T3	150	120	80
T4	150	120	100

Parameters considered for the performance of the experiments. Volume of solution used: 500 ml.

Sampling and measurement of parameters of interest

The process of sampling and measurement of the parameters considered was carried out every 15 minutes once the exposure of the solution to the treatment had begun. For this, the plasma generation is stopped, the temperature reading is taken (thermometer of the experimental system) and a sample is extracted to measure the absorbance and pH (Hach DR 3900 spectrophotometer and HI 9813-6N potentiometer, respectively). Once the necessary measurements have been taken, the sample solution is added to the reaction chamber and the treatment is resumed. This process is repeated until the experiment has lasted 150 minutes.

3. Results and Discussion

Given the fluorescence characteristics of the Permalon Rhodamine B 400% network dye under certain conditions, in this study the changes of the absorbance value were measured when a solution of this dye is exposed to an air plasma of different electrical power at atmospheric pressure, as well as the change of the pH value and the temperature of the solution.

Absorbance

The absorbance values of the solution of interest show a particular behavior very different from that of other dyes under the same conditions and treatments. Graph 3.1 illustrates such behavior as a function of exposure time to air plasma treatments at atmospheric pressure and for different values of plasma generation power.

Graph 3.1 Change in absorbance.
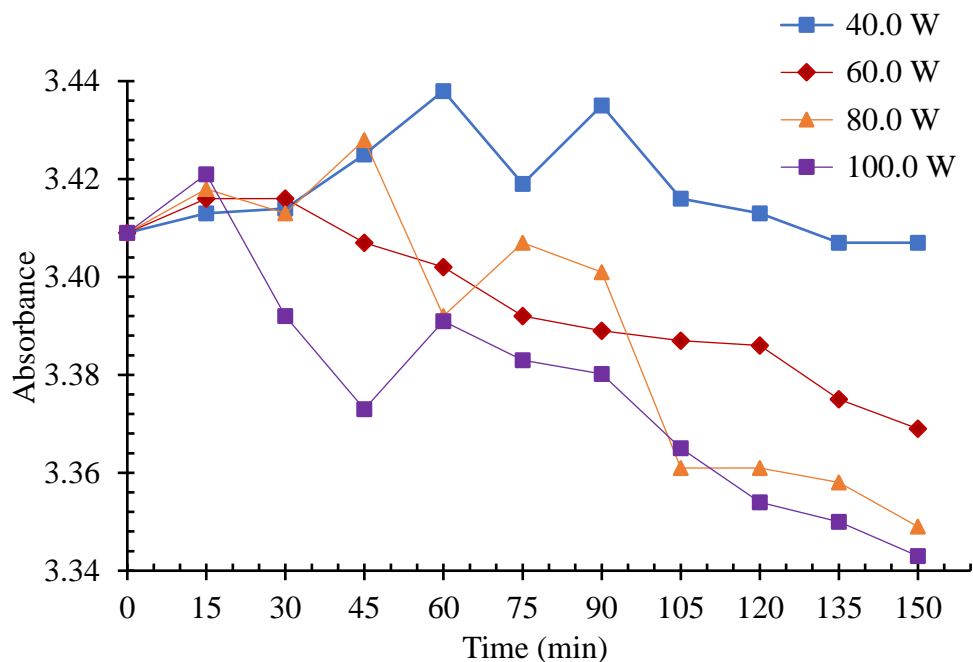
Source of Reference: Own Image

It is observed that the absorbance for the first fifteen minutes of treatment increases its value with respect to the initial value (3.409). Such behavior is presented for the four plasma treatments and shows an increasing dependence on the electrical power used (40, 60, 80, and 100 W), that is, the higher the plasma generation power, the greater the increase in the absorbance value (3.413, 3.416, 3.418 and 3.421) respectively.

On the other hand, for the 40 W electrical power treatment, the absorbance continued to increase (not so for the other treatments) until reaching a value of 3.438, corresponding to the exposure time of 60 minutes. After this time, the absorbance decreases to a value of 3.407.

That the increase in absorbance for the first fifteen minutes of exposure for all plasma treatments is proportional to the plasma generation power and that the increase in absorbance value is maintained for 60 minutes for plasma generated at the lowest power (40 W), may have a response in the characteristic fluorescence of the Rhodamine B dye.

In a recent experimental study (Radiul *et al.*, 2023), a previously undetected Rhodamine B fluorescence emission band was found, which is located between the spectral wavelength of 675 nm to 717 nm for the following solvents at ambient conditions: glycerol, ethylene glycol, methanol and butanol. Such a band is suggested, could be associated with the H-aggregates (H-dimer) of Rhodamine B and is confirmed by a blue-shifted band at 515 nm in the absorption spectra of Rhodamine B, in all solvents. In the present case, the absorbance maximum was presented at $\lambda = 533$ nm; which can be explained in terms of the working concentration (120 mg/L) (Radiul *et al.*, 2022). On the other hand, the formation of fluorescent H-aggregates was further corroborated by the variation of absorption and fluorescence peak intensity dependent on the experimental working concentration and pH. In particular, pH-dependent absorption and emission spectra for a fixed concentration of Rhodamine B in solvents reveal a red shift in the respective absorption and emission maxima (Radiul *et al.*, 2023).

For the other treatments (60, 80 and 100 W), the absorbance generally showed a decreasing behavior, reaching values of 3.369, 3.349 and 3.343 respectively at 150 minutes of plasma exposure. The largest decrease was observed for the 100 W treatment, decreasing a value of 0.066, equivalent to almost 2 %. It is noteworthy that the decrease in the absorbance value of the solution at 150 minutes of exposure to plasma is related to the power of plasma generation, the higher the power of plasma generation, the greater the discoloration.

pH.

The solution changes pH (decreases) as it is exposed to the plasma. The rate of decrease is associated with the plasma generation power and with the exposure time. The higher the plasma generation power, the faster the pH values decrease, the longer the exposure time to the plasma, the higher the acidity of the solution. Graph 3.2 shows this behavior.

In all the experiments, a rapid decrease in pH can be observed during the first 15 minutes, after which the decrease is slow and gradual until reaching the minimum value reached.

The pH values observed after 150 minutes of treatment changed from 5.3 to 3.0 (equivalent to 43 %) for all treatments, only that some treatments reached it in less time than others. Similar results regarding the behavior were obtained for other dyes exposed to plasmas under similar conditions (Alarcón *et al.*, 2019; Alarcón *et al.*, 2022a; Alarcón *et al* 2022b; Alarcón *et al* 2022c).

The decrease in pH is attributed to the chemical reactions that occur during the application of the plasma. On the one hand and considering the configuration of the experimental system, there is the generation of hydronium ions, obtained from the interaction of CO_2, water and plasma, and the subsequent reactions. Reactions (1) - (3).

$$CO_{2\ (ac)} + H_2O \rightarrow H_2CO_{3\ (ac)} \tag{1}$$

$$H_2CO_{3\ (ac)} + H_2O \rightarrow HCO_3^- + H_3O^+ \tag{2}$$

$$HCO_3^-{}_{(ac)} + H_2O \rightarrow CO_3^{2-} + H_3O^+ \tag{3}$$

On the other hand, in the reactor chamber and due to the generation of compounds such as HNO_3, HNO_2, among other products that can be formed in moist air plasmas, there is a change in the pH of the solution (Fahmy *et al.*, 2018; Shimizu *et al.*, 2020; Alarcón *et al.*, 2022a; Safenraider *et al.*, 2020).

Graph 3.2 pH change of the solution as a function of exposure time and plasma generation power
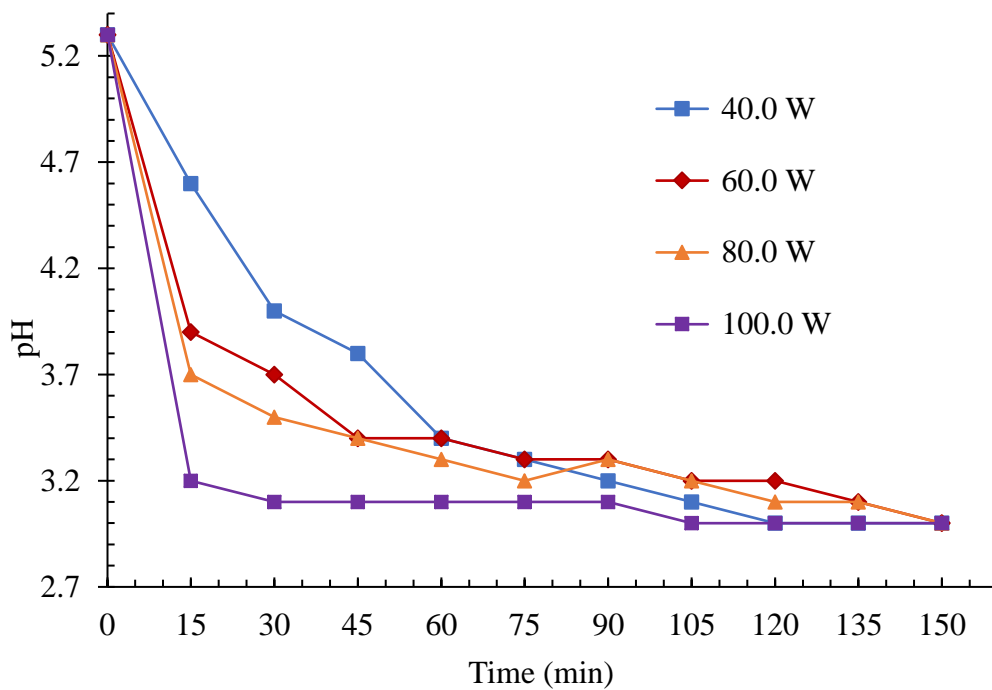
Source of Reference: Own Image

It should be considered that the change in pH of the solution after being exposed to the plasma is a consequence of the treatment, however; it also contributes to the change in the absorbance value and the wavelength at which it is determined (Radiul *et al*., 2023).

Temperature

Graph 3.3 shows the behavior of the temperature change of the solution as a function of exposure time and plasma generation power. It is observed that as the exposure time increases, the temperature value also increases. A similar behavior is shown for all plasma generation powers (40, 60, 80 and 100 W), in particular; the temperature changes from an initial value of 27 °C to 43, 47, 52 and 58 °C respectively.

Given the volumes of solution treated and the plasma generation powers, the rate of temperature change is different for each treatment. As the energy provided to the system increases, the rate of temperature rise increases as well. It is noteworthy that the temperature rise is not linear; it could be associated with a degree 2 polynomial behavior.

In particular, the temperature increase of the solution presents mainly two physical processes, the first one of heating of the solution with little evaporation and the second one of heating and at the same time greater evaporation (Alarcón *et al.,* 2022a).

It has been observed that increasing temperature does not necessarily generate changes in the discoloration of a dye solution (Alarcón *et al*., 2022b), however, it is necessary to perform the experiments for the solution of interest in the considered temperature range.

Graph 3.3 Solution temperature change behavior
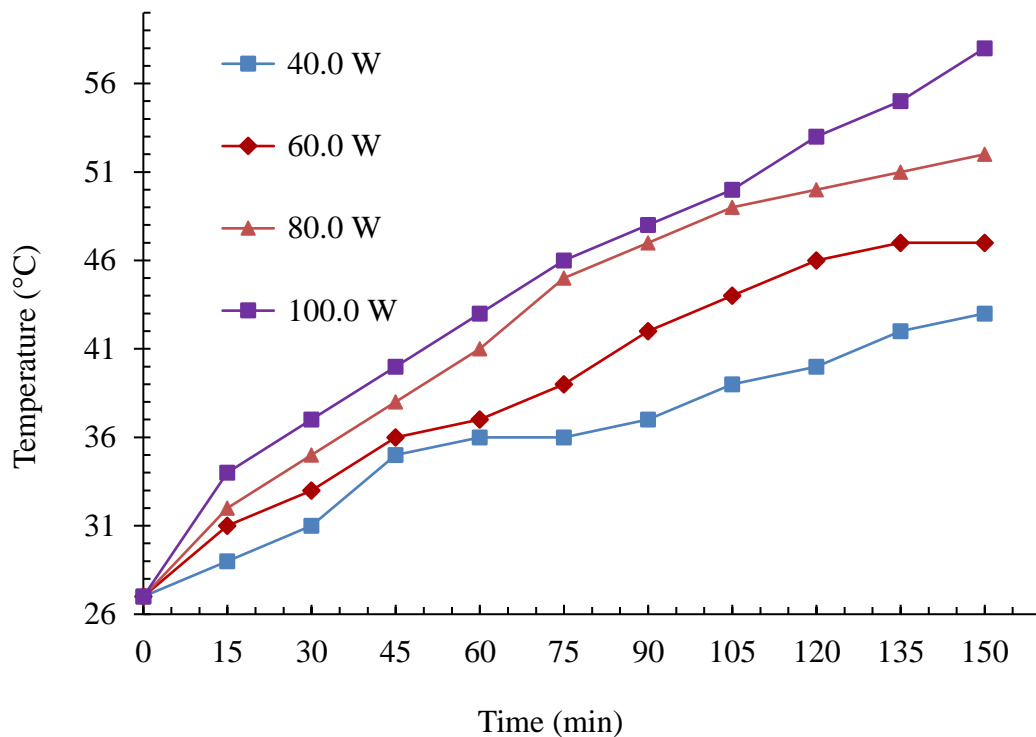
Source of Reference: Own Image

4. Acknowledgements

5. Conclusions

The discoloration behavior of the Permalon Rhodamine B 400% network pigment in liquid medium was quantified after its exposure to a non-thermal plasma of different electrical power (40, 60, 80 and 100 W) at atmospheric pressure and with a duration of 150 minutes per treatment. The change in pH and temperature values was also determined.

The absorbance of the solution showed for all the treatments, a singular behavior of increase for the first 15 minutes of exposure to the plasma, this; due to the fluorescence characteristics of Rhodamine B. The minimum absorbance value reached for the solution was almost 2 %; it rises and then decreases. The higher the plasma generation power, the greater the decrease in the absorbance value and pH. The higher the temperature increase.

An air plasma with the characteristics of the one used in the present investigation, stimulates and enhances the fluorescence characteristics of the Rhodamine B.

Research suggestion

The present investigation showed an increase in absorbance of the solution of interest in the first 15 minutes of treatment (first measurement) and then a decrease (second measurement). It is considered to take measurements of absorbance and other variables at shorter intervals (1 minute), to analyze the behavior in a more detailed way and to determine the fluorescence.

The implementation of the same experiments at intervals of 20 minutes is also considered, with a longer exposure time (300 minutes) to know if the absorbance continues to decrease.

6. References

Alarcón F.B., Fuentes M. C., Gadea J. L., Cañete V.A. (2019). El plasma no térmico como agente de cambio de la concentración de iones Hidrógeno [H$^+$], presentes en la solución acuosa del colorante Verde Azul Doracryl X5GS 200 %. *Ciencia e Ingeniería de materiales para aplicaciones Energéticas, Handbook*, ECORFAN, ISBN: 978-607-8695-20-1. DOI: 10.35429/H.2019.1.84.93

Alarcón F.B., Montiel E., Fuentes M. C., Tabarez A., Gadea J. L, Tlatelpa A. (2022a). Behavior of the AB52 dye degradation in liquid medium by different electrical power non-thermal plasma at atmospheric pressure. Revista Mexicana De Ingeniería Química, Vol. 21, No. 2 IA2793. DOI: 10.24275/rmiq/IA2793

Alarcón F.B., Fuentes M.C., Gadea J.L., Tlatelpa A., Cañete V.A. (2022b). Evaluation of the Degradation Process of Diethyl (3H-1-Ethoxy-3-phenoxazinylidene) Ammonium Chloride in Water, after Exposure to Nonthermal Plasma at Atmospheric Pressure. Hindawi. *Journal of Chemistry*. Volume 2022, Article ID 4486227, 8 pages. ISSN: 2090-9071 (Online). https://doi.org/10.1155/2022/4486227

Alarcón F.B., Fuentes M. C., Gadea J. L. Montiel E. (2022c). Efecto de la exposición del colorante textil Rojo versatint en solución acuosa ante un plasma de aire a presión atmosférica. Ingeniería y Materiales Aplicados al Medio Ambiente T-I Handbooks, ECORFAN, ISBN: 978-607-8695-95-9. DOI: 10.35429/H.2022.9.80.93

Fahmy, A., El-Zomrawy, A., Saeed, A.M., Sayed, A.Z., Ezz El-Arab, M.A. and Shehata, H.A. (2018). Modeling and optimizing Acid Orange 142 degradation in aqueous solution by non-thermal plasma. *Chemosphere 210*, 102-109. https://doi.org/10.1016/j.chemosphere.2018.06.176

Forgacs, E., Cserh´ati, T., Oros, G. (2004). Removal of synthetic dyes from wastewaters: a review. *Environ. Int.* 30, 953–971. https://doi.org/10.1016/J.ENVINT.2004.02.001.

Goscianska, J., Ptaszkowska, M., Pietrzak, R. (2015). Equilibrium and kinetic studies of chromotrope 2R adsorption onto ordered mesoporous carbons modified with lanthanum. *Chem. Eng. J.* 270, 140–149. https://doi.org/10.1016/j.cej.2015.02.021

Hamdaoui, O. (2011). Intensification of the sorption of Rhodamine B from aqueous phase by loquat seeds using ultrasound. *Desalination* 271, 279–286. https://doi.org/10.1016/j.cis.2014.04.002.

Imam, S.S., Babamale, H.F. (2020). A short review on the removal of Rhodamine B dye using agricultural waste-based adsorbents. *Asian J. Chem. Sci*. 7, 25–37. DOI: 10.9734/ajocs/2020/v7i119013

Panda, K.K. y Mathews, A.P. (2014). Ozone oxidation kinetics of Reactive Blue 19 anthraquinone dye in a tubular in situ ozone generator and reactor: Modeling and sensitivity analyses. *Chemical Engineering Journal,* 255, 553–567. https://doi.org/10.1016/j.cej.2014.06.071

Radiul, S.M., Chowdhury, J., Goswami, A., Hazarika, S. (2022). Fluorescence spectroscopy based characterisation method for aggregation behaviour of rhodamine B (RhB) in water, ethanol, and propanol. *Laser Physics,* 32, 075602. DOI 10.1088/1555-6611/ac6e46

Radiul, S.M., Chowdhury, J., Hazarika, S. (2023). Fluorescent H-aggregates of pure rhodamine B (RhB) in glycerol, ethylene glycol, methanol and butanol under ambient condition. *J. Mol. Struct.,* 1275, Article 134606, 10.1016/j.molstruc.134606

Safenraider, A.P., Piazza, L.D., Amadeu, G. and Angelo, N. (2020). Degradation of indigo carmine in water induced by nonthermal plasma, ozone and hydrogen peroxide: A comparative study and by-product identification. *Chemosphere* 244, 1-9, https://doi.org/10.1016/j.chemosphere.2019.125502

Sharma, J.; Sharma, S.; Bhatt, U.; Soni, V. (2022). Toxic effects of Rhodamine B on antioxidant system and photosynthesis of Hydrilla verticillata. *J. Hazard. Mater. Lett.* 3, 100069. https://doi.org/10.1016/j.hazl.2022.100069

Shimizu, T., Kishimoto, N. and Sato, T. (2020). Effect of electrical conductivity of water on plasma-driven gas flow by needle-water discharge at atmospheric pressure. *Journal of Electrostatics 104*, 1-8. https://doi.org/10.1016/j.elstat.2020.103422

Varjani, S., Rakholiya, P., Ng, H.Y., You, S., Teixeira, J.A. (2020). Microbial degradation of dyes: an overview. *Bioresour. Technol.* 314, 123728 https://doi.org/10.1016/j. biortech.2020.123728.

Yagub, M.T., Sen, T.K., Afroze, S., Ang, H.M. (2014). Dye and its removal from aqueous solution by adsorption: a review. *Adv. Colloid Interface Sci.* 209, 172–184. https://doi.org/10.1016/j.cis.2014.04.002

Zhao, D., Zhang, W., Chen, C., Wang, X. (2013). Adsorption of methyl orange dye onto multiwalled carbon nanotubes. *Procedia Environ. Sci.* 18, 890–895. https://doi.org/10.1016/j.proenv.2013.04.120

Chapter 6 Analysis of Flow Direction Effects in a Single-Channel Serpentine Geometry for PEM Fuel Cells at the Cathode Side

Capítulo 6 Análisis de los efectos en la dirección del flujo en una geometría de serpentín de un canal para celdas de combustible tipo PEM en el lado del cátodo

CEBALLOS-PÉREZ, José[1], ORDÓÑEZ-LÓPEZ[1,*], Luis and SIERRA-GRAJEDA, Juan[2]

[1]*Centro de Investigación Científica de Yucatán, Unidad de Energía Renovable, Parque Científico Tecnológico de Yucatán, Carretera Sierra Papacal – Chuburná Puerto, Km 5, Sierra Papacal, Mérida, Yucatán, México.*
[2]*Facultad de Ingeniería, Universidad Autónoma del Carmen, Campus III, Avenida Central S/N, Esq. con Fracc. Mundo Maya, C.P. 24115, Ciudad del Carmen, Campeche, México.*

ID 1st Author: *José, Ceballos-Pérez* / **ORCID**: 0000-0001-7529-0346, **CVU CONAHCYT ID**: 928198

ID 1st Co-author: *Luis, Ordóñez-López* / **ORCID**: 0000-0003-1110-1934, **CVU CONAHCYT ID**: 43804

ID 2nd Co-author: *Juan, Sierra-Grajeda* / **ORCID**: 0000-0002-0565-6450, **CVU CONAHCYT ID**: 219284

Abstract

Proton Exchange Membrane (PEM) fuel cells represent a promising clean energy technology that converts hydrogen and oxygen into electricity with water as the sole byproduct. This work presents a comprehensive analysis of the impact of flow direction, specifically parallel flow and counter-flow configurations, on the performance of a single-channel serpentine geometry. The serpentine flow field pattern is widely utilized for its advantages in enhancing mass transport and reducing pressure drop. This study integrates computational fluid dynamics (CFD) simulations using an open-source toolbox based on C++ to investigate the influence of flow direction on the liquid water saturation distribution within the cell. The analysis of liquid water accumulation is essential, as it directly affects the overall performance and durability of the PEM fuel cell. Saturation contour maps are obtained at 0.52 V for each geometry. The results show that water saturation tends to accumulate at the edges of the electrode-membrane assembly, and the counter-parallel flow exhibits the major saturation distribution.

Resumen

Las celdas de combustible de membrana de intercambio de protónico (PEM) representan una prometedora tecnología de energía limpia que convierte el hidrógeno y el oxígeno en electricidad con agua como único subproducto. Este trabajo presenta un análisis del impacto de la dirección del flujo, específicamente las configuraciones de flujo paralelo y contraflujo, en el rendimiento de una geometría de serpentín de un canal. La geometría tipo serpentín es ampliamente utilizada por sus ventajas para mejorar el transporte de masa y reducir la caída de presión. En este estudio, se integran simulaciones de dinámica de fluidos computacional (CFD) utilizando un código abierto basado en C ++ para investigar la influencia de la dirección del flujo en la distribución de saturación de agua líquida dentro de la celda. El análisis de la acumulación de agua líquida es esencial, ya que afecta directamente al rendimiento general y la durabilidad de la celda. Los mapas de contorno de saturación se obtienen a 0.52 V para cada geometría. Los resultados muestran que la saturación de agua tiende a acumularse en los bordes del conjunto electrodo-membrana, y el flujo contraparalelo exhibe la mayor distribución de saturación.

1. Introduction

Proton Exchange Membrane (PEM) fuel cells are a promising alternative as a clean energy technology, offering a pathway to sustainable power generation for various applications [1]. A PEM fuel cell is an electrochemical device that converts chemical energy directly into electrical energy through electrochemical reactions. The flow channels ensure optimal reactant distribution, efficient mass transport, and overall cell performance among these components. These flow channel designs consider flow directions and geometry, with flow and counter-flow configurations emerging as vital elements in serpentine channel designs[2]. Due to their simplicity and effectiveness, serpentine flow channels are of interest in PEM fuel cell design. In a serpentine flow channel, reactant gases traverse a winding path along the electrode surfaces, enhancing interaction between the gases and the catalyst layers. This geometry optimizes the utilization of catalyst sites while promoting efficient water management [3]. The reactant gases typically flow through these channels either in the same direction (co-flow) or opposite directions (counter-flow) to the serpentine path[4]. Understanding the implications of these flow configurations is crucial for maximizing fuel cell performance. In this work, three different fuel cell configurations are analyzed to observe the behavior of the polarization curves in a single-channel serpentine flow path with co-flow and counter-flow directions using OpenFOAM (Open Field Operation and Manipulation), an open-source toolbox based on C++, to solve a 3D multiphase non-isothermal model [5] with three different configurations of single-channel serpentine geometry and flow directions.

2. Methodology

A 3D representation of the computational domain of the numerical model is shown in Fig. 1. The domain consists of the main components of a PEM fuel cell: bipolar plates (BP), gas flow channels (GFC), gas diffusion layers (GDL), catalyst layers (CL), and the protonic membrane for both the anode and cathode; where the red line represents the location where the electrochemical reaction occurs.
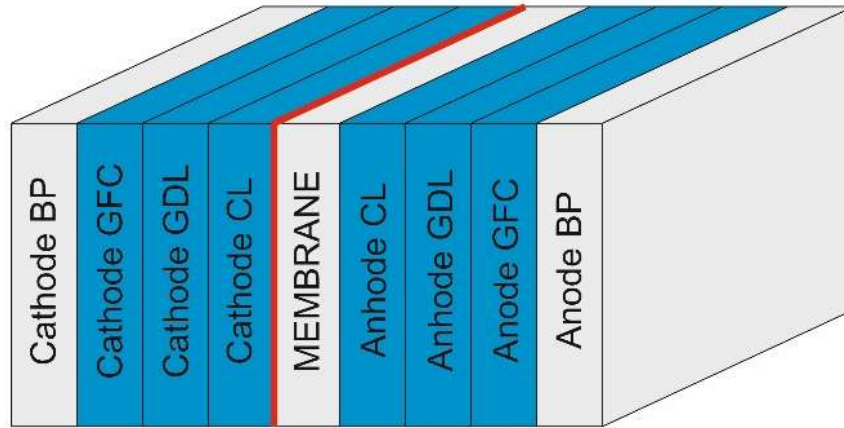
Figure 1 Computational domain and its components

Table 1 shows the governing equations and source terms. Modeling the flow through the fuel cell components used the Navier-Stokes equations and considered isotropic porous media. For the continuity equation (Eq. 1), ρ_g is the fluid density, $\vec{U}_g$ the velocity vector, S_l is the mass source term due to phase change, where, in Eq. 2, C_r is the condensation rate, ε the porosity, s the water saturation, x_{WV} the water vapor mass fraction, p_{sat} water saturation pressure, R the ideal gas constant, M_{H_2O} stands for the molecular weight of water. In the momentum equation (Eq. 3) p_g, μ_g, and S_M represent the pressure gradient, dynamic viscosity, and momentum source term, respectively. S_M is the Darcy resistance in the porous media, where K_g is the permeability of the gas phase. In the species transport equation (Eq. 5) y_i and D_g^{eff} are the species i mass fraction and the effective diffusion coefficient of each gas, respectively. In the liquid water transport equation (Eq. 9), the terms D_l stands for the diffusivity of liquid water where ρ_l, k_l and μ_l represents the fluid density, thermal conductivity, and dynamic viscosity of liquid water, respectively, and p_c is the capillary pressure. For the energy equation (Eq. 6) $\rho_{mix}, C_{p_{mix}}, k_{mix}, T$, stands the fluid density of the gas mixture, the specific heat capacity of the gas mixture, the thermal conductivity of the gas mixture, and temperature, respectively. S_E^{reac} and S_E^{PC} are the energy source terms due to the heat released by the electrochemical reactions and water phase change, where δ_{MEA} is the membrane electrode assembly thickness, η_{act} are the activation losses, n is the number of electrons, F is the Faraday constant, and h_{mfg} is the latent heat.

Table 1 Governing equations

| Description	Equation	
Continuity equation	$\nabla \cdot \left(\rho_g \vec{U}_g\right) = -S_l$	(1)
Mass source term due to phase change	$S_l = -C_r \dfrac{\varepsilon(1-s)\left(x_{WV}p_g - p_{sat}\right)}{RT} M_{H_2O}$	(2)
Momentum equation	$\nabla \cdot \left(\rho_g \vec{U}_g \vec{U}_g\right) = -\nabla p_g + \nabla \cdot \left(\mu_g \nabla \vec{U}_g\right) + S_M$	(3)
Darcy source term	$S_M = -\dfrac{\mu_g \vec{U}_g}{K_g}$	(4)
Specie transport equation	$\nabla \cdot \left(\rho_g \vec{U}_g y_i\right) = \left(\nabla \cdot \rho_g D_g^{eff} \nabla y_i\right)$	(5)
Energy equation	$\nabla \cdot \left(\rho_{mix} C_{p_{mix}} \vec{U}_g T\right) = \nabla \cdot \left(k_{mix} \nabla T\right) + S_E^{reac} + S_E^{PC}$	(6)
Energy source term due to the heat released by the electrochemical reactions	$S_E^{reac} = \dfrac{1}{\delta_{MEA}}\left(\eta_{act} - \dfrac{T\nabla S}{nF}\right)$	(7)
Source term due to water phase change	$S_E^{PC} = S_l h_{mfg}$	(8)
Liquid water transport equation	$\nabla \cdot \left(\rho_l D_l \nabla s\right) - \nabla \cdot \left(\rho_g \vec{U}_g s\right) = S_l$	(9)
Diffusivity of liquid water	$D_l = \dfrac{\rho_l k_l}{\mu_l}\dfrac{\partial p_c}{\partial s}$	(10)

Table 2 summarizes the initial conditions for the steady-state simulation. Here, Dirichlet boundary conditions are applied at the fluid inlets for velocity, temperature, and mass fractions of both the anode and the cathode gas flow channels. Neumann boundary conditions are applied at the fluid outlets for mass fractions, temperature and saturation, with their gradients set to zero in the flow direction.

Table 2. Boundary and initial values

Component	Momentum	Energy	Species transport	Liquid water transport
Anode inlet	$U_{fuel} = 9\ m/s$ $\nabla p_{air} = 0$	$T = 333\ K$	$y_{H_2} = 0.727$ $y_{H_2O} = 0.273$	$s = 0$
Anode outlet	$p_{air} = 506{,}625\ Pa$	$\nabla T = 0$	$\nabla y_{H_2} = 0$ $\nabla y_{H_2O} = 0$	$\nabla s = 0$
Cathode inlet	$U_{air} = 9\ m/s$ $\nabla p_{air} = 0$	$T = 333\ K$	$y_{O_2} = 0.225$ $y_{H_2O} = 0.024$ $y_{N_2} = 0.751$	$s = 0$
Cathode outlet	$p_{air} = 506{,}625\ Pa$	$\nabla T = 0$	$\nabla y_{O_2} = 0$ $y\nabla_{H_2O} = 0$ $\nabla y_{N_2} = 0$	$\nabla s = 0$
Walls	$U = 0$	$T = 333\ K$	$\nabla y = 0$	$\nabla s = 0$

Figure 2 shows the different flow configurations to obtain the polarization curves with an open-source toolbox based on icoFoam, an OpenFOAM application that solves the incompressible laminar Navier-Stokes equations using the PISO algorithm and discretizes the equations based on the finite volume method. The Preconditioned bi-Conjugate Gradient (PBiCG) method was used to find convergence in the energy equation, and Preconditioned bi-Conjugate Gradient Stabilized (PBiCGStab) for other variables (continuity, momentum, species transport, energy, and liquid water transport). For all variables, the convergence criterion was a residual of $1\text{x}10^{-9}$.

Figure 2 Flow configurations for the different geometries of the single-channel serpentine flow paths

Co-flow [Cell A]
a)

Counter-flow [Cell B]
b)

Counter-flow [Cell C]
c)
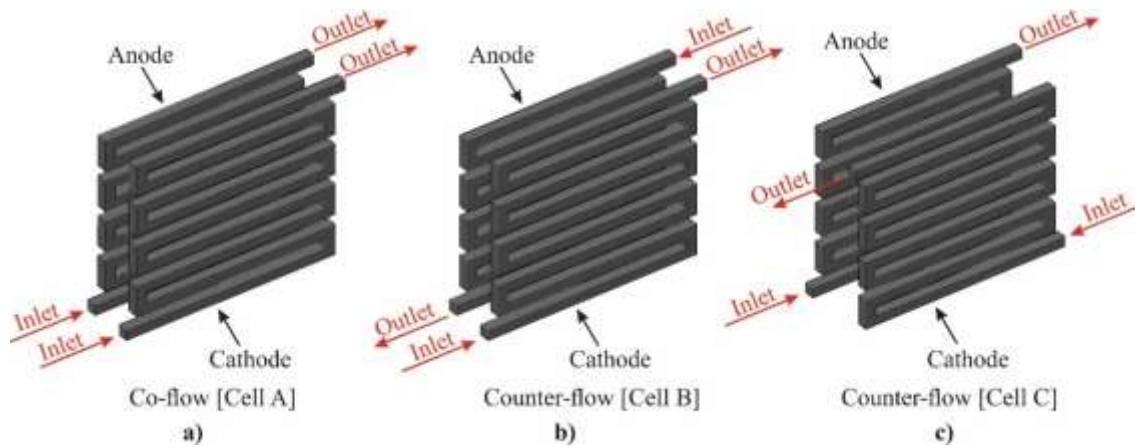
Results

Figure 3 shows the polarization curves where cell B exhibits the major current density, then cell A, and finally cell C. However, cell C performs a maximum current density at 0.52 V, where the calculation stops for this configuration. Therefore, the contour maps of the current density at the interface CL-membrane at the cathode side in Figure 4 are obtained at 0.52 V. It is noticed that even when cell B exhibits the greatest current density, the best distribution belongs to cell A. In other words, the best performance is shown by cell A, specifically in this study, where the difference between the current density of A and B is 0.53 %.

Figure 3 Polarization curves of the different flow configurations
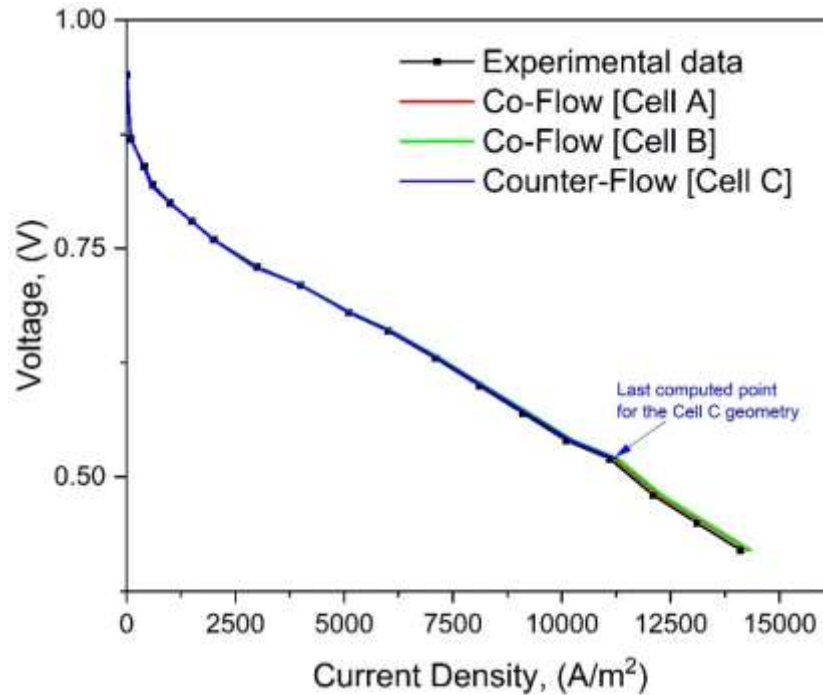
Figure 4 shows the distribution of the current density for the three flow configurations at 0.52 V, where it can be seen that cell B has a minor exploited active area. This is due to the delay of the reactant gases that need time to meet and associate the electrons and proton to form water at the cathode side. Therefore, cell A exhibits a better distribution with a parallel flow path between the anode and the cathode, even when the current density is lower. Cell C finds it challenging to reach the maximum point of the experimental data due to the limits of the model and the attempt to simulate complex geometries with the same work conditions.

Cell A's co-flow configuration offers a uniform distribution and guarantees a consistent inflow of reactant gases across the entirety of the electrode surface. This uniform distribution cultivates balanced electrochemical reactions, maximizing the use of catalyst sites and augmenting cell performance. With both reactant gases following the same trajectory, the risk of reactant depletion close to the outlet is minimized.

On the other hand, in cell B, the counter-flow can foster the uneven distribution of reactants along electrode surfaces. Concentrations of reactants may taper off near the outlet, potentially causing localized inefficiencies and compromising overall performance. The counter-flow setup impacts mass transport dynamics. The motion of reactant gases against one another influences the rate of mass transport, potentially influencing the pace of electrochemical reactions and, consequently, the overall cell performance. Managing water becomes intricate under counter-flow conditions, as water vapor movement from cathode to anode occurs against the flow direction. This can lead to water accumulation at the cathode, affecting proton conductivity and potentially causing flooding, as shown in Figure 5. The distribution of the liquid water saturation in cell B is major through the active area of the electrode-membrane assembly.

Figure 5 Saturation distribution at the interface CL-membrane at the cathode side at 0.52 V
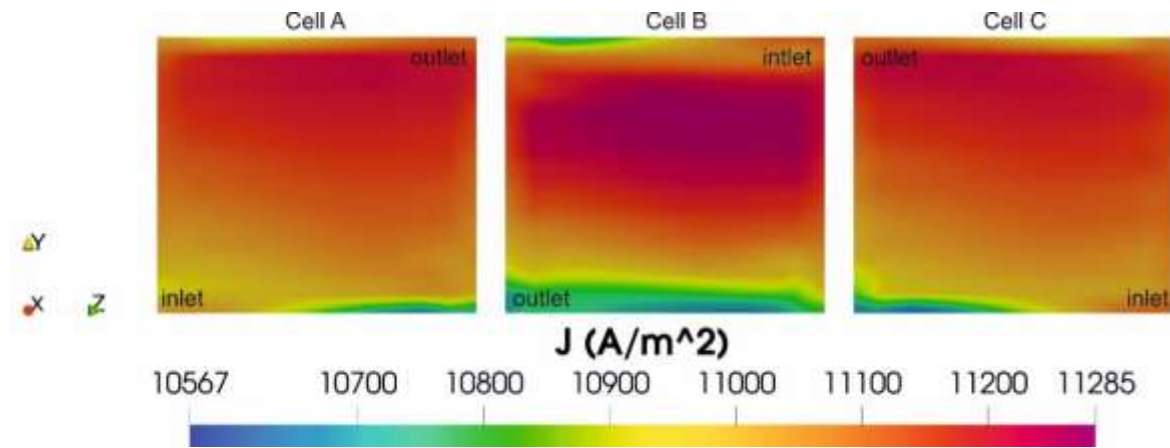
Figure 4 Current density at the interface CL-membrane at the cathode side at 0.52 V.
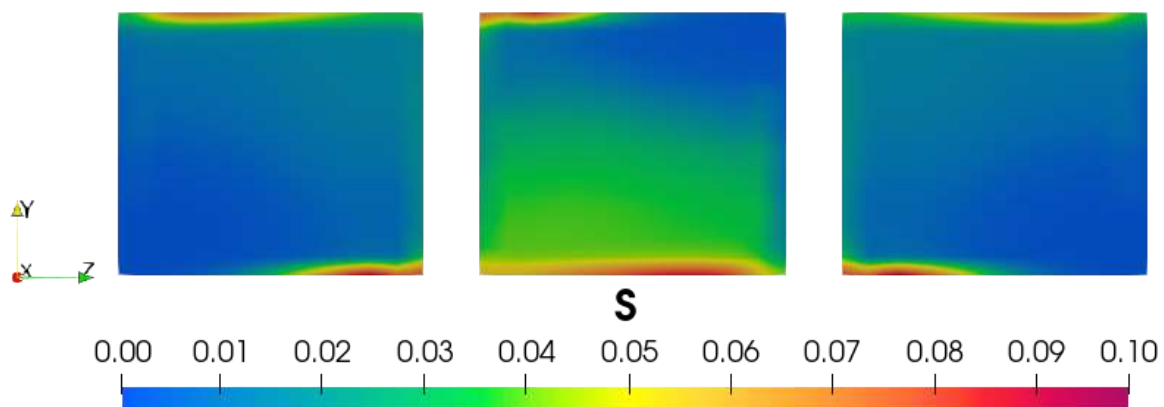
Figure 6 shows the temperature distribution where cell B exhibits an uneven temperature distribution adverse to the performance of the fuel cell. The electrochemical reactions might be more pronounced in the areas with higher temperatures, leading to accelerated degradation of the membrane and catalysts. This could result in increased resistive losses and lowered overall efficiency. The uneven temperature distribution might also indicate a cooling or thermal management issue within the fuel cell system. Addressing this abnormality is crucial to avoid long-term damage and maximize the cell's performance.

Figure 6 Temperature distribution at the interface CL-membrane at the cathode side at 0.52 V.
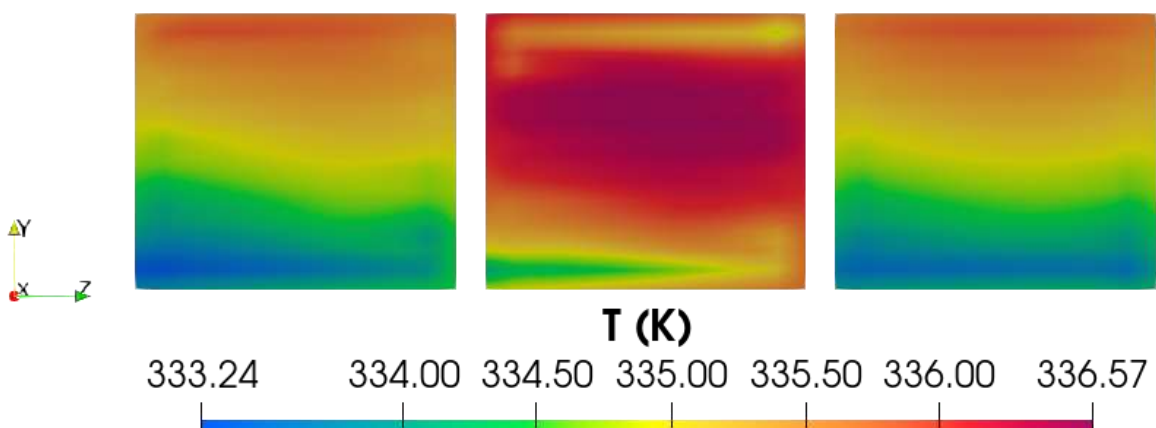
Figure 7 displays the distribution of the ionic conductivity where cell B experience a lower distribution at the zone where the cathode outlet meets the inlet of the anode side and consists of the uneven distribution of the current density and temperature in Figure 1 and 2, respectively. The electrochemical reactions within the cell are well-balanced, and the membrane conductivity is optimal. The overall efficiency is commendable, with minimal voltage losses due to resistive, activation, and mass transport losses. The temperature distribution across the cell is uniform, indicating effective cooling mechanisms and thermal management.

Figure 7 Ionic conductivity distribution at the interface CL-membrane at the cathode side at 0.52 V
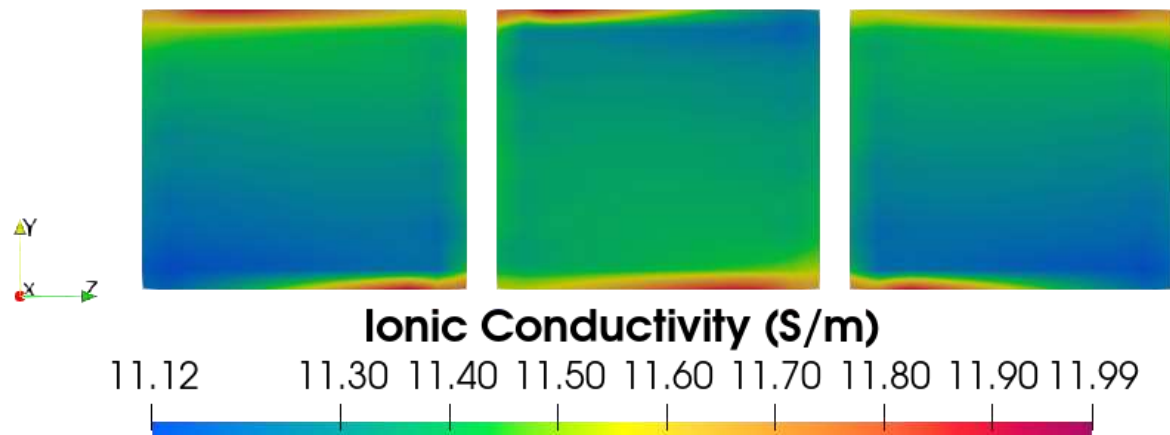
Conclusions

The interaction of co-flow and counter-flow configurations within serpentine channels significantly influences the performance of PEM fuel cells. Co-flow optimizes reactant distribution, staving off reactant depletion and encouraging even reactions. Meanwhile, counter-flow introduces the complexities of reactant distribution, mass transport, and water management. The selection of the most suitable flow configuration hinges on the specific requirements of the fuel cell, operational conditions, and the need to harmonize diverse performance aspects.

References

[1] Abdelkareem, M. A., Elsaid, K., Wilberforce, T., Kamil, M., Sayed, E. T., & Olabi, A. (2021). Environmentalaspects of fuel cells: A review. *Science of the Total Environment*, *752*, 141803. https://doi.org/10.1016/j.scitotenv.2020.141803

[2] Kone, J.-P., Zhang, X., Yan, Y., & Adegbite, S. (2018). An Open-Source Toolbox for Multiphase Flow Simulation in a PEM Fuel Cell. *Computer and Information Science*, *11*(3), 10. https://doi.org/10.5539/cis.v11n3p10

[3] Martins Belchor, P., Camargo Forte, M. M., & Ortiz Suman Carpenter, D. E. (2012). Parallel serpentine-baffle flow field design for water management in a proton exchange membrane fuel cell. *International Journal of Hydrogen Energy*, *37*(16), 11904–11911. https://doi.org/10.1016/j.ijhydene.2012.05.091

[4] Wang, X. D., Duan, Y. Y., Yan, W. M., & Peng, X. F. (2008). Effects of flow channel geometry on cell performance for PEM fuel cells with parallel and interdigitated flow fields. *Electrochimica Acta*, *53*(16), 5334–5343. https://doi.org/10.1016/j.electacta.2008.02.095

[5] Wang, X. D., Huang, Y. X., Cheng, C. H., Jang, J. Y., Lee, D. J., Yan, W. M., & Su, A. (2010). An inverse geometry design problem for optimization of single serpentine flow field of PEM fuel cell. *International Journal of Hydrogen Energy*, *35*(9), 4247–4257. https://doi.org/10.1016/j.ijhydene.2010.02.059

Chapter 7 Feasibility study of alloy Al$_{80}$Mg$_{20}$% weight, heat-treated as energy material

Capítulo 7 Estudio de la factibilidad de la aleación Al$_{80}$Mg$_{20}$%peso, tratado térmicamente como material energético

REDA-CRUZ, Alfredo†, PÉREZ-MONTEJO, Salatiel, CALAN-CANCHE, Damian and FLORES-CHAN, José Enrique*

Universidad Autónoma del Carmen, Campus III, Facultad de Ingeniería, Avenida Central S/N, Esq. Con Fracc. Mundo Maya, C.P. 24115, Ciudad del Carmen, Campeche, México.

ID 1st Author: *Alfredo, Reda-Cruz* / **ORC ID:** 0000-0002-8767-3616, **CVU CONAHCYT ID:** 952544

ID 1st Co-author: *Salatiel, Pérez-Montejo* / **ORC ID:** 0000-0002-1750-0154, **CVU CONAHCYT ID:** 594590

ID 2nd Co-author*: José Damian, Calan-Canche* / **ORC ID:** 0000-0001-6688-4468, **CVU CONAHCYT ID:** 415663

ID 3rd Co-author: *José Enrique, Flores-Chan* / **ORC ID:** 0000-0003-4714-686X, **CVU CONAHCYT ID:** 175430

A. Reda, S. Pérez, D. Calan and J. Flores

*Jeflores@pampano.unacar.mx

Abstract

The purpose of this research is to evaluate the effect of the aging heat treatment and the electrochemical behavior of the alloy (Al$_{80}$Mg$_{20}$% weight), for energy purposes through corrosion processes. Hydrogen generation sources currently have a high cost, and their large-scale implementation has been of great interest in research. Aluminum and its alloys have great potential as energetic materials due to their low cost, performance, and availability. The Aluminum-Magnesium alloy Al$_{80}$Mg$_{20}$% weight was obtained by casting and subsequently subjected to an aging heat treatment that favored microstructural heterogeneity and the precipitation of the β intermetallic phase (Al$_3$Mg$_2$). This Al$_{80}$Mg$_{20}$% weight alloy was characterized by optical microscopy, scanning electron microscopy and X-ray diffraction. The electrochemical behavior of the Al$_{80}$Mg$_{20}$% weight alloy was also characterized by Open Circuit Potential (PCA), Potentiodynamic Polarization Curves (CPP) and Electrochemical Impedance Spectroscopy (EIE). The results indicated a change in the microstructural morphology of the polygonal type and the presence of cracks at the grain boundaries, as well as the presence of the α Al (Mg) phase and a β (Al$_3$Mg$_2$) intermetallic secondary phase, with a higher precipitation in the grain boundaries, both with a cubic crystallographic system. Through the PCA, corrosion current density (Icorr), anodic and cathodic Tafel slopes (β and α). They showed that both samples are susceptible to embrittlement corrosion, with the rate of corrosion being more accentuated in the sample after Al$_{80}$Mg$_{20}$-6TT350°C.

Corrosion, Intermetallic, Cracking, Embrittlement

Resumen

El propósito de esta investigación es evaluar el efecto del tratamiento térmico de envejecido y el comportamiento electroquímico de la aleación (Al$_{80}$Mg$_{20}$% peso), para fines energéticos mediante procesos de corrosión. Las fuentes de generación de hidrógeno en la actualidad tienen un alto costo y su implementación a gran escala ha sido de gran interés. El aluminio y sus aleaciones tienen mucho potencial como materiales energéticos por el bajo costo, el rendimiento y disponibilidad. La aleación de Aluminio-Magnesio (Al$_{80}$Mg$_{20}$% peso), se obtuvo por fundición y posteriormente se le practicó un tratamiento térmico de envejecido que favoreció la heterogeneidad microestructural y la precipitación de la fase intermetálica β (Al$_3$Mg$_2$). La aleación Al$_{80}$Mg$_{20}$%peso, se caracterizó por Microscopía óptica, Microscopia electrónica de barrido y Difracción de rayos X. También se caracterizó el comportamiento electroquímico de la aleación Al$_{80}$Mg$_{20}$% peso mediante Potencial a circuito abierto (PCA), Curvas de polarización potenciodinámica (CPP) y Espectroscopia de Impedancia Electroquímica (EIE). Los resultados indicaron un cambio en la morfología microestructural del tipo poligonal y presencia de agrietamientos en los límites de grano, así como la presencia de la fase α Al (Mg) y una fase secundaria intermetálica β(Al$_3$Mg$_2$), con una mayor precipitación en los límites de grano, ambas con un sistema cristalográfico cubico. A través del PCA, densidad de corriente de corrosión (Icorr) y pendientes anódica y catódica de Tafel (β y α), revelaron que ambas muestras son susceptibles a la corrosión por fragilización, siendo más acentuada la velocidad de corrosión en la muestra Al$_{80}$Mg$_{20}$-6TT350°C.

Corrosión, Intermetálico, Agrietamientos, Fragilización

1. Introduction

Aluminum alloys of the 5xxx series, have Mg as the main alloying element, its maximum solubility in Al is 17.4% and its precipitation occurs at room temperature in cast alloys with 10% Mg [1]. It has been studied in various applications [1,2], however, research has emerged suggesting its application as an energetic material through corrosive processes [3,4]. Aluminum reacts rapidly with atmospheric oxygen forming a thin layer of aluminum oxide (Al2O3) on its surface. The Al2O3 layer prevents oxygen from coming into contact with the metal, providing protection from corrosion deterioration, making it a metallic material with remarkable corrosion resistance. In recent research [5,6], the behavior of intergranular corrosion in aluminum alloys forming galvanic microcells in saline aqueous media has been studied. Aluminum due to its equivalent weight is an excellent hydrogen producer, due to its negative redox potential [22,24], aluminum reacts easily with water, producing gaseous hydrogen according to equation (1) [7,8] and Al (OH)$_3$.

$$2Al + 3H_2O \rightarrow 3H_2 + Al_2O_3 \qquad (1)$$

In equation (1), two moles of Al are observed reacting with three moles of H_2O, producing 3 moles of H_2 and Al_2O_3. However, the reactions of aluminum with NaOH in aqueous media produce $3H_2$, in the following equations [7,8]:

$$2Al + 6H_2O + 2NaOH \rightarrow 2Al(OH)_4 + 3H_2 \tag{2}$$

$$NaAl(OH)_4 \rightarrow NaOH + Al(OH)_3 \tag{3}$$

$$2Al(OH_3) \rightarrow Al_2O_3 + 3H_2 \tag{4}$$

In equation (2) and (3), it is observed that 2 moles of Al react with 6 moles of H2O and 2 moles of NaOH, resulting in 2 moles of $Al(OH)_4$ and $NaAl(OH)_4$ and 3 moles of H_2. Equation (3) shows the decomposition of $(NaAl(OH)_4)$ into NaOH and $Al(OH)_3$ to produce one mole of Al_2O_3 and 3 moles of H_2O (see Equation (4)). The H_2 produced through these reactions in aqueous solution can be used in mechanical elements, electronic devices, batteries, fuel cells, among others.

2.- Experimental Methodology

2.1.- Materials and heat treatment

For this research, commercial aluminum Al-6063 and magnesium at 99.99% purity were used. The stoichiometric ratio for 2 kg of castings to obtain the alloy (Al80Mg20% weight) is shown in Table 1.

Table 1 Stoichiometric ratio to obtain the alloy Al80Mg20%wt

Aluminum (Al)	1632.38 g
Magnesium (Mg)	367.6 g

Source: Own Elaboration

The melting was performed in a PREFINSA model HR C4/1200 electric resistance furnace (see Figure 1a), at a temperature of 715°C. A graphite crucible was introduced into the furnace to obtain a homogeneous temperature. Then, pieces of Al and Mg were added inside the crucible for melting, placing first the one with the highest melting point and then the one with the lowest melting point. After controlling the melting and the total homogeneity of the casting, the molten metals were poured into a commercial steel mold with rectangular geometry and shape, then the casting was left to cool for 12 hours at room temperature, after which the mold was demolded to obtain the Al80Mg20% wt.% alloy (see Figure 1b).

Figure 1 PREFINSA electric furnace b) Specimens (Al80Mg20% weight))
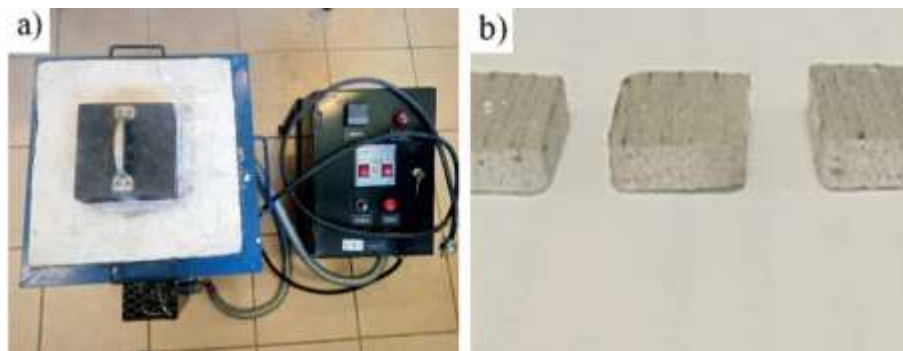
Source: Own Elaboration

To determine the influence of the microstructure and the phases present in Al80Mg20 wt.%, a heat treatment was designed consisting of a solubilization at 300°C (Al80Mg20-24TT) and 350°C (Al80Mg20- 6TT), for 24 and 6 hours, respectively. In both metallurgical situations, they were quenched in ice water at -3°C [9]. Finally, all the specimens were subjected to aging for 6 hours at179°C, allowing them to cool to room temperature, in order to promote the growth of intermetallic phases in this alloy. Figure 1.1 shows the heat treatment diagram used.

Figure 1.1 Heat treatment design
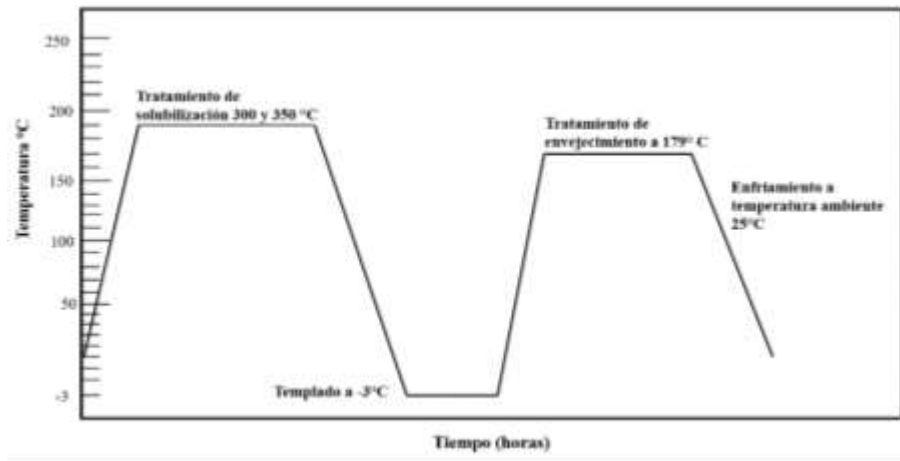
Source: Own Elaboration

2.2. Microstructural characterization of Al80Mg20, Al80Mg20-24TT300 and Al80Mg20-6TT350 alloys

For microstructural characterization, 10 mm x 10 mm x 10 mm specimens were cut from Al80Mg20, Al80Mg20-24TT300°C and Al80Mg20-6TT350°C alloys and roughened with SiC sandpaper from 180 to 2500 grit size. They were then polished to a mirror finish using 1/10μm, 1/2μm and 3μm diamond paste according to ASTM E3-11 [10]. The specimens were dried with distilled water and hot air. Finally, the specimens were chemically attacked with Keller solution (2 ml HF, 3 ml HCl, 5 ml HNO3, 190 ml H2O). The microstructural characterization of the Al80Mg20, Al80Mg20, 24TT300 and Al80Mg20-6TT350 alloy was carried out using an optical microscope (OM), ZEISS Omax-01 brand and a scanning electron microscope (SEM), JEOL-JSM brand. The phases present in the study specimens were identified using an ADP 2000 diffractometer, with Cu-Kα radiation and a wavelength (λ) =1.5406 Å and voltage of 35kV and a current emission of 30mA. The data were collected over a 2θ range from 20° to 80° with a step of 0. 0166.

2.2. Electrochemical tests

Specimens of 1.2 cm x 1.2 cm x 1 cm of Al80Mg20, Al80Mg20, Al80Mg20-24TT300°C and Al80Mg20-6TT350°C alloys were cut and surface prepared. Surface roughing of one side of the samples consisted of sanding with silicon carbide (CSi), with grit sizes from 100 to 600, achieving an effective working surface of 1 cm2. Synthetic seawater at pH: 8.2 [11], a conventional three-electrode cell consisting of: a calomelane reference electrode (ERC), a graphite rod as auxiliary electrode (EA) and Al80Mg20, Al80Mg20-24TT300°C and Al80Mg20-6TT350°C alloy specimens, as working electrode (ET), were used. With the intention of evaluating the influence of the thermal treatment on the specimens and to know the possibility of being used as an energetic material for the generation of (H2), electrochemical tests consisting of potentiodynamic polarization curves (CPP) [12] and resistance to polarization (Rp) [13] were practiced. The CPPs were performed over a range of -1000 mV to -2000 mV with respect to the open circuit potential (OCP) at a sweep speed of 1 mV/s. Corrosion current density was calculated by Tafel extrapolation, considering a range of ±120 mV. All tests were performed at room temperature on an ACM Instruments potentiostat/galvanostat.

3. Results

3.1 Microstructural characterization of Al80Mg20, Al80Mg20-24TT300 and Al80Mg20-6TT350 alloys

Figure 1.2, shows the morphological evolution in cast (Al80Mg20%wt) and heat-treated (Al80Mg20-24TT300°C and Al80Mg20-6TT350°C) condition. The MO shown in Figure 1.2a, revealed the presence of an α Al phase (Mg solid solution) with a globular morphology, surrounded by an intermetallic β secondary phase (Al3Mg2), both with an FCC crystalline structure [14,15,16]. After solubilization heat treatment at 300°C for 6 hours, the micrograph (Figure 1.2b) revealed precipitated particles in the form of elongated globules. However, after 350°C for 24 hours in (Figure 1.2c), precipitation is observed in the form of thick elongated lines, white areas where precipitation is delayed and black areas where it is accelerated [17,18]. Hamana et.al (2018), indicated that the precipitation is the β-phase (Al3Mg2), which originates due to the increase in temperature between ranges of 50°C to 350°C. The morphology obtained in the microstructures has been previously related to similar transformations at various Mg weight contents [18], with longer aging times. The phases studied are clearly identified in the Al-Mg phase diagram [19] and related to the results obtained in X-ray diffraction, (Figure 1.3).

Figure 1.2 Alloy morphological evolution a) Al80Mg20 b) Al80Mg20-6TT350 and c) Al80Mg20-24TT300 heat-treated Al80Mg20-24TT300
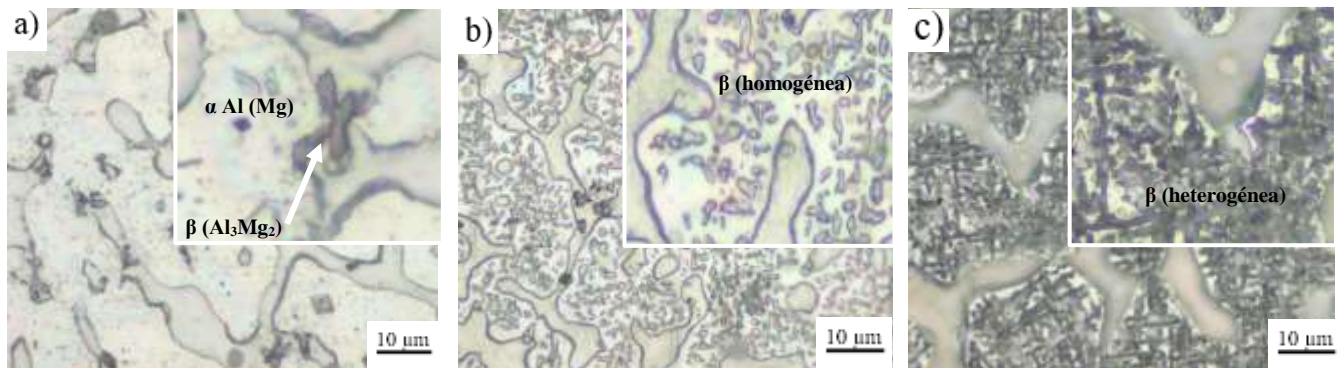
Source: Own Elaboration

Figure 1.3, shows the X-ray diffractograms of Al80Mg20, Al80Mg20-24TT300°C and Al80Mg20-6TT350°C alloys. Two main phases were identified: the Al (Mg) solid solution and the precipitation of the β(Al3Mg2).

Figure 1.3 X-ray diffraction a) Al80Mg20 b) Al80Mg20-6TT350°C and c) Al80Mg20-24TT300°C
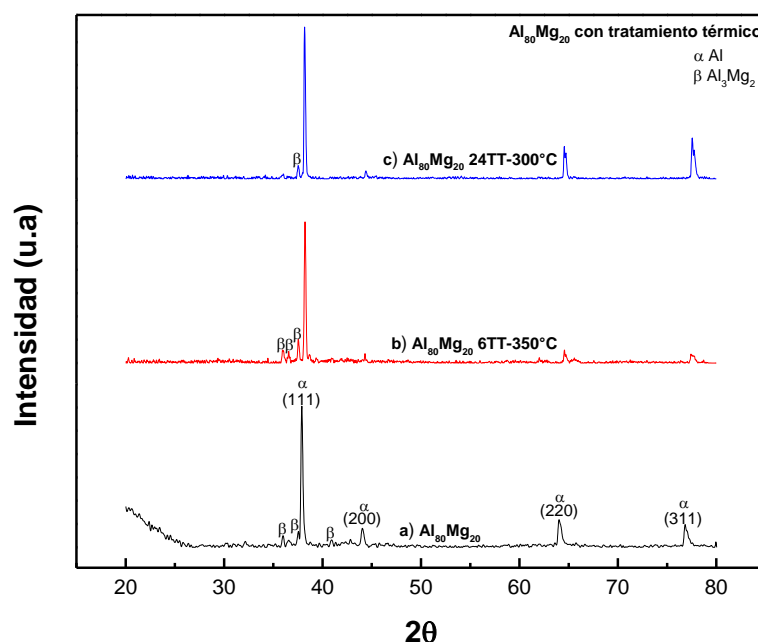
Source: Own Elaboration

In Figure 1.4a, the SEM image of the microstructure corresponding to the Al80Mg20 alloy is observed. The microstructure is composed of an Al matrix (Mg in solid solution) and a secondary intermetallic β-phase (Al3Mg2). Corrosion products were observed in each of the samples, although well differentiated between the different metallurgical conditions, these in general are caused by electrochemical attack. Areas with grain boundary cracking were also identified, this could be due to the redistribution and growth of β (Al3Mg2), which occurs preferentially at the grain boundaries.

The presence of cracking is of interest because it has been reported [5], that this phenomenon is caused by hydrogen embrittlement (H2), referring to equation (1) [7,8]. However, in the (Figure 1.4b, 1.4c), Al80Mg20-6TT350°C and 24TT300°C alloys, the presence of cracking increases at the grain boundaries due to the dissolution of the Al2O3 surface layer under the influence of the intermetallic β(Al3Mg2) phase and solution chemistry, thus causing an acceleration in intergranular corrosion [20,25,26]. In the literature Abdullah *et al.* (2018), indicated that as the NaOH solution increases, the oxide layer on the surface of Al (Mg in solid solution) dissolves faster [7] and that, in turn, more Al contact area can be accessed to react with NaOH and increase the corrosive process.

Figure 1.4 Scanning electron microscopy a) Al80Mg20 b) Al80Mg20-6TT350°C and c) Al80Mg20-24TT300°C.
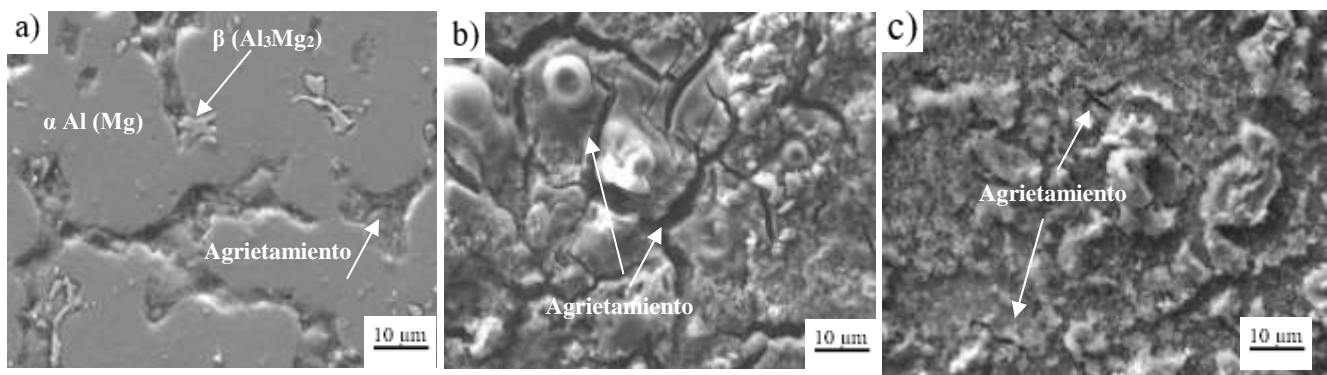
Source: Own Elaboration

3.2. Electrochemical behavior of Al80Mg20, Al80Mg20-24TT300 and Al80Mg20-6TT350 alloys

Figure 1.4 shows the CPP of the alloys Al80Mg20, Al80Mg20-24TT300 and Al80Mg20-6TT350 in synthetic seawater at pH 8.2. The interest in studying the corrosion of this alloy in saline solution, as a hydrogen generator it is known that aluminum produces 2.9 mol H2/m2 per year [5], compared to steels that produce 50% less, so aluminum-based alloys have an interesting energetic potential. Furthermore, in the tests performed in this research it was observed that the microstructure plays an important role in the passivation of the material because the pH was the same for each sample.

The potentiodynamic curves showed that the current density (icorr), increased significantly due to pitting corrosion in point areas, in values ranging from 2.03 mA/cm2 to 3.77 mA/cm2 respectively. However, the potential values did not show significant changes staying around between -1150 mV and -1260mV, indicating that passive films were formed in this potential range [23]. The kinetic parameters obtained from the intersection method are shown in Table 1.2. The icorr was calculated from the Stern-Geary formula at low field, applying a range of ±20 mV. Rp kinetics showed values between 244 Ω*cm2 and 400Ω*cm2. The potentiodynamic results showed a charge transfer controlled behavior, with a slight tendency to form a passive Al2O3 layer as shown in Figure 1.4.

Similarly, the alloy with the presence of the α phase Al (Mg solid solution), acts as a cathode while the β phase (Al3Mg2), acts as an anode, these phases promote the formation of a micro galvanic cell. It can be deduced that the most favorable condition for hydrogen (H2) generation, is the Al80Mg20-24TT300 alloy, with more active Ecorr values [5,21].

Table 1.2 Kinetic parameters obtained from the potentiodynamic polarization curves of the alloy in its different metallurgical conditions: Al80Mg20, Al80Mg20-24TT300°C and Al80Mg20-6TT350°C

Sample	E_{corr} (mV)	I_{corr} (mA)	Ba (mV década)	Bc (mV década)	Rp ($\Omega*cm^2$)
Al$_{80}$Mg$_{20}$	-1222.18	2.03	-46.91	59.58	400
Al$_{80}$Mg$_{20}$-6TT350°C	-1153.89	2.57	-18.02	20.56	285.71
Al$_{80}$Mg$_{20}$-24TT300°C	-1263.72	3.77	-60.45	97.81	244.82

Source: Own Elaboration

Figure 1.4 Potentiodynamic polarization curves Al80Mg20 b) Al80Mg20-6TT350°C and c) Al80Mg20-24TT300°C
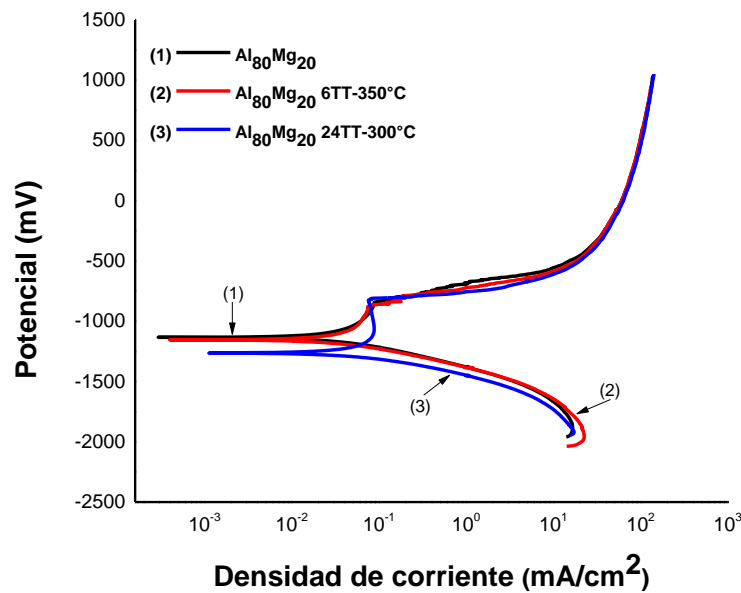
Source: Own Elaboration

Conclusions

The following conclusions can be drawn from this research study:

1. Two main phases were observed from the X-ray diffraction spectra, the Al(Mg solid solution) phase and the secondary interdendritic intermetallic β-phase (Al3Mg2).

2. The microstructure of the material showed changes due to the effects of the thermal treatment of solubilization at 300°C and 350°C for 24 and 6 hours in which precipitates of the β phase (Al3Mg2) were observed in the form of thick and elongated lines due to the nucleation in dispersed zones.

3. The microstructure of the Al80Mg20 base material showed a polygonal type granular behavior corresponding to AlMg alloys.

4. The Al80Mg20-6TT350°C and 24TT300°C showed qualities necessary for the evolution of hydrogen by embrittlement due to the effects of more active potentials; however, the 24TT300°C sample is where the corrosion rate was more accentuated.

Acknowledgments

References

[1] Zhao *et al* (2014). *The role of grain boundary plane orientation in the β phase precipitation of an Al–Mg alloy.* Scripta Materialia, p.p 1-4, https://doi.org/10.1016/j.scriptamat.2014.07.003 .

[2] Yi, G., Cullen, D.A., Littrell, K.C. *et al. Characterization of Al-Mg Alloy Aged at Low Temperatures.* Metall Mater Trans A 48, Pages 2-3. https://doi.org/10.1007/s11661-017-3992-2

[3] Martínez *et al* (2019). *Hydrogen generation by aluminum alloy corrosion in aqueous acid solutions promoted by nanometal*: kinetics study. Renewable Energy. Pages 1-7. https://doi.org/10.1016/j.renene.2019.08.103

[4] Dudoladov *et al* (2016). *Generation of hydrogen by aluminum oxidation in aqueous solutions at low temperatures.* International Journal of Hydrogen Energy, Pages 1-8 https://doi.org/10.1016/j.ijhydene.2015.11.122

[5] JE Flores-Chan, A. Torres-Islas, C. Patiño-Carachure, G. Rosas-Trejo & MA Espinosa-Medina (2021) *Comportamiento de corrosión de aleación intermetálica de Al–20Cu en agua de mar sintética,* Canadian Metallurgical Trimestral, 60:3, Pages 1-5, https://doi.org/10.1080/00084433.2021.1997263

[6] Olivares *et al* (2012). *Hydrogen Generation by Treatment of Aluminium Metal with Aqueous Solutions*: Procedures and Uses. In Tech. https://doi.org10.5772/48762

[7] Irankhah, A., Seyed Fattahi, S. M., & Salem, M. (2018). *Hydrogen generation using activated aluminum/water reaction.* International Journal of Hydrogen Energy. Pages 1-6 https://doi.org/10.1016/j.ijhydene.2018.07.014

[8] Wang *et al* (2011). *Generation of hydrogen from aluminum and water – Effect of metal oxide nanocrystals and water quality.* International Journal of Hydrogen Energy, Pages 1-8. https://doi.org/10.1016/j.ijhydene.2011.08.077

[9] M. Araghchi, H. Mansouri & R. Vafaei (2017). *Influencia del tratamiento térmico criogénico en las propiedades mecánicas de una aleación de Al–Cu–Mg*, Ciencia y tecnología de materiales. Pages 1-5, https://doi.org/10.1080/02670836.2017.1407553

[10] ASTM. *"Standard Guide for Preparation of Metallographic Specimens".* ASTM E3-11. 2da Edition. Pennsylvania: Ed. ASTM International, 2015. https://www.academia.edu/35989703/ASTM_E_3_01_Standard_Guide_for_Preparation_of_Metallographic_Specimens_1?auto=download&email_work_card=download-paper

[11] Standard, A.S.T.M, D. (1998). 1141-98: *"Standard Practice for the Preparation of Substitute Ocean Water".* American Society for Testing and Materials, USA. https://tienda.aenor.com/norma-astm-d1141-98e1-003143

[12] ASTM, Designation: G5-94, *"Standard Reference Test Method for Making Potentiostatic and Potentiodynamic Anodic Polarization Measurements",* 1993. https://www.astm.org/g0005-94r11e01.html

[13] ASTM, Designation G59-91, *"Standard practice for conducting Potentiodynamic Polarization Resistance Measurements"* 2004. https://pdfcoffee.com/astm-g59-pdf-free.html

[14] Holroyd, N.J.H., Scamans, G.M. (2013) *Stress Corrosion Cracking in Al-Zn-Mg-Cu Aluminum Alloys in Saline Environments.* Metall Mater Trans A 44, Pages 1-8 https://doi.org/10.1007/s11661-012-1528-3

[15] George F. V. V. *Metallography and Microstructures*, Volume 9. ASM International. 2004. USA.

[16] KUMAR, S., NAMBOODHIRI, T.K.G. (2016). *Precipitation hardening and hydrogen embrittlement of aluminum alloy AA7020*. Bull Mater Sci 34, Pages 2-5.https://doi.org/10.1007/s12034-011-0066-8

[17] Yang, Y.-K., & Allen, T. (2013). *Direct visualization of β phase causing intergranular forms of corrosion in Al–Mg alloys*. Materials Characterization, 80, Pages 1-4. https://doi.org/10.1016/j.matchar.2013.03.014

[18] Hamana, D., Baziz, L., & Bouchear, M. (2004). *Kinetics and mechanism of formation and transformation of metastable β'-phase in Al–Mg alloys*. Materials Chemistry and Physics, 84(1), Pages 1-6, https://doi.org10.1016/j.matchemphys.2003.11.001

[19] T.B Massalki, H Okamoto, P.R. Subramanian, L. Kacprzak, W.W. Scott, *Binary Alloy Phase Diagrams, ASMT International*, Vol 1, (1986), Metals Park, OH: American society for metals.

[20] Grimm *et al* (2019), *Influence of the microstructure on the corrosion behaviour of cast Mg-Al alloys*, Corrosion Science, Volume 155, Pages 1-3, ISSN 0010-938X, https://doi.org/10.1016/j.corsci.2019.04.024

[21] Liu *et al* (2017). *Pitting Corrosion of Steel Induced by Al_2O_3 Inclusions*. Metals, 7(9), Pages 1-8 https://doi.org/10.3390/met7090347

[22] Mendoza Márquez, O.J. (2020) *Evaluación del Mecanismo de Corrosión del Aluminio y sus Aleaciones Al-5154 y Al-6063 para la producción de Hidrógeno*. [Tesis de Maestría]. Universidad Autónoma del Carmen.

[23] Zhang *et al* (2020). *Influence of heat treatment on corrosion behavior of rare earth element Sc modified Al-Mg alloy processed by selective laser melting*. Applied Surface Science, https://doi.org/10.1016/j.apsusc.2020.145330

[24] Flores Chan J.E. (2018). *Evaluación de la corrosión en intermetálicos Al-Me20% peso (Me=Fe, Cu y Mg) en agua de mar sintética, empleando técnicas electroquímicas CP, RPL y EIE* [Disertación Doctoral, Universidad Michoacana de San Nicolas de Hidalgo]. Repositorio de la UMSNH. http://bibliotecavirtual.dgb.umich.mx:8083/xmlui/handle/DGB_UMICH/1321

[25] Zhang *et al* (2020*). Current-driving intergranular corrosion performance regeneration below the precipitate's solvus temperature in Al–Mg alloy*. Journal of Materials Science & Technology, 53, Pages 1-5. https://doi.org/10.1016/j.jmst.2020.01.071

[26] Yi *et al* (2017). *Characterization of Al-Mg Alloy Aged at Low Temperatures*. Metallurgical and Materials Transactions A, 48(4), Pages 1-9. https://DOI.org10.1007/s11661-017-3992-2

Chapter 8 Phytoremediation of heavy metals in petroleum-contaminated soil using red mangrove (*Rhizophora mangle*) and a microbial consortium

Capítulo 8 Fitorremediación de metales pesados presentes en suelo contaminado con petróleo crudo utilizando mangle rojo (*Rhizophora mangle*) y un consorcio microbiano

RAMÍREZ-ELÍAS, Miguel Ángel†*, BENÍTEZ-PINEDA, Paulo Alberto, AGUILAR-UCÁN, Claudia Alejandra and CÓRDOVA-QUIROZ, Atl Víctor

Universidad Autónoma del Carmen, Facultad de Química. Calle 56 No. 4 Esq. Avenida Concordia Col. Benito Juárez C.P. 24180 Cd. del Carmen, Campeche, México

ID 1st Author: *Miguel Ángel, Ramirez-Elias* / **ORC ID**: 0000-0002-3962-1117, **CVU CONAHCYT ID**: 226557

ID 1st Co-author: *Paulo Alberto, Benítez-Pineda* / **ORC ID**: 0000-0002-4340-318X, **CVU CONAHCYT ID**: 920418

ID 2nd Co-author: *Claudia Alberto, Aguilar-Ucán* / **ORC ID**: 0000-0002-1733-2867, **CVU CONAHCYT ID**: 93717

ID 3rd Co-author: *Atl Víctor. Córdova-Quiroz* / **ORC ID**: 0000-0003-1854-288X, **CVU CONAHCYT ID**: 122022

Abstract

In the present work, was studied the capacity of red mangrove (Rhizophora mangle) seedlings to phytoremediator heavy metals in soils contaminated with crude oil by applying bioaugmentation through a microbial consortium made up of Serratia marcescens, Trichoderma harzianum and Rhizopus sp. Experimental treatments were prepared in triplicate with soils contaminated with 30, 60 and 100 mg/Kg of crude oil and cohorts or surveys of experimental units were carried out 0, 15, 30, 60 and 90 days, respectively. The growth of the Rhizophora mangle seedlings was evaluated, obtaining an average height of 9.69 cm and a root length average of 10.67 cm. To determine the concentration of heavy metals, the EPA 3050B digestion method was used, and for its quantification, a Thermo-Scientific atomic absorption spectrophotometer, model ICE 3000, was used. With the results obtained, the heavy metal phytoremediation percentages were calculated. Finality, the percentages of average phytoremediation of heavy metals by applying Rhizophora mangle and the microbial consortium, presented the following order: Cd (86%) > Pb (65%) > Cu (57%) > Zn (43%) > (40%).

Phytoremediation, Heavy metals, Crude oil, Red mangrove, Bioaugmentation

Resumen

En el presente trabajo, se estudió la capacidad de plántulas de mangle rojo (Rhizophora mangle) para fitorremediar metales pesados en suelos contaminados con petróleo crudo mediante la aplicación de bioaumentación a través de un consorcio microbiano conformado por *Serratia marcescens, Trichoderma harzianum y Rhizopus* sp. Los tratamientos experimentales se prepararon por triplicado con suelos contaminados con 30, 60 y 100 mg/Kg de petróleo crudo y se realizaron cohortes o muestreos de unidades experimentales a 0, 15, 30, 60 y 90 días, respectivamente. Se evaluó el crecimiento de las plántulas de Rhizophora mangle, obteniendo una altura promedio de 9.69 cm y una longitud de raíz promedio de 10.67 cm. Para determinar la concentración de metales pesados se utilizó el método de digestión EPA 3050B, y para su cuantificación se utilizó un espectrofotómetro de absorción atómica Thermo-Scientific, modelo ICE 3000. Con los resultados obtenidos se calcularon los porcentajes de fitorremediación de metales pesados. Finalmente, los porcentajes de fitorremediación promedio de metales pesados mediante Rhizophora *mangle* y el consorcio microbiano, presentaron el siguiente orden: Cd (86%) > Pb (65%) > Cu (57%) > Zn (43%) > (40 %).

Fitorremediación, Metales pesados, Petróleo crudo, Mangle rojo, Bioaumentación

1. Introduction

Currently, worldwide, energy security in oil-producing countries is still based on petroleum derivatives; therefore, it is necessary to continue research on bioremediation technologies for sites contaminated with crude oil and heavy metals; one of them is phytoremediation. Phytoremediation is an environmentally friendly and efficient technique to reduce the impact of heavy metals contained in crude oil (Barea *et al.*, 2005; Shen *et al.*, 2023; Singh & Pant, 2023; Tehrani & Besalatpour, 2023). This results in a feasible, economical and important method for the reduction of heavy metal contamination in the Gulf of Mexico and in the Laguna de Términos region where the red mangrove (Rhizophora mangle) predominates, which represents an important ecological alternative for phytoremediation of heavy metals present in soils contaminated with crude oil.

Bioremediation and phytoremediation are techniques that use microorganisms, plants, the interaction of plants with microorganisms, and specifically, the interaction of bacteria and fungi individually or in the form of a microbial consortium, which in turn are associated with plants (Saha *et al.*, 2021; Wojtowicz *et al.*, 2023). Bioremediation is an environmentally friendly technology for remediating contaminated soils, the efficacy of which requires further research as proposed in the present study. Other researchers indicate that the combined use of microorganisms or microbial remediation, plants, conditioned natural materials or even the use of nanomaterials was suggested as an effective and innovative method for remediation of soils contaminated with heavy metals (Luo *et al.*, 2017; Zanganeh *et al.*, 2022).

The remediation of sites contaminated with heavy metals, crude oil and other toxic pollutants; has been effective and reliable due to their ecological characteristics given that they use microbial (bioremediation) or plant (phytoremediation) processes (Moreira *et al*., 2013; Al-Solaimani *et al.,* 2022; Nayak, Bhushan & Wilson. 2022; Cheng *et al.,* 2023). Bioremediation can be performed with ex situ or in situ techniques; its application will depend on 1 the characteristics of the site, the type and concentration of contaminant, as well as the treatment costs. Ex situ techniques are more expensive compared to in situ techniques because of the additional cost attributable to excavation. However, the cost of installing equipment on site and the inability to visualize and monitor the subsurface of contaminated sites are major concerns when conducting in situ bioremediation (Singh & Tripathi, 2023; Azubuike, Chikere & Okpokwasili, 2016). On the other hand, two technologies can also be applied to improve bioremediation: biostimulation (addition of nutrients) and bioaugmentation (addition of microorganisms), which are used when successful treatment is required and after previously performing a physical, chemical and microbiological characterization of the site to be bioremediated.

Mangrove forests are very complex ecosystems with multiple ecological functions and high economic value (Olguin *et al*., 2007). Given the ecological importance of the red mangrove as a protective barrier against natural phenomena, nesting and rearing of juvenile marine and coastal species (Lewis 2005), it will be necessary to determine whether the red mangrove (Rhizophora mangle) has the potential to be used as a phytoremediation plant for heavy metals, as well as to determine whether filamentous fungi such as T. harzianum, Rhizopus sp and the bacterium S. marcescens help in the phytoremediation of heavy metals (Lewis *et al*., 2005).

Con el desarrollo del presente trabajo se generará información importante para la fitorremediación de metales pesados presentes en suelos contaminados con petróleo crudo medio, el cual es representativo de la mezcla mexicana que se produce en la Sonda de Campeche, México. Por lo anterior, el objetivo de esta investigación fue fitorremediar metales pesados presentes en suelos contaminados con petróleo crudo medio (22.4 °API) utilizando plantas de mangle rojo (*Rhizophora mangle*) y un consorcio microbiano conformado por *Serratia marcescens*, *Trichoderma harzianum* y *Rhizopus* sp.

This paper contains the abstract, introduction, methodology, results, conclusions, acknowledgments and references. The introduction includes the objective and hypothesis of the work. The hypothesis of the work was the following: "With the application of Rhizophora mangle plants (phytoremediation) and the microbial consortium formed by Trichodema harzianum, Rhizopus sp and Serratia marcescens (bioaugmentation), it is expected to obtain high percentages of phytoremotion of heavy metals present in soils contaminated with medium crude oil". On the other hand, the methodology includes the evaluation of seedling height and root length of red mangrove seedlings; as well as the determination of physicochemical, microbiological and heavy metal parameters in the phytoremediation of soils contaminated with crude oil. The results include seedling height and root length of red mangrove seedlings, pH, electrical conductivity, texture and organic matter of the soil during the phytoremediation trial, in addition to the colony forming units of the microbial consortium and the percentage of phytoremediation of heavy metals in soils contaminated with crude oil.

2. Materiales y métodos

The experiment of phytoremediation of contaminated soil using red mangrove plants was installed in the botanical garden of the Universidad Autónoma del Carmen. The microorganisms that were used as a microbial consortium in the phytoremediation of heavy metals in oil contaminated soils were provided by Dr. Miguel A. Ramírez Elías, professor of the Faculty of Chemistry of the UNACAR. For the trial, a selection of Rhizophora mangle seedlings was made in order to have a homogeneous size. The experimental treatments were prepared by placing one kilogram of previously sterilized soil in crystallizers. To each soil unit, 30, 60 and 100 mg of crude oil were added, respectively, to obtain the respective units contaminated with 30, 60 and 100 ppm (mg/kg). Subsequently, they were placed in a sowing bag and transferred to a greenhouse of the botanical garden of UNACAR. Finally, the red mangrove seedlings previously selected for their size were placed in the sowing bag in triplicate and the prepared microbial consortium was applied to each of the experimental treatments. Likewise, the pH of the soil and sterilized water was adjusted to 6 to provide an optimum pH for the microbial consortium and the red mangrove seedlings used (Moreno, 2000).

2.1. Evaluation of the height and root length of red mangrove (Rhizophora mangle) seedlings

The following characteristics were evaluated in the seedlings: propagule height, root length and number of leaves. All this was done in each cutting or time period, respectively (0, 15, 30, 30, 60 and 90 days). A graduated ruler was used for each of the measurements. The objective was to know the changes of the seedlings with respect to the progress of the phytoremediation trial.

2.2. Determination of physicochemical, microbiological and heavy metal parameters during phytoremediation of crude oil contaminated soil

The soil samples obtained from each cut or time period were deposited in glass crystallizers for drying at 40 °C, in a Fisher Scientific oven. The dried soils were sieved with a mesh < 0.05 mm. From each sieved sample, the amount of soil necessary to determine the physicochemical parameters was taken; as well as the concentration of the following heavy metals: Cd, Cu, Ni, Pb, and Zn.

For the determination of physicochemical parameters such as pH and electrical conductivity (EC), the potentiometer and conductivity meter method was used, in accordance with the NOM-021-SEMARNAT 2000 standard. Organic matter was determined using the Walkey and Black (1999) method described in the official Mexican standard NOM-021-SEMARNAT-2000. Texture was determined using the Bouyoucos technique described in NOM-021-SEMARNAT-2000.

For the determination of microbial activity, 10 g of soil were taken from each experimental unit and added in an Erlenmeyer flask then 90 mL of distilled water was added, shaken until a suspension was formed and using the dilution and raking technique in Petri dishes with potato dextrose agar (PDA) and nutrient agar (AN), respectively; the colony forming unit (CFU) count was performed in each experimental unit of the phytoremediation trial (Aydin *et al.*, 2017).

The determination of the concentration levels of heavy metals (Cd, Cu, Ni, Pb and Zn) was carried out using EPA (Environmental Protection Agency) method 3050B, which refers to the acid digestion of sediments, sludge and soils by Atomic Absorption Spectrophotometry (Lorentzen & Kingston, 1996). A Thermo Scientific Atomic Absorption Spectrophotometer, model iCE 3000 Series, was used. Standard solutions of Cd, Cu, Ni, Pb and Zn and INORGANIC VENTURES certified reference materials were used to determine the concentration of heavy metals. The calibration curve started with a 1000 mg/L solution for the five metals under study. All samples and the blank were prepared with deionized water. Finally, from the calibration curve for each metal, the samples were read and the concentration of heavy metals was determined (Handschuh, 2013).

For the determination of the percentage of heavy metal phytoremoval, the following equation was applied:

$$\% \, Fitorremediación = \frac{[metal \; en \; el \; testigo] - [metal \; en \; la \; muestra]}{[metal \; en \; el \; testigo]} * 100 \tag{1}$$

3. Results

## 3.1. Seedling height and root length of Rhizophora mangle during phytoremediation.

In Figure 3.1, it is observed that the growth and height of the Rhizophora mangle seedlings was sequential and proportional in the three concentrations of oil and in the respective exposure times, presenting an average height of 9.69 cm, a minimum height of 6.50 cm in the 60 ppm concentration and a maximum height of 13.10 cm in the 100 ppm concentration in a period of 90 days. Likewise, the increase in root length in the monitored seedlings had a growth similar to the plant height, as shown in Figure 3.2. The average root length was 10.67 cm, starting with a minimum length of 5.50 cm at 30 ppm and reaching a maximum root length of 16.75 cm at 100 ppm. This confirms the rhizospheric strength of the red mangrove (Rhizophora mangle) and its application in phytoremediation processes of heavy metals present in soils or sediments contaminated with total petroleum hydrocarbons (Moreira *et al.*, 2013).

Graph 3.1 Height of Rhizophora mangle seedlings), (Mean ± Standard Error)
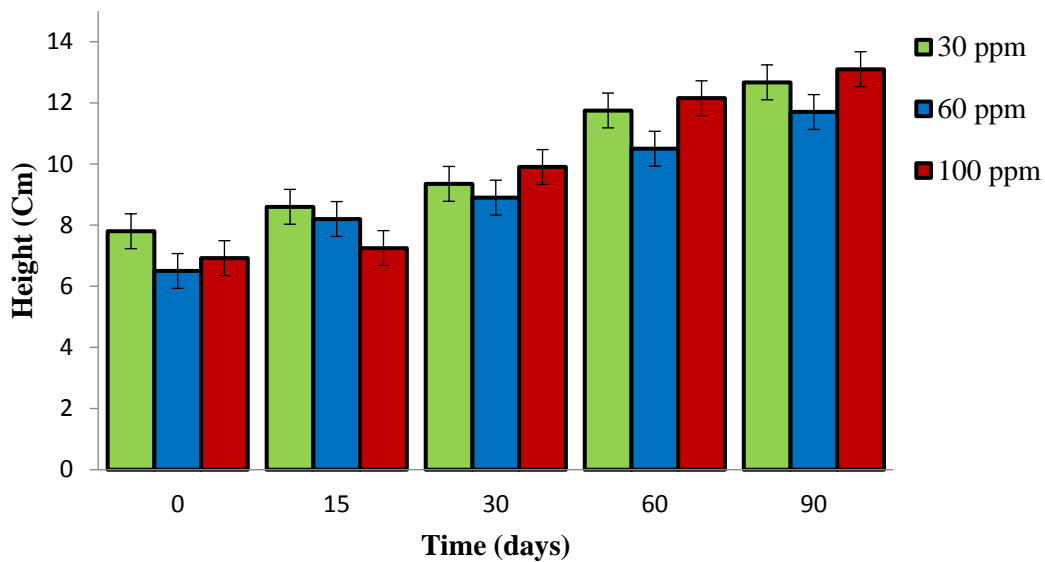
Graph 3.2 Root length of Rhizophora mangle seedlings), (Mean ± Standard Error)
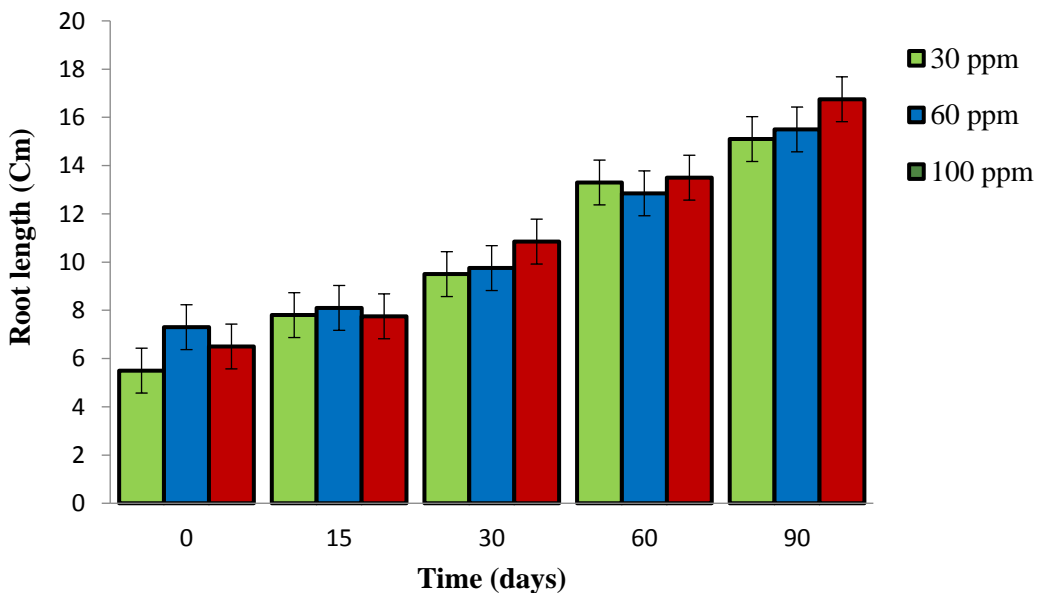
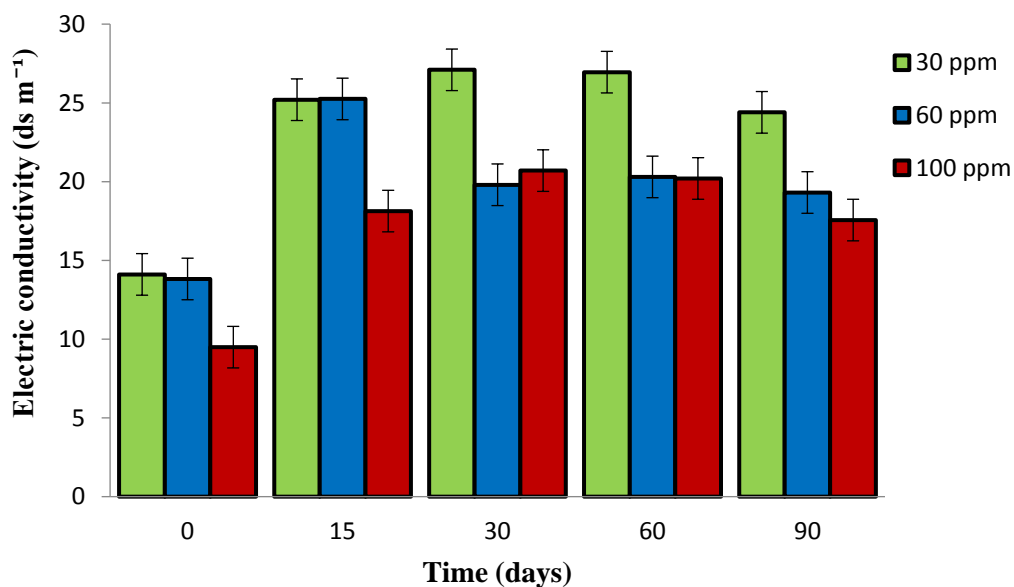## 3.2. Soil pH during phytoremediation

The average pH value was 7.46; the minimum pH value was 7.09 at 90 days at the 100 ppm oil concentration and the maximum pH value was 7.84 at 30 days at the 30 ppm concentration (Graph 3.3.). This shows that the lower the concentration of oil in the soil, the higher the pH value, and at high oil concentrations the pH tends to neutralize. Changes in pH may be associated with the buffering capacity of the soil and active microbial metabolism in the presence of hydrocarbons and nutrients (Atlas and Bartha, 2001).

The average pH of 7.46 obtained in the present heavy metal phytoremediation study was lower compared to the average pH of 7.55 reported by Moreira *et al.* (2013) in a study evaluating the effects of metals on phytoremediation of total petroleum hydrocarbons for 90 days. Therefore, the obtained pH values are representative of mangrove soils and sediments, which favors the activity of microorganisms present in bioremediation and phytoremediation processes.

Graph 3.3 Soil pH (Mean ± Standard Error)
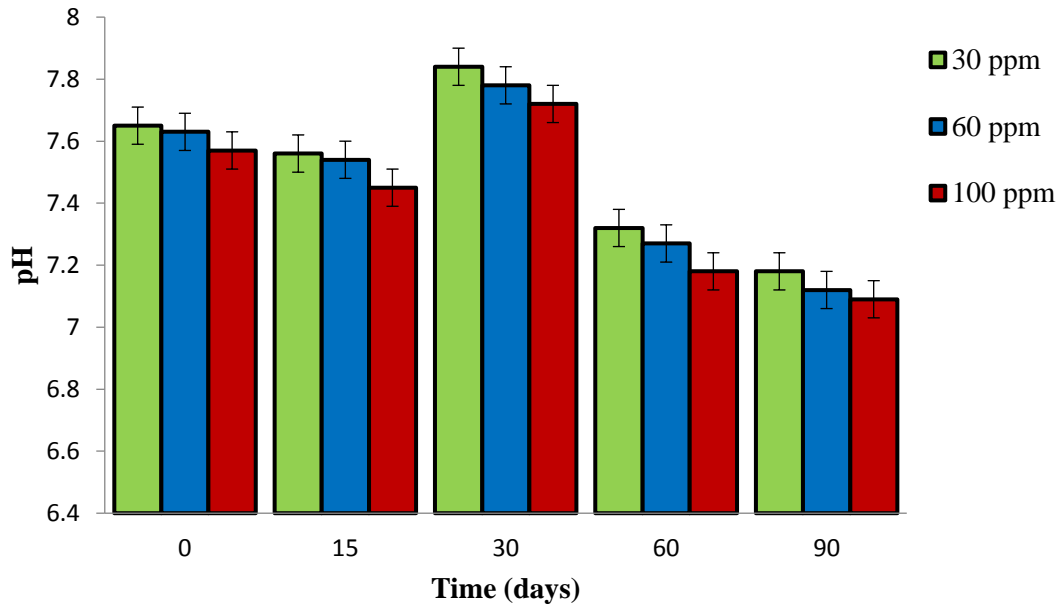
3.3. Soil electrical conductivity during phytoremediation

Graph 3.4 shows the data obtained from the experiment, where it can be observed that at the beginning of the test (0 days) there is the lowest value of electrical conductivity in the soil compared to the other cuts of the test (15, 30, 60 and 90 days); this can be attributed and associated with the initial concentration of oil, because as the phytoremediation test progressed the concentration of crude oil in the soil was reduced, which generated the increase of the EC in the soil after 15 days of the test.

Graph 3.4 Electrical conductivity (EC) of the soil, (Mean ± Standard Error)

3.4. Soil texture during phytoremediation

Soil texture is another important factor that influences the mobility and availability of heavy metals (Castillo *et al.*, 2017). According to the results shown in Graph 3.5, it is observed that the soil texture is sandy at the beginning and end of the phytoremediation trial. The soil texture showed the following average values: sands (87 %), clays (4.57 %) and silts (8.43 %).

Graph 3.5 Texture of the soil used (%)
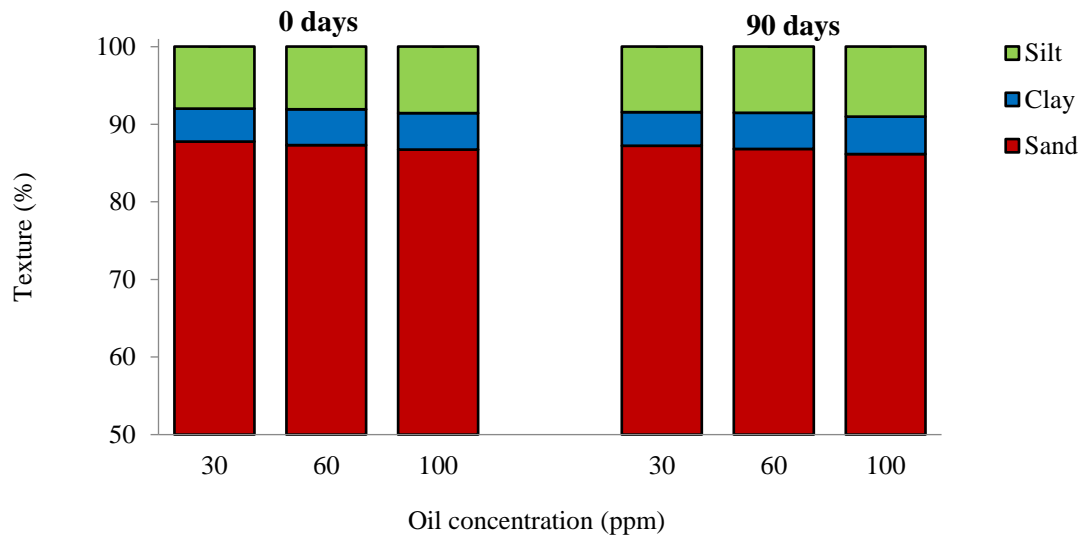
3.5. Soil organic matter during phytoremediation

Figure 3.6 shows the percentages of organic matter (OM) observed during the phytoremediation trial. When comparing the initial cut (0 days) with the final cut (90 days), an increase in organic matter can be observed for each concentration. The average organic matter value was 33%. This percentage is a very high value of OM. However, mangrove soils are very rich in organic matter and this is attributed to the fact that OM acts as a storehouse of metallic elements; in addition to its attraction for heavy metals that are in solution (Pineda, 2004).

Figure 3.6 Percentage of organic matter in soil, (Mean ± Standard Error)
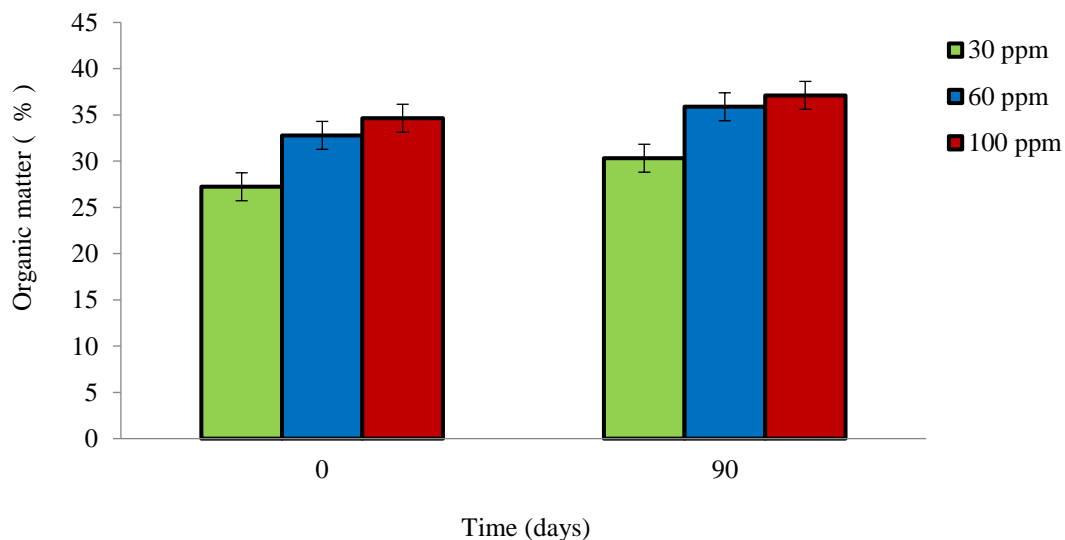
3.6. Microbiological parameters of the microbial consortium during phytoremediation

In order to know the content of colony forming units (CFU), the dilution and raking technique was applied in plates in each period of time and concentration of oil present in the soil. The results of the CFU count obtained from the microbial consortium formed by Trichoderma harzianum, Rhizopus sp and Serratia marcescens are shown below.

Figure 3.7 shows a comparison of the colony forming units of the microbial consortium, as well as the behavior and number of CFU for each concentration (30, 60 and 100 ppm) used in the phytoremediation.

It should be noted that the colony forming units of the fungi are expressed as CFU x 10^3 and for the bacteria as CFU x 10^6; taking this into account, it can be observed that the bacteria (Serratia marcescens) show the highest number of CFU compared to the filamentous fungi (Trichoderma harzianum, Rhizopus sp). Kotoky & Pandey (2020) indicated that the presence of the bacterium Serratia marcescens favors the activity of the enzyme glutathione-S-transferase in mangrove plants, which favors plant growth and reduces stress in the presence of heavy metals. This confirms their behavior in the present study, since the red mangrove plants apparently did not inhibit their height and root length during the heavy metal phytoremediation trial. The CFU obtained in the present study at 30 ppm with Serratia marcescens at 30, 60 and 90 days (60 x 106 CFU g-1, 27 x 106 CFU g-1 and 10 x 106 CFU g-1) were slightly higher than those reported by Moreira *et al*. (2013) in a study evaluating the effects of metals in the phytoremediation of 33 ppm total petroleum hydrocarbons at 30, 60 and 90 days (24.4 x 106 CFU g-1, 32 x 106 CFU g-1 and 7 x 106 CFU g-1).

The microbial consortium had the same behavior and growth trend including the general increase observed at 30 days of the trial, due to the second bioaugmentation of the consortium, with the purpose of guaranteeing the CFU of bacteria and fungi until the end of the trial, given that with the passage of time the consortium tends to decrease its growth due to the reduction of nutrients in the soil.

Gráfico 3.7 Unidades Formadoras de Colonias (UFC) del consorcio microbiano: **A**) 300 ppm, **B**) 60 ppm y **C**) 100 ppm, Las UFC para Hongos (*) se expresan como UFC x 10^3 y para la Bacteria (**) se expresan como UFC x 10^6.
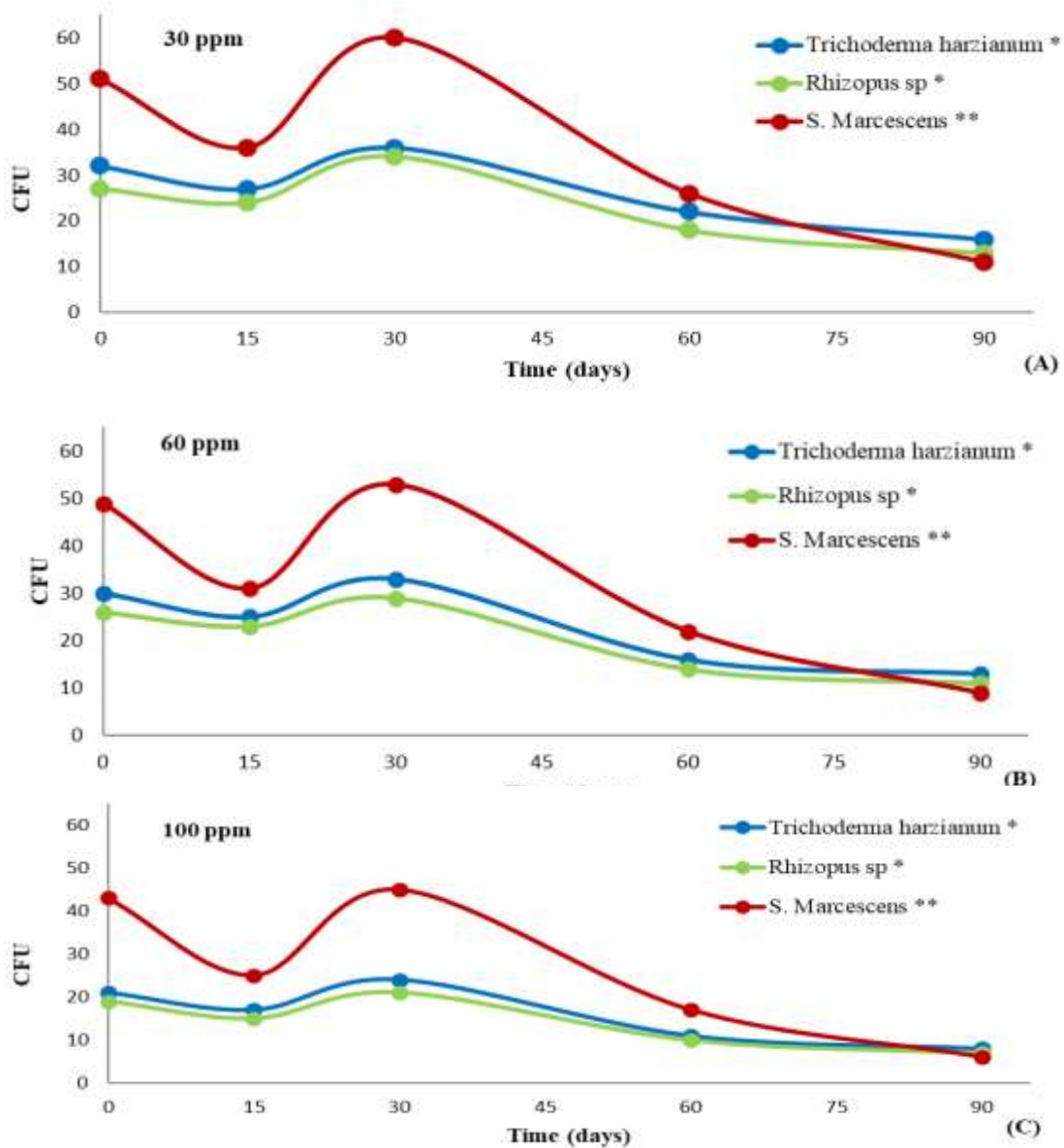
3.7 Percentage of phytoremoval of heavy metals (Cd, Cu, Ni, Pb and Zn) in soils contaminated with crude oil

3.7.1 Cadmio (Cd)

Figure 3.8 shows each of the percentages of cadmium phytoremoval in the respective time periods and concentrations. The percentages varied depending on the concentration; it was observed that the lower the oil concentration, the higher the percentage of cadmium phytoremoval. At the end of the trial (90 days) it can be observed that, at 30 ppm of crude oil, an average of 93 % Cd phytoremoval was obtained, as opposed to the concentration of 60 ppm, where 87 % Cd phytoremoval was obtained and for 100 ppm of oil the Cd phytoremoval was 78 %. Finally, in the present trial the average Cadmium phytoremoval was 86 %.

The 93 % phytoremediation of Cd obtained in the present study at 30 ppm crude oil at 90 days of the trial was higher compared to the 35 % phytoremediation of Cd reported by Moreira *et al.* (2013) in a study evaluating the effects of metals on the phytoremediation of 33 ppm total petroleum hydrocarbons for 90 days. Therefore, the phytoremediation of Cd in this study was approximately 58 % more efficient in the phytoremediation of Cd.
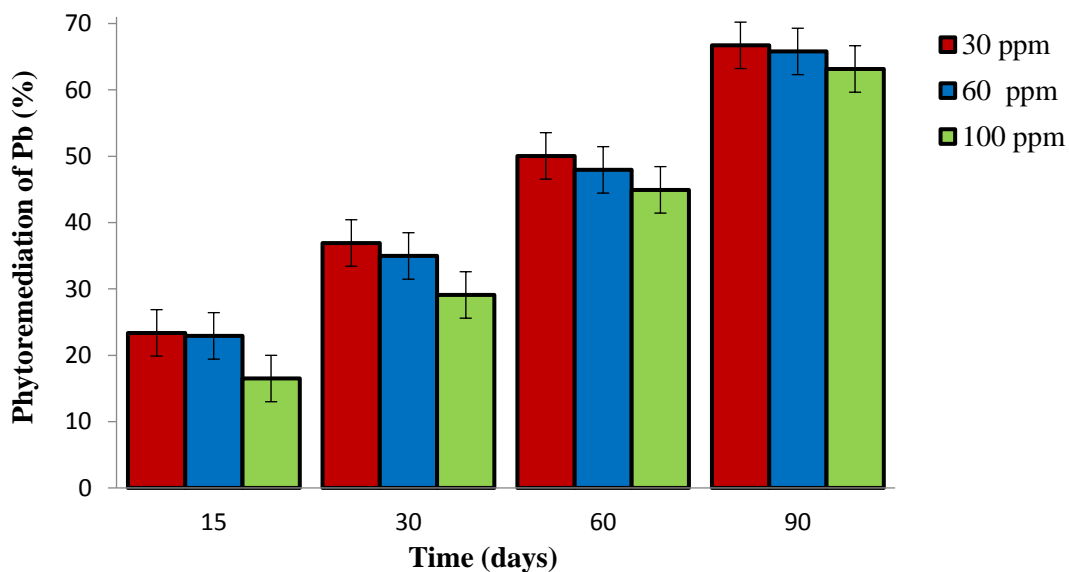
Graph 3.8 Percentage of phytoremediation of Cadmium (Cd), (Mean ± Standard Error), (Mean ± Standard Error)
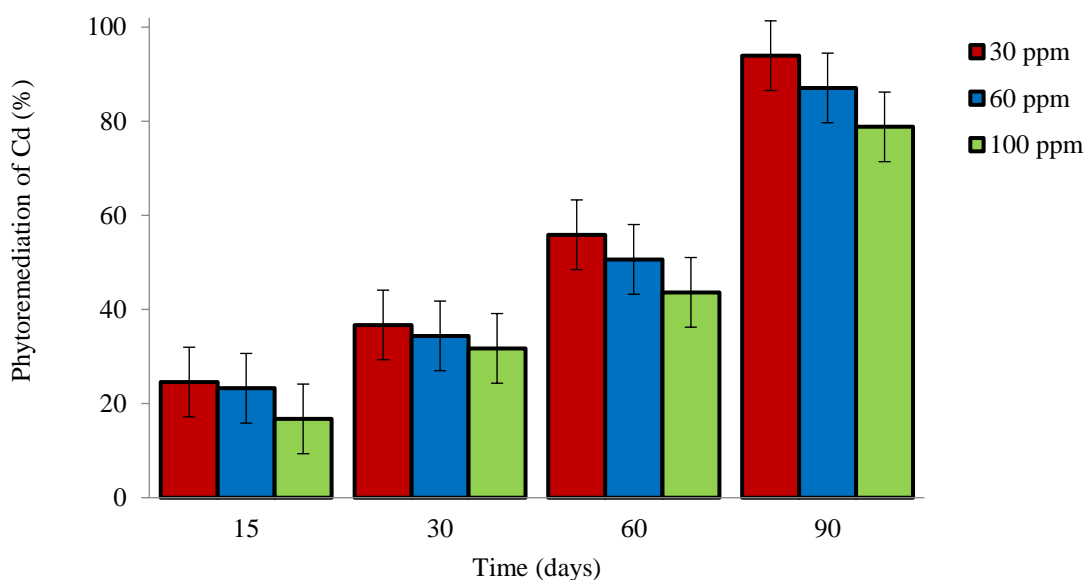
3.7.2 Copper (Cu)

The phytoremoval percentages for copper can be seen in Graph 3.9, in which a constant Cu phytoremoval is observed in each cut or period of time. It can be observed that for 100 ppm of oil, 49 % of Cu phytoremoval was obtained and for the 60 ppm concentration, 59 % of Cu phytoremoval was obtained. Finally, for the 30 ppm concentration, it presented 64% and was the highest phytoremoval value at 90 days. Finally, in the present trial, the average phytoremediation of copper was 57.3 %.

The 64% Cu phytoremediation obtained in the present study at 30 ppm crude oil at 90 days of the trial was higher compared to the 25% Cu phytoremediation reported by Moreira *et al.* (2013) in a study evaluating the effects of metals on the phytoremediation of 33 ppm total petroleum hydrocarbons for 90 days. Therefore, the Cu phytoremediation in this study was approximately 39 % more efficient in the phytoremediation of Cu.

**Graph 3.9** Percentage of Phytoremediation of Copper (Cu), (Mean ± Standard Error))
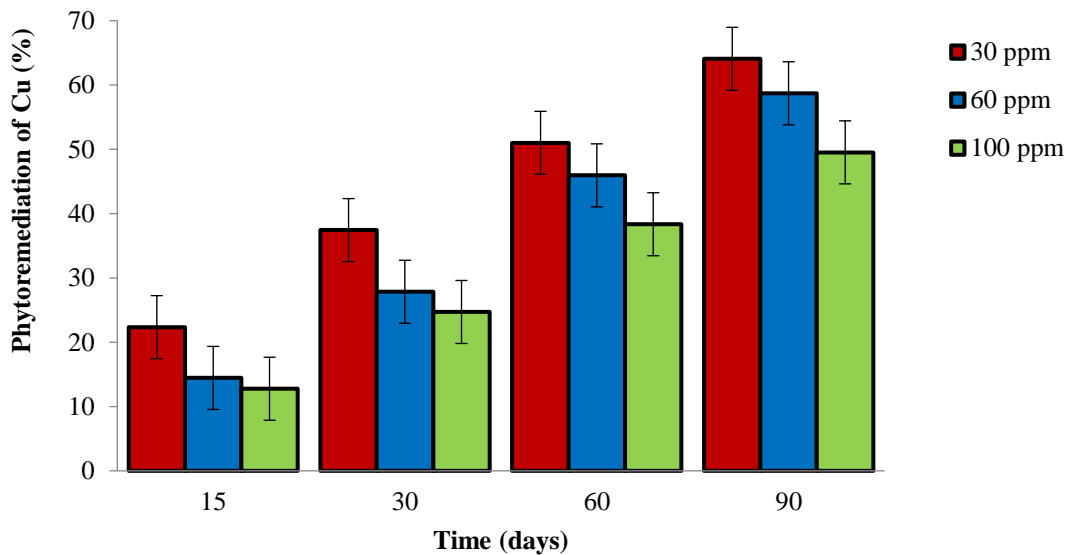
3.7.3 Nickel (Ni)

Figure 3.10 shows the phytoremoval values of Nickel obtained in the experiment. It can be observed that as the exposure time passes, the phytoremotion percentage increases, this is due to the adaptation of the Rhizophora mangle seedlings and the function of the microorganisms showing a constant phytoremotion. The achieved percentages of Ni were as follows: 42 % phytoremotion at 30 ppm, 40 % at 60 ppm and 38% for 100 ppm in the last cut, presenting a variation of 2 % between concentrations. Finally, in the present trial the average phytoremediation rate for Nickel was 40 %.

The 42% phytoremediation of Ni obtained in the present study at 30 ppm crude oil at 90 days of the trial was lower compared to the 57% phytoremediation of Cu reported by Moreira *et al.* (2013) in a study evaluating the effects of metals on the phytoremediation of 33 ppm total petroleum hydrocarbons for 90 days. Therefore, the phytoremediation of Ni in this study was approximately 15 % less efficient in the phytoremediation of Ni.

Graph 3.10 Percentage of Phytoremediation of Nickel (Ni), (Mean ± Standard Error)
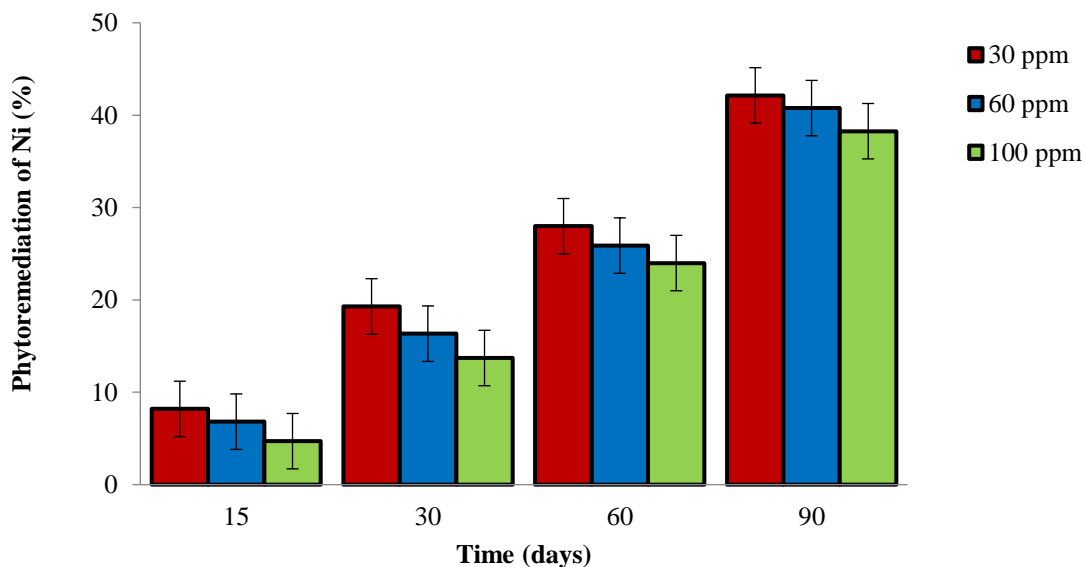
3.7.4 Plomo (Pb)

The phytoremoval percentages for lead were calculated, which are shown in Graph 3.11, obtaining as a result that the three concentrations do not show much difference in the phytoremoval percentages of Pb. The percentages obtained are as follows: for 30 ppm, 66.5 % phytoremoval was obtained, at 60 ppm 65 % and for 100 ppm of oil 63 % of Pb phytoremoval. Finally, in the present trial the average phytoremoval of Lead was 64.8 %.

The 66.5 % phytoremediation of Pb obtained in the present study at 30 ppm crude oil at 90 days of the trial was slightly lower compared to the 66.9 % phytoremediation of Cu reported by Moreira *et al*. (2013) in a study evaluating the effects of metals on the phytoremediation of 33 ppm total petroleum hydrocarbons for 90 days. Therefore, the phytoremediation of Pb in this study was approximately 0.4 % less efficient in the phytoremediation of Pb.

Graph 3.11 Percentage of Phytoremediation of Lead (Pb), (Mean ± Standard Error)

3.7.5 Zinc (Zn)

Finally, Graph 3.12 shows the phytoremediation percentages of Zinc obtained for each cut or time period. The phytoremediation percentages of Zn, as with the metals indicated above, tend to increase with the passage of time, as well as varying according to the concentrations used in the experiment. The 30 ppm and 60 ppm concentrations show a small variation in their percentages, obtaining 46 % and 45 % respectively, in contrast to the 100 ppm crude oil concentration where 38 % of Zn phytoremoval was obtained in a period of 90 days. Finally, in the present trial, the average Zinc phytoremediation rate was 43 %.

The 46 % phytoremediation of Zn obtained in the present study at 30 ppm crude oil at 90 days of the trial was higher compared to the 43 % phytoremediation of Cu reported by Moreira *et al*. (2013) in a study evaluating the effects of metals on the phytoremediation of 33 ppm total petroleum hydrocarbons for 90 days. Therefore, the phytoremediation of Zn in this study was approximately 3 % more efficient in the phytoremediation of Zn.

Graph 3.12 Percentage of Zinc (Zn) Phytoremediation, (Mean ± Standard Error), (%)
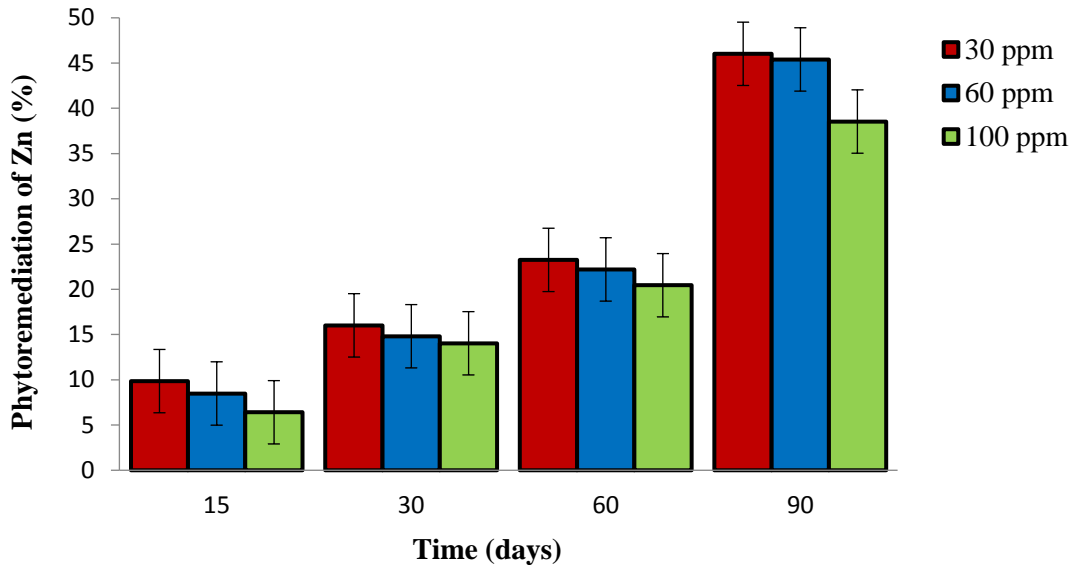
After 90 days, the present phytoremediation trial presented the following order and average phytoremediation percentages of heavy metals: Cd (86 %) > Pb (65 %) > Cu (57 %) > Zn (43 %) > Ni (40 %). Therefore, cadmium was the metal that obtained the highest average phytoremediation percentage of heavy metals present in soils contaminated with medium crude oil, which is in agreement with Pittarello *et al*., (2018) highlighting that cadmium is often found in high concentrations in sediment or mangrove soils.

Finally, the average phytoremoval percentages of heavy metals achieved with red mangrove (Rhizophora mangle) in the present work, presented the following order: Cd > Pb > Cu > Zn > Ni; which, suggests the potential of Rhizophora mangle as a phytoremediation plant for such heavy metals together with the microbial consortium formed by Trichoderma harzianum, Rhizopus sp and Serratia marcescens.

4. Conclusions

High percentages of heavy metal phytoremoval were obtained in soil contaminated with medium crude oil, using Rhizophora mangle seedlings and a microbial consortium composed of Trichoderma harzianum, Rhizopus sp and Serratia marcescens. Therefore, the hypothesis is accepted.

It is also concluded that the presence of the microbial consortium favorably influenced the growth of the red mangrove plants and their function as a phytoremediation plant. Therefore, the red mangrove (Rhizophora mangle) has the potential to be used as a phytoremediation plant for heavy metals together with the microbial consortium formed by T. harzianum, Rhizopus sp and S. marcescens.

5. Acknowledgments

6. References

Al-Solaimani, S. G., Abohassan, R. A., Alamri, D. A., Yang, X., Rinklebe, J., & Shaheen, S. M. (2022). Assessing the risk of toxic metals contamination and phytoremediation potential of mangrove in three coastal sites along the Red Sea. *Marine Pollution Bulletin*, *176*, 113412. https://doi.org/10.1016/j.marpolbul.2022.113412

Atlas, R. y Bartha, R. (2001). Ecología microbiana y ambiental. Quinta edición. California: The Benjamin/Cummings Publishing Company, Inc. pp. 559-610.

Aydin, S., Aygun, H., Shahi, A., Gokce, S., Ince, B., Ince, O. (2016). Aerobic and anaerobic fungal metabolism and omics insight for increasing polycyclic aromatic hydrocarbons biodegradation. *Fungal Biology Reviews.* Pp.61-72. https://doi.org/10.1016/j.fbr.2016.12.001

Azubuike, C. C., Chikere, C. B., & Okpokwasili, G. C. (2016). Bioremediation techniques–classification based on site of application: principles, advantages, limitations and prospects. *World Journal of Microbiology and Biotechnology*, *32*, 1-18. https://doi.org/10.1007/s11274-016-2137-x

Barea, J. M., Pozo, M. J., Azcon, R., & Azcon-Aguilar, C. (2005). Microbial co-operation in the rhizosphere. *Journal of experimental botany*, *56*(417), 1761-1778. https://doi.org/10.1093/jxb/eri197

Castillo, A., Obeso, A., Guerrero, J., Vejarano, D. (2017). Fitorremediación de suelos contaminados con metales pesados mediante cultivo de geranio (*pelargonium zonale).* Investigación y Educación para el desarrollo sostenible, (UPN), Facultad de Ingeniería Ambiental. https://hdl.handle.net/11537/9832

Cheng, P. C., Lin, Y. C., Lin, M. S., Lin, S. L., Hsiao, Y. H., Huang, C. Y., ... & Cheng, S. F. (2023). Phytoremediation Efficiency of Weathered Petroleum-Contaminated Soils by Vetiveria zizanioides and Cymbopogon nardus itle. *Engineering Proceedings*, *38*(1), 63. https://doi.org/10.3390/engproc2023038063

Handschuh, K. (2013). Dinámica Espacio Temporal de Elementos Traza en el Lago Panguipulli, Región de los Ríos, Chile, 2011. Tesis de Pregrado. Universidad Austral de Chile. 138 pp. chrome-extension://efaidnbmnnnibpcajpcglclefindmkaj/http://cybertesis.uach.cl/tesis/uach/2013/fch236d/doc/fch236d.pdf

Kaewtubtin, P., Meeinkuirt, W. Seepom, S. & Pichtel, J. (2018). Phytomanagement of radionuclides and heavy metals in mangrove sediments of Pattani Bay, Thailand using *Avicennia marina* and *Pluchea indica*. *Marine Pollution Bulletin* 127. (2), pp. 320-333. https://doi.org/10.1016/j.marpolbul.2017.12.021

Kotoky, R., & Pandey, P. (2020). Rhizosphere assisted biodegradation of benzo (a) pyrene by cadmium resistant plant-probiotic Serratia marcescens S2I7, and its genomic traits. *Scientific Reports*, *10*(1), 5279. https://doi.org/10.1038/s41598-020-62285-4

Lewis III, R. R. (2005). Ecological engineering for successful management and restoration of mangrove forests. *Ecological engineering*, *24*(4), 403-418. https://doi.org/10.1016/j.ecoleng.2004.10.003

Lorentzen, E. M., & Kingston, H. S. (1996). Comparison of microwave-assisted and conventional leaching using EPA method 3050B. *Analytical Chemistry*, *68*(24), 4316-4320. https://doi.org/10.1021/ac960553l

Luo R, Li J, Zhao Y, Fan X, Zhao P, Chai L. (2017). A critical Review on the research topic system of soil heavy metals Pollution biromediation base don dinamyc co-words network measures. *Geoderma* 305:281-292. https://doi.org/10.1016/j.geoderma.2017.06.019

Moreira, I. T., Oliveira, O. M., Triguis, J. A., Queiroz, A. F., Barbosa, R. M., Anjos, J. A. & Rios, M. C. (2013). Evaluation of the effects of metals on biodegradation of total petroleum hydrocarbons. *Microchemical Journal*, *110*, 215-220. https://doi.org/10.1016/j.microc.2013.03.020

Moreno, Z. (2000). Correlación de la tasa de crecimiento radial y la tasa de crecimiento especifico de hongos filamentosos aislados de la planta Espeletia barclayana. Tesis doctoral. Bogota: pontificia Universidad Javeriana. Facultad de Ciencias. http://hdl.handle.net/10554/56850

Nayak, A., Bhushan, B., & Wilson, I. (2022). Current Soil Bioremediation Technologies: An Assessment. In *Advances in Bioremediation and Phytoremediation for Sustainable Soil Management: Principles, Monitoring and Remediation* (pp. 17-29). Cham: Springer International Publishing. https://doi.org/10.1007/978-3-030-89984-4_2

Norma Oficial Mexicana, NOM 021-SEMARNAT 2000. Que establece las especificaciones de fertilidad, salinidad y clasificación de suelos, estudio, muestreo y análisis; Diario Oficial (2002).

Olguín, E. J., Hernández, M. E., & Sánchez-Galván, G. (2007). Contaminación de manglares por hidrocarburos y estrategias de biorremediación, fitorremediación y restauración. *Revista internacional de contaminación ambiental*, *23*(3), 139-154. chrome-extension://efaidnbmnnnibpcajpcglclefindmkaj/https://www.scielo.org.mx/pdf/rica/v23n3/v23n3a4.pdf

Pineda, R. (2004). Presencia de hongos micorrizicos arbusculares y contribución de *Glummu*s en la absorción y translocación de cinc y cobre en girasol (*Helianthus annuus L.*) crecido en un suelo contaminado con residuos. Universidad de colima, área: Biotecnología

Pittarello, M., Busato, J. G., Carletti, P., Zanetti, L. V., da Silva, J., & Dobbss, L. B. (2018). Effects of different humic substances concentrations on root anatomy and Cd accumulation in seedlings of Avicennia germinans (black mangrove). *Marine pollution bulletin*, *130*, 113-122. https://doi.org/10.1016/j.marpolbul.2018.03.005

Saha, L., Tiwari, J., Bauddh, K., & Ma, Y. (2021). Recent developments in microbe–plant-based bioremediation for tackling heavy metal-polluted soils. *Frontiers in Microbiology*, *12*, 731-723. https://doi.org/10.3389/fmicb.2021.731723

Shen, Y., Ji, Y., Wang, W., Gao, T., Li, H., & Xiao, M. (2023). Temporal effect of phytoremediation on the bacterial community in petroleum-contaminated soil. *Human and Ecological Risk Assessment: An International Journal*, *29*(2), 427-448. https://doi.org/10.1080/10807039.2022.2102460

Singh, A., & Tripathi, A. K. (2023). Remediation of Heavy Metals: Tools and Techniques. *Biotechnology in Environmental Remediation*, 47-67. https://doi.org/10.1002/9783527839063.ch4

Singh, H., & Pant, G. (2023). Phytoremediation: Low input-based ecological approach for sustainable environment. *Applied Water Science*, *13*(3), 85. https://doi.org/10.1007/s13201-023-01898-2

Tehrani, M. R. F., & Besalatpour, A. A. (2023). A combined landfarming-phytoremediation method to enhance remediation of mixed persistent contaminants. https://doi.org/10.21203/rs.3.rs-3077559/v1

Wojtowicz, K., Steliga, T., Kapusta, P., & Brzeszcz, J. (2023). Oil-Contaminated Soil Remediation with Biodegradation by Autochthonous Microorganisms and Phytoremediation by Maize (Zea mays). *Molecules*, *28*(16), 6104. https://doi.org/10.3390/molecules28166104

Zanganeh, F., Heidari, A., Sepehr, A., & Rohani, A. (2022). Bioaugmentation and bioaugmentation–assisted phytoremediation of heavy metal contaminated soil by a synergistic effect of cyanobacteria inoculation, biochar, and purslane (Portulaca oleracea L.). *Environmental Science and Pollution Research*, *29*(4), 6040-6059. https://doi.org/10.1007/s11356-021-16061-0

Chapter 9 Test of electrodes based on manganese oxide with and without potassium cations for supercapacitors

Capítulo 9 Prueba de electrodos a base de óxidos de manganeso con y sin cationes de potasio para supercapacitores

CHÁVEZ-GÓMEZ, Karina del Carmen, LÓPEZ-LÓPEZ, Elizabeth and QUIROGA-GONZALEZ, Enrique*

Benemérita Universidad Autónoma de Puebla, Instituto de Física

ID 1st Author: *Karina Del Carmen, Chávez-Gómez* / **ORC ID**: 0000-0003-2887-5864, **CVU CONAHCYT ID**: 629494

ID 1st Co-author: *Elizabeth, López-López* / **ORC ID**: 0009-0000-4984-6427

ID 2nd Co-author: *Enrique, Quiroga-Gonzalez* / **ORC ID** 0000-0003-1650-0862, **CVU CONAHCYT ID**: 48276

K. Chávez, E. López, E. Quiroga

*equiroga@ifuap.buap.mx.

Abstract

The demand for more efficient energy storage devices with a sustainable approach has turned supercapacitors into a great alternative in applications where high instantaneous power is required. Above all, those based on manganese oxides are attracting attention for their low cost, durability, and relatively high specific capacitance. However, it is known that MnO_2 with a pyrolusite structure (β-MnO_2) has a poor performance. This work studies this material electrochemically before and after thermally incorporating potassium cations at 800 °C. For the present work, commercial MnO_2 and MnO_2 doped with potassium ions (K-MnO_2) were used as active material for the electrodes of commercial supercapacitors. It was verified that the commercial material is β-MnO_2 and that the thermally doped material is predominantly manganese oxide with a cryptomelane structure (α-K_xMnO_2). Cyclic voltammetry measurements were performed at different scanning rates, to elucidate the electrochemical response of the materials. The results corresponding to K-MnO_2 present a higher current compared to commercial MnO_2, this implies that this electrode has a higher specific capacitance, which can be attributed to a greater potassium ion insertion/extraction capacity. However, at high scanning speeds, its behavior shows that it is pseudocapacitive.

Supercapacitors, Manganese oxide, Capacitance, Electrochemical tests

Resumen

La demanda de dispositivos de almacenamiento de energía más eficientes y con enfoque sustentable, ha convertido a los supercapacitores en una gran alternativa en aplicaciones donde se requiere alta potencia instantánea. Sobre todo, están llamando la atención por su bajo costo, durabilidad y relativamente alta capacitancia específica los basados en óxidos de manganeso. Sin embargo, es conocido que el MnO_2 con estructura pirolusita (β-MnO_2) presenta un pobre rendimiento. En este trabajo se estudia electroquímicamente al MnO_2 antes y después de incorporarle cationes de potasio térmicamente a 800 °C. Para el presente trabajo se empleó como material activo de electrodos de supercapacitores MnO_2 comercial y MnO_2 dopado con iones potasio (K-MnO_2) de manera térmica. Se comprobó que el material comercial es β-MnO_2 y que el material dopado térmicamente es predominantemente óxido de manganeso con estructura criptomelano (α-K_xMnO_2). Se realizaron mediciones de voltamperometría cíclica a diferentes velocidades de barrido, para dilucidar la respuesta electroquímica de los materiales. Los resultados correspondientes al K-MnO_2 presentan una corriente mayor respecto a las del MnO_2 comercial, esto implica que este electrodo tiene una capacitancia especifica superior, la cual puede atribuirse a una mayor capacidad de inserción/extracción de iones potasio. Sin embargo, a velocidades altas de barrido, su comportamiento denota ser pseudocapacitivo.

Supercapacitores, Óxido de manganeso, Capacitancia, Pruebas electroquímicas

1. Introduction

The constant development of electrical devices has led to an increasing demand for energy, and as a consequence an advance in energy storage devices (Paramati *et al*., 2022). Energy is an essential factor for development and progress, so its supply and storage is of vital importance, especially in the process of decarbonization of the global economy, which is gradually taking place (Spinelli *et al*., 2022). At present, the development of efficient, stable systems capable of providing energy storage with high power represents a major challenge. Supercapacitors stand out from other devices, due to high instantaneous power (they can supply large currents in a short time) and large number of charge/discharge cycles (Gonzalez *et al*., 2016).

Given the characteristics already mentioned above, electrochemical capacitors are commonly used in short-term applications requiring high power (Khan *et al.,* 2023). Supercapacitors are increasingly being used for industrial applications as they compaginate with green energy (Mensah-Darkwa *et al*., 2019). As they have the property of storing energy quickly.

The performance of supercapacitors can be evaluated in terms of electrochemical properties, which depend on the properties of the electrodes and the electrolyte (Vangari *et al.*, 2013). Various materials that can rapidly accumulate charge, which is the main characteristic of supercapacitors, have been tested. Initially, ruthenium dioxide (RuO2) was used as the electrode, obtaining a drastic decrease in the internal resistance that characterized the first supercapacitors, making them much more cost-effective and allowing their use as energy storage media in the field of automation (Zhang *et al.*, 2021), RuO2 presents good specific capacitance properties; however, being a costly material with negative effects on the environment, alternatives have been sought in other metal oxides or combinations based on carbon and oxides, among which manganese dioxide (MnO2) stands out; above all, they are attracting attention for their low cost, durability and relatively high specific capacitance (Kour *et al.*, 2022).

Despite the good performance of MnO2 as a charge store in a supercapacitor, few of its phases exhibit this performance (Sari *et al.*, 2017). In particular, the performance of the pyrolusite phase is very poor, around 9- 11F/g (Devaraj *et al.*, 2008; Pundir *et al.*, 2023). On the other hand, the birnesite phase, with specific capacitance of 230 F/g is among the best (Komaba *et al.*, 2008; Zhu *et al.*, 2020). This may be due to the fact that the structure of the latter phase contains mobile cations, and that the interatomic spacing allows it. In this work we intend to electrochemically study MnO2 with pyrolusite structure before and after incorporating potassium cations thermally at 800 °C, to elucidate the effect of cation incorporation and structural change on the electrochemical performance.

2. Methodology

Commercial MnO2 powders (Sigma-Aldrich) and MnO2 doped with potassium ions (K-MnO2) were used for the present study.

2.1. Synthesis of K- MnO2

Commercial MnO2 powders (Sigma-Aldrich) and potassium hydroxide (KOH) flakes, both in a 1:1 molar ratio, were used. The KOH flakes were first crushed in a crucible and then the MnO2 powders were added. Heat treatment was carried out at 800 °C for 2 h at temperature and allowed to cool to room temperature. The powders obtained were washed with deionized water until a neutral pH was obtained, and then they could be used in the fabrication of the electrodes.

2.2. Characterization techniques

To identify the phase of the manganese oxides, the X-ray diffractometry (XRD) technique was used, using the Panalytical - Empyrean diffractometer. As part of the chemical analysis, a Raman microscope of the Horiba LabRAM brand was used, with a He-Ne laser (632.8 nm).

2.3. Electrode fabrication

The electrodes for the supercapacitors in the study were developed from a mixture of three components: manganese oxide (MnO2 and K-MnO2), carbon black (CB) and polyvinylidene fluoride (PVDF). The weight ratio of the above materials was 70:20:10. The paste obtained was deposited on a T-316 stainless steel mesh (food grade) of 100 wires/inch wire gauge 49 (0.03mm) and mesh opening 0.033mm, which was used as a current collector substrate.

2.4. Electrochemical characterization

The cyclic voltammetry tests were performed in a Zahner Zennium potentiostat, using the software of the same Thales equipment for the analysis and acquisition of data, in a 3-electrode cell. The working electrode (WE) which is the paste electrode with the metal oxide to be studied (MnO2), a reference electrode (RE) of Ag/AgCl and the third one that closes the electrical circuit, called counter electrode (CE) of platinum, and 6 M potassium hydroxide (KOH) will be used as electrolyte. Measurements were performed in an operating window from -500 to 750 mV, using sweep speeds of 200, 100, 50, 50, 20, 10, 10, 5, 4, 3 and 2 mV/s.

3. Results

The results obtained from the characterization and discussion of the manganese oxides, the commercial one which is the base material and the resulting oxide after cation insertion are shown below. In addition, the results of the electrochemical test assembled as an electrode in a supercapacitor are presented.

3.1. XRD analysis of the manganese oxides

The structural characterization of the material was carried out by X-ray diffraction. Graph 3.1 shows the diffractograms corresponding to commercial MnO2 and MnO2 with thermal treatment and ion insertion. In graph 3.1a the diffraction peaks correspond to those characteristic of pyrolusite, planes (110), (101), (200), (111), (200), (111), (210), (211), (220), (002), (310) and (301) can be identified, they can be indexed to the tetragonal β-MnO2 phase (JCPDS card N° 24-0735). No peaks for other phases are observed, indicating high purity and crystallinity in the sample. On the other hand, the diffractogram of graph 3.1b, presents diffraction peaks of 2 phases, one of them is of the β-MnO2 as it is the precursor material still present after the thermal treatment and the second resulting phase coincides with the tetragonal phase of the cryptomelane □-KxMnO2 (JCPDS card N° 29-1020), identifying the planes (110), (200), (220), (310), (211), (520) and (431). Comparing the intensity of the highest reflections of the two phases present, qualitatively it is possible to say that this sample is predominantly □-KxMnO2.

Figure 3.1 XRD patterns corresponding to a) commercial MnO2 and b) K-MnO2
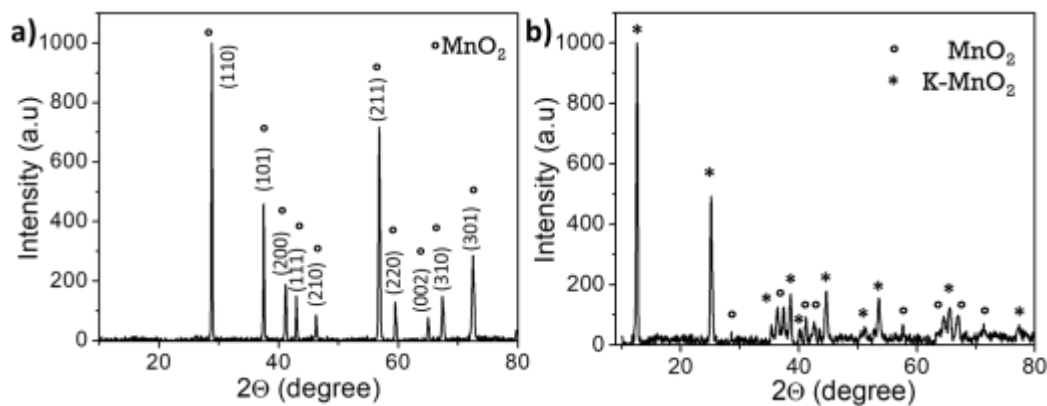
3.2. Characterization by Raman spectroscopy

The samples were analyzed by Raman spectroscopy, graph 3.2a corresponds to the commercial MnO2, it can be observed the well-defined characteristic bands at 557 cm-1 and 668 cm-1 of the β-MnO2 phase. Graph 3.2b, belonging to the K-MnO2 sample, shows the β-MnO2 bands, in addition to the bands positioned at 185, 376 and 576 cm-1 corresponding to □-KxMnO2. In addition, of the synthesized phases that agree with the XRD results, bands appear at positions 157, 284 and 411 cm-1 that can be indexed to the corresponding Mn-OOH phase.

**Figure 3.2** Raman spectra for a) commercial MnO2 and b) K-MnO2
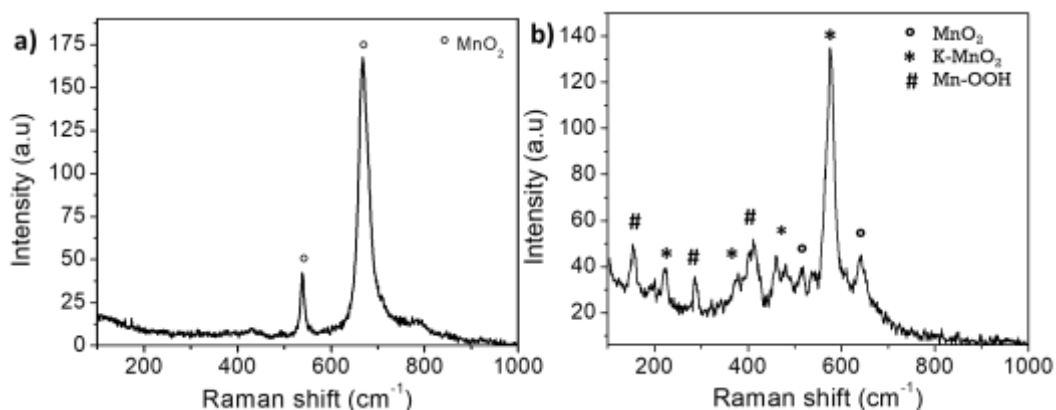
3.3 Caracterización electroquímica de los electrodos fabricados

Based on the characterization results, the β-MnO2 was analyzed for the commercial manganese oxide and a mixture of α and β phases for the oxide with potassium ion insertion. Voltammetry tests were performed on them in a KOH electrolyte.

To understand the electrochemical behavior of the manganese oxides, they were tested as electrodes in supercapacitor in an aqueous medium, at different rates both fast and slow to observe at which rate the electrode obtains higher current density. Figure 3.3 shows the cyclic voltammetry curves for commercial MnO2 at different sweep speeds. A pair of approximately symmetrical redox peaks can be observed in the CV curve at voltages 0.25 and 0.35 V, due to the intercalation/de-intercalation of protons or alkali metal ions on the MnO2 electrode, confirming the pseudocapacitive characteristics. As the scan rate increases, the current intensity increases, while the position (x-axis) of the redox peak shifts only slightly, indicating a good electrochemical reversibility of the system, it is also observed in graph 3.3b that at low speeds the commercial MnO2 loses the characteristic shape of its voltammogram and the oxidation and reduction peaks are not well defined.

Figure 3.3 Cyclic voltammetry plots at a) fast scanning speeds and b) slow speeds of commercial MnO2
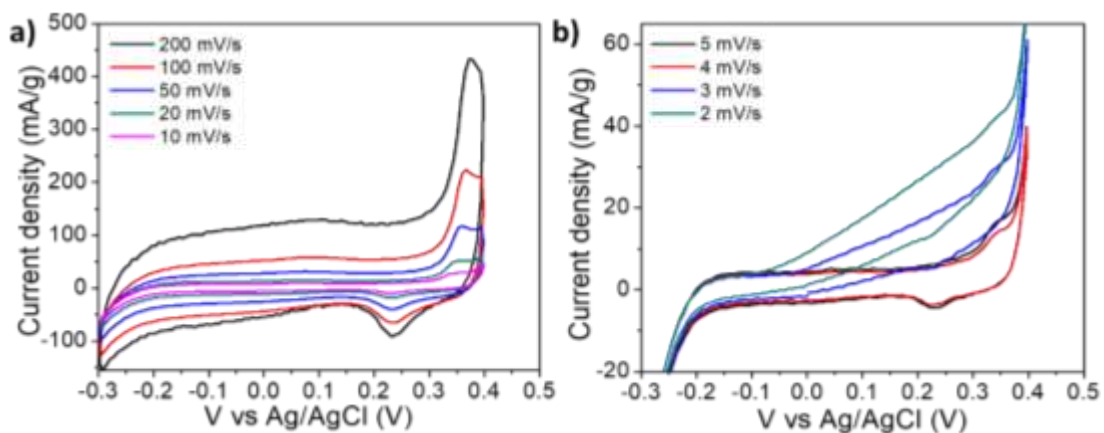
Cyclic voltammetry was performed to know the electrocatalytic activity of K-MnO2 in 6 M KOH as electrolyte. Graph 3.4 shows the voltammograms obtained at different sweep speeds from 200 mV/s to 2 mV/s. The behavior of the cell with KOH electrolyte, a redox process is present with an oxidation peak at -0.04 V and a reduction peak at -0.24 V, but only at low sweep speeds. In addition, comparing the current values of K-MnO2 with respect to those in graph 3.3, a considerable increase is observed, thus proving that the insertion of K ions in the composite acts favorably to increase the current density in the electrode.

Figure 3.4 Cyclic voltammetry plots at a) fast scanning speeds and b) slow K-MnO2 speeds
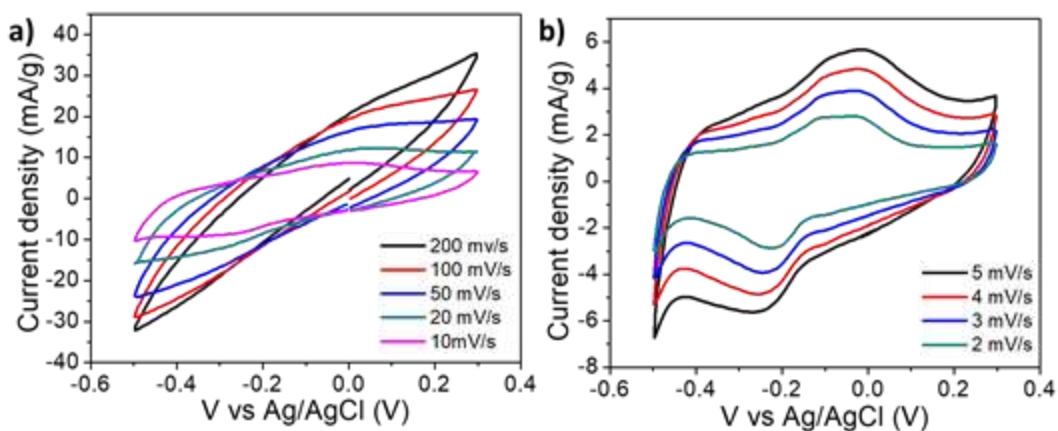
Graph 3.5 shows the specific capacitance of the MnO2 and K-MnO2 electrode as a function of the sweep speed at 2 different potentials 0 and 0. 2 V, the specific capacitances of the electrodes composed of MnO2 were calculated from cyclic voltammetry data at different speeds, the capacitance values were measured at potentials where a faradaic process is observed and another in a capacitive part, also shows the behavior of the capacitance at different sweep speeds, noting that the higher the sweep speed the specific capacitance decreases, this is due to insufficient time for the ions to diffuse into the electrode material (Thomas *et al.*, 2023). In contrast, better storage capacitance is favorable at lower scan rates because slow ionic propagation in the electrolyte-electrode can improve its chemical reactivity. One can compare the capacitance we obtain from MnO2 and K-MnO2, at a rate of 2 mV/s for MnO2 it is 20 F/g, while for K-MnO2 at the same rate it is 350 F/g (17 times higher). This is attributed to the incorporation of K+ cations into the MnO2 structure by heat treatment, which enhances the ion insertion/extraction capacity of the material. At fast rates the capacitance tends to stabilize at one value, indicating pseudocapacitive behavior (Jones *et al.*, 2023). It has been shown that the addition of ions makes the charge storage mechanisms more surface redox dominated and can improve the specific capacitance (Barclay *et al.*, 2023).

Graph 3.5 Comparative graph of the specific capacitances vs. sweep speeds of a) β-MnO2 and b) K-MnO2
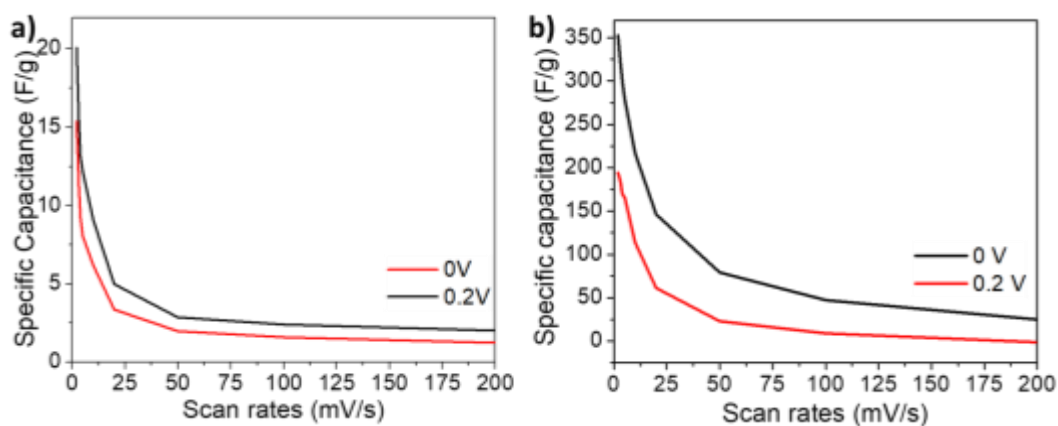
4. Conclusions

From the voltammetry curves it can be seen that the K-MnO2 graphs present a higher current density with respect to that of commercial MnO2. The incorporation of ions in the structure of the material with the thermal treatment, allows the insertion and extraction of ions in an electrochemical way when using it as an electrode of supercapacitors. When analyzing the specific capacitance graphs, it is observed that at fast speeds the capacitance decreases exponentially, but tends to stabilize at fast speeds. This is an indication that at slow speeds the storage process is diffusion limited, and at fast speeds it is pseudocapacitive. Although the K-MnO2 material is not a pure phase, and the potassium phase is cryptomelane (a phase with low cation content), its response as an electrochemical energy store is vastly superior (17 times higher gravimetric capacitance) to commercial MnO2 with pyrolusite structure.

References

Barclay, M., et al. (2023). Plasma-activated water for improved intercalation and pseudocapacitance of MnO2 supercapacitor electrodes. *Materials Today Sustainability, 22*, 100388. doi:https://doi.org/10.1016/j.mtsust.2023.100388

Devaraj, S., & Munichandraiah, N. (2008). Effect of Crystallographic Structure of MnO2 on Its Electrochemical Capacitance Properties. *The Journal of Physical Chemistry C, 112*(11), 4406-4417. doi:https://doi.org/10.1021/jp7108785

González, A., et al. (2016). Review on supercapacitors: Technologies and materials. *Renewable and Sustainable Energy Reviews, 58*, 1189-1206. doi: https://doi.org/10.1016/j.rser.2015.12.249

Jones, D. R., et al. (2023). Scalable Synthesis of Pre-Intercalated Manganese(III/IV) Oxide Nanostructures for Supercapacitor Electrodes: Electrochemical Comparison of Birnessite and Cryptomelane Products. *ChemElectroChem, 10*(14), e202300210. doi:https://doi.org/10.1002/celc.202300210

Khan, M. S., et al. (2023). Unveiling the electrochemical advantages of a scalable and novel aniline-derived polybenzoxazole-reduced graphene oxide composite decorated with manganese oxide nanoparticles for supercapacitor applications. *Journal of Energy Storage, 73*, 109109. doi:https://doi.org/10.1016/j.est.2023.109109

Komaba, S., Ogata, A., & Tsuchikawa, T. (2008). Enhanced supercapacitive behaviors of birnessite. *Electrochemistry Communications, 10*(10), 1435-1437. doi:https://doi.org/10.1016/j.elecom.2008.07.025

Kour, S., Tanwar, S., & Sharma, A. (2022). A review on challenges to remedies of MnO2 based transition-metal oxide, hydroxide, and layered double hydroxide composites for supercapacitor applications. *Materials Today Communications*, 104033. doi:https://doi.org/10.1016/j.mtcomm.2022.104033

Mensah-Darkwa, K., et al. (2019). Supercapacitor energy storage device using biowastes: A sustainable approach to green energy. *Sustainability, 11*(2), 414. doi:https://doi.org/10.3390/su11020414.

Paramati, S. R., Shahzad, U., & Doğan, B. (2022). The role of environmental technology for energy demand and energy efficiency: Evidence from OECD countries. *Renewable and Sustainable Energy Reviews, 153*, 111735. doi:https://doi.org/10.1016/j.rser.2021.111735.

Pundir, S., et al. (2023). Synthesis of 1D β-MnO2 for high-performance supercapacitor application. *Journal of Solid State Electrochemistry, 27*(2), 531-538. doi:https://doi.org/10.1007/s10008-022-05347-z.

Sari, F. N. I., So, P. R., & Ting, J. M. (2017). MnO2 with controlled phase for use in supercapacitors. *Journal of the American Ceramic Society, 100*(4), 1642-1652. doi:https://doi.org/10.1111/jace.14636.

Spinelli, F., et al. (2022). Shipping Decarbonization: An Overview of the Different Stern Hydrodynamic Energy Saving Devices. *Journal of Marine Science and Engineering, 10*(5), 574. doi:https://doi.org/10.3390/jmse10050574.

Thomas, M., et al. (2023). Nanoarchitectonics of high-performance supercapacitors based on mesoporous carbon and MnO2 electrodes using Aquivion electrolyte membrane. *Journal of Alloys and Compounds, 960*, 170719. doi:https://doi.org/10.1016/j.jallcom.2023.170719
Vangari, M., Pryor, T., & Jiang, L. (2013). Supercapacitors: review of materials and fabrication methods. *Journal of energy engineering, 139*(2), 72-79. doi:https://doi.org/10.1061/(ASCE)EY.1943-7897.0000102.

Zhang, Q., et al. (2021). Energy release from RuO2//RuO2 supercapacitors under dynamic discharge conditions. *Electrochimica Acta, 367*, 137455. doi:https://doi.org/10.1016/j.electacta.2020.137455.

Zhu, S., et al. (2020). Birnessite based nanostructures for supercapacitors: challenges, strategies and prospects. *Nanoscale Advances, 2*(1), 37-54. doi: https://doi.org/10.1039/C9NA00547A.

Chapter 10 Performance of a microbial fuel cell using MnO$_2$ as cathode catalyst

Capítulo 10 Desempeño de una celda de combustible microbiana empleando MnO$_2$ como catalizador catódico

CALZADO-ARAGÓN, Jenny†, FUENTES-ALBARRÁN, María del Carmen* and ALARCÓN-HERNÁNDEZ Fidel Benjamín

Universidad Autónoma del Estado de Morelos, Escuela de Estudios Superiores de Xalostoc. Av. Nicolás Bravo s/n, Parque Industrial Cuautla, C.P. 62717 Xalostoc, Ayala, Morelos, México.

ID 1st Author: *Jenny, Calzado-Aragón* / **ORC ID**: 0009-0002-6334-8576, **CVU CONAHCYT ID**: 1322232

ID 1st Co-author: *María del Carmen, Fuentes-Albarrán* / **ORC ID**: 0000-0003-1308-1332, **CVU CONAHCYT ID**: 171814

ID 2nd Co-author: *Fidel Benjamín, Alarcón-Hernández* / **ORC ID**: 0000-0002-2465-0898, **CVU CONAHCYT ID**: 131028

J. Calzado, M. Fuentes and F. Alarcón

*carmen.fuentes@uaem.mx

Abstract

Microbial fuel cells are electrochemical devices that use microorganisms as catalysts to produce electricity. Oxygen is the most used electron acceptor in the cathodic reaction of these systems, due to its abundance in the environment and high redox potential; however, the slow kinetics in oxygen reduction constitutes a limitation. Platinum (Pt) is the most widely used catalyst to accelerate the oxygen reduction reaction, but its high cost makes its use on a large scale impossible. In this study, the performance of manganese dioxide (MnO_2) as a cathodic catalyst in an H-type microbial fuel cell was examined. The MnO_2 layer on the carbon fiber surface was deposited by simply immersing the carbon in an aqueous $KMnO_4$ solution. The microbial fuel cell was characterized by polarization and power curves. A maximum power peak of 6.09 mW/m^2 was obtained with a current density of 22 mA/m^2, showing that MnO_2 can be a low-cost alternative to be used as catalytic material in the cathode of these devices.

Microbial fuel cell, Cathode Catalyst, Manganese Dioxide

Resumen

Las celdas de combustible microbianas son dispositivos electroquímicos que utilizan microorganismos como catalizadores para la producción de electricidad. El oxígeno es el aceptor de electrones más comúnmente utilizado en la reacción catódica de estos sistemas, debido a su abundancia en el ambiente y alto potencial redox, sin embargo, la lenta cinética en la reducción de oxígeno constituye una limitante. El platino (Pt) es el catalizador más ampliamente utilizado para acelerar la reacción de reducción del oxígeno, pero su alto costo imposibilita su uso a gran escala. En este estudio se examinó el desempeño de dióxido de manganeso (MnO_2) como catalizador catódico en una celda de combustible microbiana tipo H. La capa de MnO_2 sobre la superficie de fibra de carbón se depositó por simple inmersión del carbón en una solución acuosa de $KMnO_4$. La celda de combustible microbiana se caracterizó mediante curvas de polarización y potencia. Se obtuvo un máximo pico de potencia de 6.09 mW/m^2 con una densidad de corriente de 22 mA/m^2, mostrando que el MnO_2 puede ser una alternativa de bajo costo para utilizarse como material catalítico en el cátodo de estos dispositivos.

Celda de combustible microbiana, Catalizador Catódico, Dióxido de Manganeso

1. Introduction

The increase in industrial activity worldwide has led to an increase in the rate of carbon dioxide emissions. The global economy depends on fossil fuels, however, it has been projected that oil and gas reserves will be depleted by 2042 and coal by 2112 (Liew *et al*., 2014). In this context, renewable energies have gained great interest in different areas of research, such as solar, geothermal, wind, and biomass power generation. Microbial fuel cells (MFCs) are a technology that converts the energy contained in organic materials such as biomass and wastewater into electricity using microorganisms as catalysts (Qiu *et al*., 2021, Prasad and Tripathi, 2022). In addition to power generation, this technology finds application for bioremediation, toxic metal recovery, wastewater treatment, seawater desalination processes, etc. (Chaturvedi and Kundu, 2021).

A conventional microbial fuel cell (MFC) consists of two compartments separated by a proton exchange membrane. The anode is commonly maintained under anaerobic conditions, while the cathode may be suspended in aerobic solutions or exposed to air. In the anode compartment, microorganisms degrade organic matter, generating electrons and protons during their metabolism, with the anode becoming the electron acceptor. Electrons flow from the anode to the cathode through an external electrical circuit that commonly includes a resistor, while protons migrate to the cathode through the membrane that separates the two compartments. Finally, at the cathode, a final electron acceptor is reduced (Logan *et al*., 2006, Bazina *et al.,* 2023).

At the cathode of a MFC, oxygen is commonly used as the final electron acceptor due to its abundant availability in the environment and its high redox potential, however, the slow kinetics in the oxygen reduction reaction (ORR) is a limitation (Rizmani-Yazdi, *et al*., 2008). Pt has been widely used due to its favorable electrocatalytic performance relative to cathodic ORR in a MFC, but its high cost prohibits its use for commercial applications.

Different materials have been proposed as efficient catalysts for ORR, which include, carbon-based electrocatalysts, including heteroatoms (N, S, P, F, etc.) doped carbon catalysts (metal-free electrocatalysts), as well as transition metal-based electrocatalysts (Peera *et al.*, 2021).

In particular, manganese dioxide materials with different crystal structures have been widely used as cathode catalysts in microbial fuel cells, due to their low cost, good catalytic activity and because they are environmentally friendly. MnOx possess great structural diversity, combined with their physical and chemical properties, in addition to their wide applications in catalysis (Deng *et al.*, 2022), batteries (Zhuo *et al.*, 2020) and supercapacitors (AlAnazi *et al.*, 2023). Several researches have focused on the employment of MnO_2 as a cathode catalyst in MFCs employing different methods such as hydrothermal and electrodeposition to improve the performance of a MFC in electricity production (Phonsa *et al*, 2018, Majidi *et al.*, 2019, Chen *et al.*, 2022).

In this work, the performance of an H-type microbial fuel cell using MnO_2 as a cathodic catalyst was investigated for electricity production. The work was developed in three stages, in the first one, the synthesis and spontaneous deposition of MnO_2 on a carbon fiber electrode was performed, then the H-type MFC was assembled by monitoring the acclimation time of the cell, finally the fuel cell was characterized by polarization and power curves to examine its performance.

2. Experimental methodology

2.1. Microbial Fuel Cell Configuration

The microbial fuel cell (MFC) had an H-type configuration. The system consisted of two cylindrical glass compartments, with a diameter of 6 cm and a height of 8 cm, with a volume of 226.20 cm^3 each (Figure 2.1). A Nafion® 117 proton exchange membrane was used to separate the MFC compartments, and rim chamber gaskets were used between the compartments to prevent leakage. Air was constantly bubbled into the MFC catholyte using a fish tank pump. In the anolyte, a consortium from domestic wastewater and acetate (0.003 mol L^{-1}) was used as carbon source, in addition to a buffer solution (NH4Cl, 0.31 g L^{-1}; KCl, 0.31 g L^{-1}; NaH2PO4-2H2O, 3.32 g L^{-1}; Na2HPO4-2H2O, 10.32 g L^{-1}), this compartment was maintained under anaerobic conditions.

Carbon fiber (Fibre Glast Developments Corporation) was used for the electrodes, both electrodes had an area of 0.0018 m^2. The following sections describe the treatment given to the anode and the MnO_2 deposit on the MFC cathode. The cell was kept in operation for a period of 26 days at room temperature. Carbon fiber was used for the external connection.

Figure 2.1 Schematic of microbial fuel cell
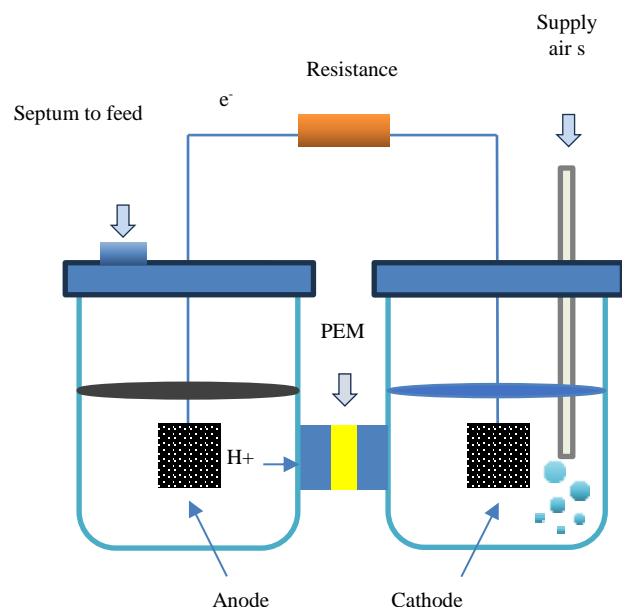
Source of Consultation: Own Elaboration

2.2. Treatment of the anode

The anode was immersed in acetone for 10 minutes at 29°C, then washed with ethanol under the same conditions and left to dry at room temperature. Next, the electrode was immersed in a 50% v/v nitric acid solution and kept in agitation for 4 hours at 80°C, and then washed several times with distilled water. The electrode was then dried in the culture oven for 1.5 hours at 120°C. The purpose of the anode treatment was to favor the adhesion of the bacteria, as well as to decrease the internal resistance, in addition to promoting the electronic transfer between the microorganisms and the anode (Cai, *et al.*, 2013).

2.3. Preparation of MnO$_2$ and deposition on the cathode

The cathode was placed in a 50 mL solution of 0.1 mol L^{-1} potassium permanganate (KMnO$_4$) for approximately 8 hours. By this procedure, the MnO$_2$ is spontaneously deposited on the carbon fiber electrode by simply immersing the carbon in the solution (Ma *et al.*, 2007). Once the indicated time had elapsed, the electrode was removed from the solution and allowed to stand for 30 minutes to allow the excess to drain. It was then placed in a culture oven at 90°C for 2 hours to dry completely. After the procedure was completed, the catalyzed cathode could be used for the following applications.

2.4. Data acquisition and characterization of the MFC

The H-type MFC was kept in operation for a period of 26 days. The acclimatization stage of the cell consisted of the colonization of the anode by the microorganisms. During this period, the open circuit voltage of the MFC was recorded using a multimeter (Steren Professional Deluxe Multimeter with PC interface, Model: MUL-600). When the cell reached a stable voltage, the cell was characterized by means of polarization and power curves, using an external resistor (R_{ext}), varying it in a range from 2 to 10 kΩ and recording the corresponding voltage obtained in the cell (E_{MFC}). For each pair of values (Ω-V) obtained experimentally, the current was calculated according to ohm's law:

$$I = \frac{E_{MFC}}{R_{ext}} \tag{1}$$

The polarization curve was obtained by plotting cell voltage vs. current. The power density curve was obtained from the polarization curve, plotting the power density vs. current density, considering that the cell power (P_{MFC}) is defined as:

$$P_{MFC} = \frac{E^2_{MFC}}{R_{ext}} \tag{2}$$

The power density obtained in this study was normalized to the area of the anode (mWm^{-2}).

3. Results

3.1. Acclimatization stage

Graph 3.1 shows the cell voltage as a function of operating time. During the first 5 days of operation, an exponential increase in voltage was observed, reaching a maximum of 0.8 V. Subsequently, the voltage began to decrease gradually, registering 0.24 V after 22 days of operation, which could be due to the depletion of organic matter by the microorganisms contained in the anode. In order to provide the carbon source to the MFC, acetate was supplied (as shown in the graph), increasing the voltage to 0.33 V. The system was monitored for a period of 26 days.

Graph 3.1 MCC acclimatization stage
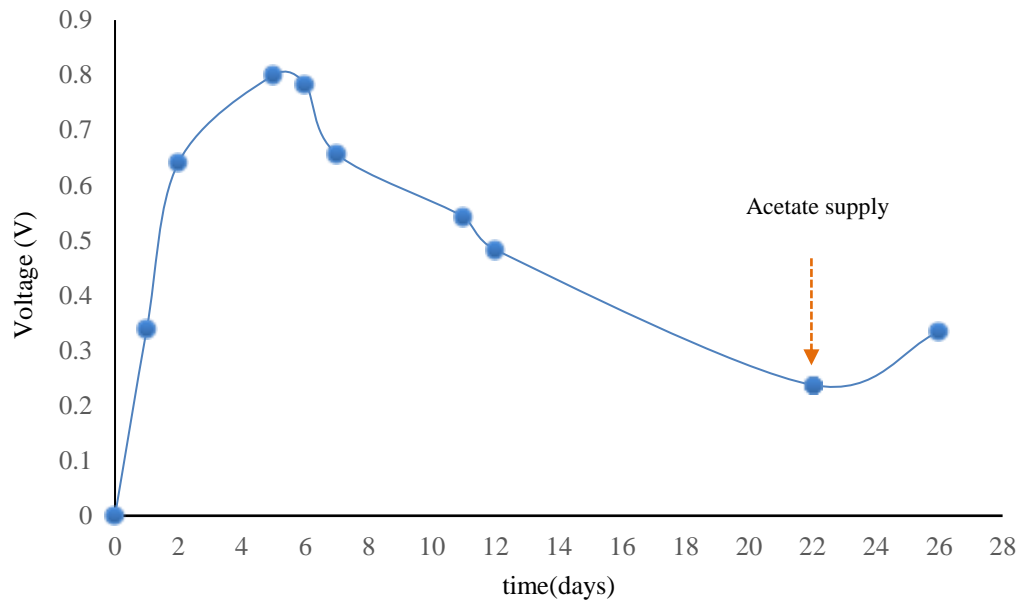
Source of Consultation: Own Elaboration

3.2. Polarization curve and power density

Graph 3.2 shows the polarization curve obtained in the MFC. It can be observed that the cell reached an open circuit voltage of 0.53 V, rapidly decaying to 0.32 V. This rapid loss of voltage at low currents corresponds to the activation losses, i.e., the activation energy that the reactant species of both electrodes must overcome. The anode is influenced by the type of substrate used as well as the microbial culture, while the cathode depends on the reduction kinetics (Rizmani-Yazdi *et al.*, 2008). Graph 3.2 also shows a zone of almost linear voltage drop in an interval of 0.3 and 0.25 V, in this region is located the maximum peak power generated by the cell, some of the factors that influence these losses are the cell configuration and the resistivity of the different conductors, so it is important to minimize these potential losses to optimize the performance of a MFC (Clauwaert *et al.*, 2008). Finally, the graph shows a rapid potential drop at high current densities.

Graph 3.2. Polarization curve
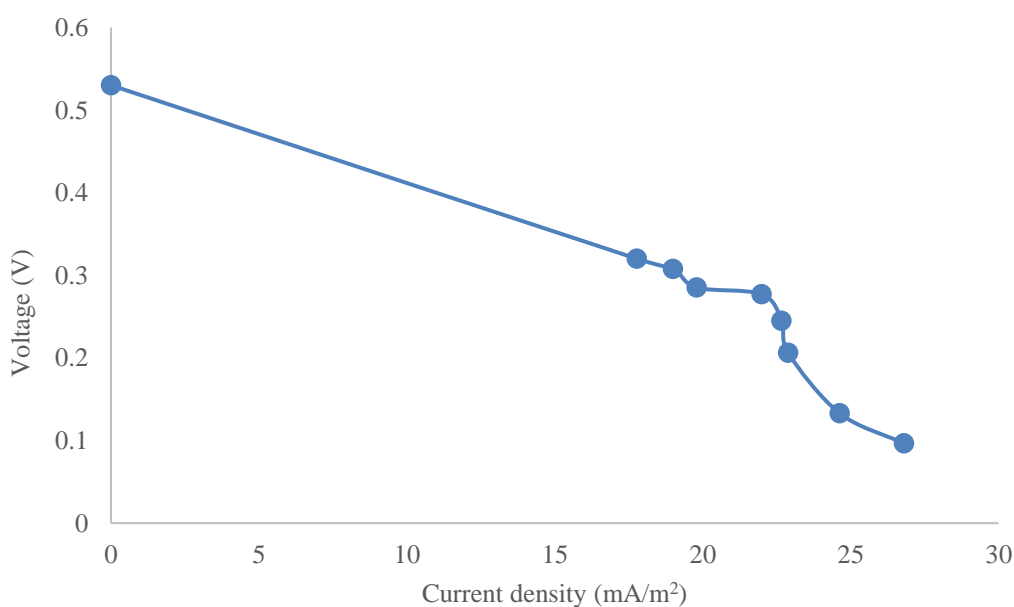
Source of Consultation: Own Elaboration

Graph 3.3 shows the power density obtained in the cell as a function of current density. The MFC obtained a maximum peak power of 6.09 mW/m^2 with a current density of 22 mA/m^2. (Fuentes *et al*., 2020) used the same method as this study to obtain MnO$_2$. The crystalline structure they identified was birnessite-type MnO$_2$. The method used in this work to deposit the catalyst on the MFC cathode has several advantages over other synthesis methods, and it is certainly attractive from a cost-effectiveness point of view, since unlike other synthesis methods it is simple and allows preparing a low-cost catalyst.

Graph 3.3 Power Density Curve
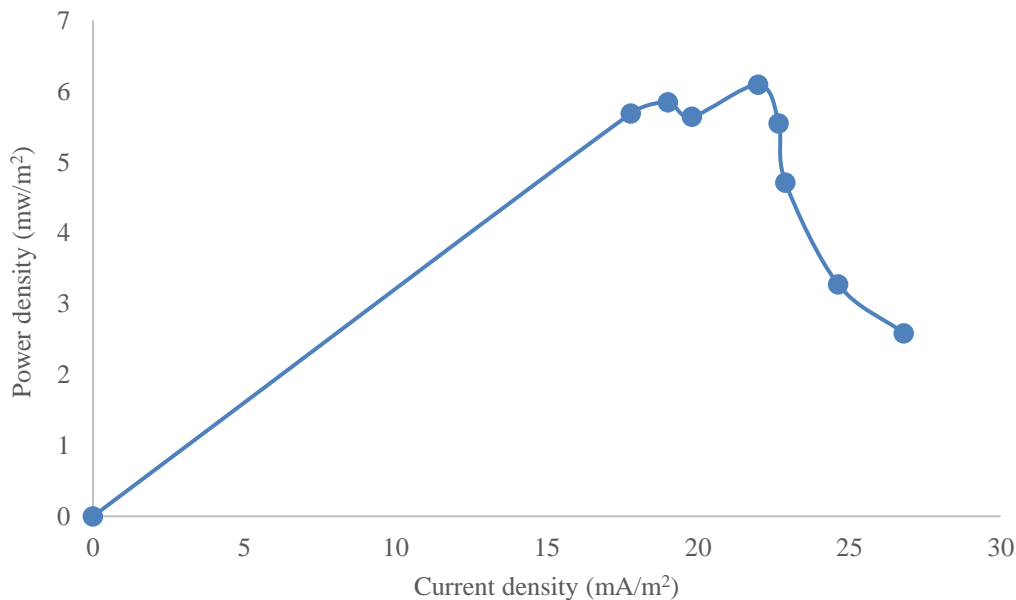
Source of Consultation: Own Elaboration

Acknowledgements

Conclusions

– In this study, birnesite-type MnO$_2$ was synthesised on a carbon fibre cathode by simply immersing the electrode in an aqueous solution of KMnO$_4$.

– Using this catalytic material in an H-type MFC, a maximum power output of 6.09 mW/m2 with a current density of 22 mA/m^2 was obtained.

– Domestic wastewater is an ecological liability that can be used in a MFC to generate electricity, while at the same time purifying this waste.

– For future work, it is suggested to optimise the cell configuration to reduce ohmic losses, as well as to increase the conductivity of the system to improve the power output.

References

AlAnazi, M., Ghrib, T., Ercan, F., Alsubaie, M., Demirci, T., Kaygili, O., Kayed , T., S., Ercan, I. (2023). Structural, optical, and electrical investigation of multilayered MnO2(n)/NiO(p) heterojunctions for supercapacitors applications. *Surfaces and Interfaces,* 103321. https://doi.org/10.1016/j.surfin.2023.103321

Bazina, N., Ahmed, T., G., Almdaaf, M., Jibia, S., Sarker, M. (2023). Power generation from wastewater using microbial fuel cells: A review. *Journal of Biotechnology,*374, 17-30. https://doi.org/10.1016/j.jbiotec.2023.07.006

Cai, H., Wang, J., Bu, Y., Zhong, Q. (2013). Treatment of carbon cloth anodes for improving power generation in a dual-chamber microbial fuel cell. *Journal Chemical Technology Biotechnology,* 88, 623-628. https://doi.org/10.1002/jctb.3875

Chaturvedi, A., y Kundu, P., P. (2021). Recent advances and perspectives in platinum-free cathode catalysts in microbial fuel cells. *Journal of Environmental Chemical Engineering,* 9, 105662. https://doi.org/10.1016/j.jece.2021.105662

Chen, J., Liu, Y., Yang, J., Wang, H., Liu, H., Cao, S., Zhang, X., Wang, R., Liu, Y., Yang, Y. (2022). The potential of Co_3O_4 nanoparticles attached to the surface of MnO2 nanorods as cathode catalyst for single-chamber microbial fuel cell. *Bioresource Technology,* 346, 126584. https://doi.org/10.1016/j.biortech.2021.126584

Clauwaert, P., Aelterman, P., Pham, T., H., Schamphelaire, L., D., Carballa, M., Rabaey, K., Verstraete, W. 2008. Minimizing losses in bio-electrochemical systems: the road to applications. *Applied Microbiology and Biotechnology,* 79, 901-913. http://dx.doi.org/10.1007/s00253-008-1522-2

Deng, P., Fang, H., Liu, R., Guo, X., Chen, P. (2022). One-pot hydrothermal synthesis of flower-like MnO2 nanostructure with rich oxygen vacancy for catalysis thermal-induced pyrolysis of energetic molecular perovskite. *Vacuum*, 203, 111234. https://doi.org/10.1016/j.vacuum.2022.111234

Fuentes, M., C., Juárez, K., Gamboa, S., Tirado, A., Alvarez, A. (2020). Improving the power density of a Geobacter consortium-based microbial fuel cell by incorporating a highly dispersed birnessite/C cathode. *Journal Chemical Technology Biotechnology,* 95, 3169-3178. https://doi.org/10.1002/jctb.6495

Liew, K., B., Daud, W., R., W., Ghasemi, M., Leong, J., X., Lim, S., S., Ismail, M. (2014). Non-Pt catalyst as oxygen reduction reaction in microbial fuel cells: A review. *International Journal of hydrogen energy,* 39, 4870-4883. https://doi.org/10.1016/j.ijhydene.2014.01.062

Logan, B., E., Hamelers, B., Rozendal, R., Schröder, U., Keller, J., Freguia, S., Aelterman, P., Verstraete, W., Rabaey, K., 2006. Microbial fuel cells: Methodology and Technology. *Environmental Science and Technology,* 40, 5181-5192. https://doi.org/10.1021/es0605016

Ma, S., B., Ahn, K., Y., Lee, E., S., Oh, K., H., Kim, K., B. (2007). Synthesis and characterization of manganese dioxide spontaneously coated on carbon nanotubes. *Carbon,* 45, 375-382. https://doi.org/10.1016/j.carbon.2006.09.006

Majidi, M., R., Farahani, F., S., Hosseini, M., Ahadzadeh, I. (2019). Low-cost nanowired α-MnO2/C as an ORR catalyst in air-cathode microbial fuel cell. *Bioelectrochemistry,* 125, 38-45. https://doi.org/10.1016/j.bioelechem.2018.09.004

Peera, S., G., Maiyalagan, T., Liu, C., Ashmath, S., Lee, T., G., Jiang, Z., Mao, S. (2021). A review on carbon and non-precious metal-based cathode catalysts in microbial fuel cells. *International Journal of hydrogen energy,* 46, 3056-3089. https://doi.org/10.1016/j.ijhydene.2020.07.252

Phonsa, S., Sreearunothai, P., Charojrochkul, S., Sombatmankhong, K. (2018). Electrodeposition of MnO2 on polypyrrole-coated stainless steel to enhance electrochemical activities in microbial fuel cells, *Solid State Ionics,* 316, 125-134. https://doi.org/10.1016/j.ssi.2017.11.022

Prassad, J., y Tripathi, R., K. (2022). Review on improving microbial fuel cell power management systems for consumer applications. *Energy Reports,* 8, 10418-10433. https://doi.org/10.1016/j.egyr.2022.08.192

Qiu, S., Guo, Z., Naz, F., Yang, Z., Yu, C. (2021). An overview in the development of cathode materials for the improvement in power generation of microbial fuel cells. *Bioelectrochemistry,* 141, 107834. https://doi.org/10.1016/j.bioelechem.2021.107834

Rismani-Yazdi, H., Carver, S., M., Christy, A., D., Tuovinen, O., H., 2008. Cathodic limitations in microbial fuel cells: An overview. *Journal of power sources.* 180, 683-694. https://doi.org/10.1016/j.jpowsour.2008.02.074

Zhuo, Y., Zhu, Y., Tang, X., Zhao, M., Ren, P., Su, W., Tang, Y., Chen, Y. (2020). MnO$_2$ supported on acrylic cloth as functional separator for high-performance lithium–sulfur batteries. *Journal of Power Sources,* 464, 228181. https://doi.org/10.1016/j.jpowsour.2020.228181

[[Title in Times New Roman and Bold No. 14 in English and Spanish]

Surname (IN UPPERCASE), Name 1st Author†*, Surname (IN UPPERCASE), Name 1st Coauthor, Surname (IN UPPERCASE), Name 2nd Coauthor and Surname (IN UPPERCASE), Name 3rd Coauthor

Institution of Affiliation of the Author including dependency (in Times New Roman No.10 and Italics)

International Identification of Science - Technology and Innovation

ID 1st Author: (ORC ID - Researcher ID Thomson, arXiv Author ID - PubMed Author ID - Open ID) and CVU 1st author: (Scholar-PNPC or SNI-CONAHCYT) (No.10 Times New Roman)

ID 1st Coauthor: (ORC ID - Researcher ID Thomson, arXiv Author ID - PubMed Author ID - Open ID) and CVU 1st author: (Scholar-PNPC or SNI-CONAHCYT) (No.10 Times New Roman)

ID 2nd Coauthor: (ORC ID - Researcher ID Thomson, arXiv Author ID - PubMed Author ID - Open ID) and CVU 1st author: (Scholar-PNPC or SNI-CONAHCYT) (No.10 Times New Roman)

ID 3rd Coauthor: (ORC ID - Researcher ID Thomson, arXiv Author ID - PubMed Author ID - Open ID) and CVU 1st author: (Scholar-PNPC or SNI-CONAHCYT) (No.10 Times New Roman)

Instructions for Scientific, Technological and Innovation Publication

Abstract (In English, 150-200 words)

Text written in Times New Roman No.12, single space

Keywords (In English)

Indicate 3 keywords in Times New Roman and Bold No. 12

1 Introduction

Text in Times New Roman No.12, single space.

General explanation of the subject and explain why it is important.

What is your added value with respect to other techniques?

Clearly focus each of its features

Clearly explain the problem to be solved and the central hypothesis.

Explanation of sections Chapter.

Development of headings and subheadings of the chapter with subsequent numbers

[Title No.12 in Times New Roman, single spaced and bold]

Products in development No.12 Times New Roman, single spaced.

Including graphs, figures and tables-Editable

In the Chapter content any graphic, table and figure should be editable formats that can change size, type and number of letter, for the purposes of edition, these must be high quality, not pixelated and should be noticeable even reducing image scale.

[Indicating the title at the bottom with No.10 and Times New Roman Bold]

Table 1.1 Title

Variable	Descripción	Valor
V_V	Volumen de Venta	20000
P_V	Postura de venta	490.61
V_C	Volumen de Compra	20000
P_c	Postura de Compra	485.39
P^{Uh}	Precio último Hecho	491.61
V_o	Volumen Operado	1241979
P_u	Precio/Utilidad	0
P^{VL}	Precio/Valor Libro	0
U_a	Utilidad p/Acción	0
V^{La}	Valor Libro p/Acción	0

Source (in italics)
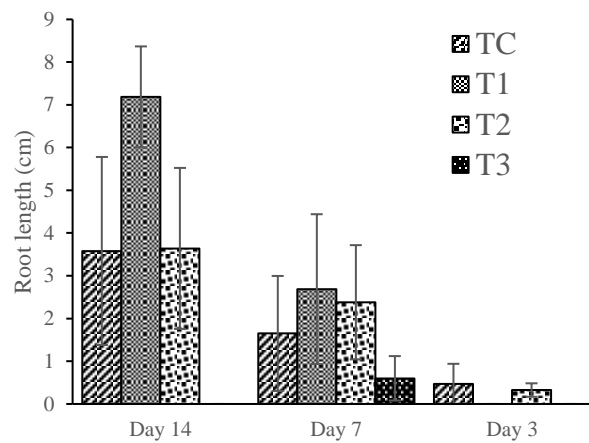Should not be images-everything must be editable.

Figure 1.1 Title
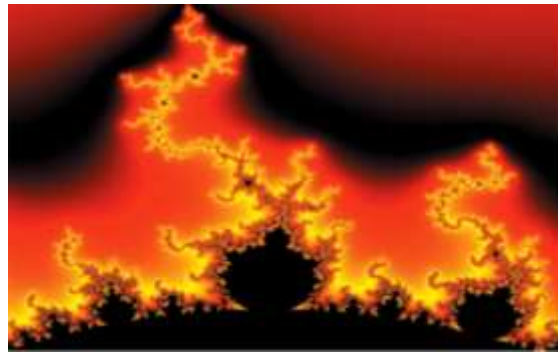
Source (in italics)

Should not be images-everything must be editable.

Graphic 1.1 Title

Source (in italics)

Should not be images-everything must be editable.

Each chapter shall present separately in **3 folders**: a) Figures, b) Charts and c) Tables in .JPG format, indicating the number and sequential Bold Title.

For the use of equations, noted as follows:

$$\int_{lim^{-1}}^{lim^1} = \int \frac{lim^1}{lim^{-1}} = \left[\frac{1\,(-1)}{lim}\right]^2 = \frac{(0)^2}{lim} = \sqrt{lim} = 0 = 0 \rightarrow \propto \qquad (1)$$

Must be editable and number aligned on the right side.

Methodology

Develop give the meaning of the variables in linear writing and important is the comparison of the used criteria.

Results

The results shall be by section of the Chapter.

Annexes

Tables and adequate sources

Instructions for Scientific, Technological and Innovation Publication

Thanks

Indicate if they were financed by any institution, University or company.

Conclusions

Explain clearly the results and possibilities of improvement.

References

Use APA system. Should not be numbered, nor with bullets, however if necessary numbering will be because reference or mention is made somewhere in the Chapter.

Use Roman Alphabet, all references you have used must be in the Roman Alphabet, even if you have quoted an Chapter, book in any of the official languages of the United Nations (English, French, German, Chinese, Russian, Portuguese, Italian, Spanish, Arabic), you must write the reference in Roman script and not in any of the official languages.

Technical Specifications

Each chapter must submit your dates into a Word document (.docx):

Handbooks title
Chapter title
Abstract
Keywords

Proceedings sections, for example:

1. Introduction
2. Description of the method
3. Analysis from the regression demand curve
4. Results
5. Thanks
6. Conclusions
7. References

Author Name (s)
Email Correspondence to Author
References

Intellectual Property Requirements for editing:

-Authentic Signature in Color of <u>Originality Format</u> Author and Coauthors

-Authentic Signature in Color of the <u>Acceptance Format</u> of Author and Coauthors

-Authentic Signature in Color of the <u>Conflict of Interest Format</u> of Author and Co-authors.

Reservation of Editorial Policy

ECORFAN Handbooks se reserva el derecho de hacer los cambios editoriales requeridos para adecuar la Obra Científica a la Política Editorial del ECORFAN Handbooks. Una vez aceptada la Obra Científica en su versión final, el ECORFAN Handbooks enviará al autor las pruebas para su revisión. ECORFAN® únicamente aceptará la corrección de erratas y errores u omisiones provenientes del proceso de edición de la revista reservándose en su totalidad los derechos de autor y difusión de contenido. No se aceptarán supresiones, sustituciones o añadidos que alteren la formación de la Obra Científica.

Code of Ethics - Good Practices and Declaration of Solution to Editorial Conflicts

Declaration of Originality and unpublished character of the Scientific Work, of Authorship, on the obtaining of data and interpretation of results, Acknowledgments, Conflict of interests, Assignment of rights and distribution

The ECORFAN-Mexico, S.C Directorate asserts to the Authors of the Scientific Work that its content must be original, unpublished and of Scientific, Technological and Innovation content to be submitted for evaluation.

The Authors signing the Scientific Work must be the same that have contributed to its conception, realization and development, as well as the obtaining of data, interpretation of the results, its writing and revision. The Correspondent Author of the proposed Scientific Work will request the form that follows.

Title of the Scientific Work:

–   The sending of a Scientific Work to ECORFAN Handbooks emanates the commitment of the author not to submit it simultaneously to the consideration of other serial publications for it must complement the Format of Originality for its Scientific Work, unless it is rejected by the Arbitration Committee, may be withdrawn.

–   None of the data presented in this Scientific Work has been plagiarized or invented. The original data are clearly distinguishable from those already published. And you have knowledge of the test in PLAGSCAN if a level of plagiarism is detected Positive will not proceed to arbitrate.

–   References are cited on which the information contained in the Scientific Work is based, as well as theories and data from other previously published Scientific Works.

–   The authors sign the Authorization Form for their Scientific Work to be disseminated by means that ECORFAN-Mexico, S.C. in its Holding Mexico consider relevant for the dissemination and dissemination of its Scientific Work by giving up its Scientific Work Rights.

–   The consent of those who have provided unpublished data obtained by verbal or written communication has been obtained, and such communication and authorship are adequately identified.

–   The Author and Co-Authors who sign this work have participated in its planning, design and execution, as well as in the interpretation of the results. They also critically reviewed the paper, approved its final version and agreed with its publication.

–   No signature responsible for the work has been omitted and the criteria of Scientific Authorization are satisfied.

–   The results of this Scientific Work have been interpreted objectively. Any result contrary to the point of view of those who sign is exposed and discussed in the Scientific Work.

Copyright and Access

The publication of this Scientific Work entails the transfer of the copyright to ECORFAN-Mexico, SC in its Mexico Holding for its ECORFAN Handbooks, which reserves the right to distribute on the Web the published version of the Scientific Work and the making available of the Scientific Work in this format supposes for its Authors the fulfillment of what is established in the Law of Science and Technology of the United States of Mexico, regarding the obligation to allow access to the results of Scientific Research.

Title of the Scientific Work:

Name and surnames of the Contact Author and the Coauthors	Signature
1.	
2.	
3.	
4.	

Principles of Ethics and Declaration of Solution to Editorial Conflicts

Publisher Responsibilities

The Publisher undertakes to guarantee the confidentiality of the evaluation process, it may not disclose to the Arbitrators the identity of the Authors, nor may it reveal the identity of the Arbitrators at any time.

The Editor assumes the responsibility of properly informing the Author of the phase of the editorial process in which the text is sent, as well as the resolutions of Double Blind Arbitration.

The Editor must evaluate the manuscripts and their intellectual content without distinction of race, gender, sexual orientation, religious beliefs, ethnicity, nationality, or the political philosophy of the Authors.

The Editor and his editing team of ECORFAN® Holdings will not disclose any information about the Scientific Work sent to anyone other than the corresponding Author.

The Editor must make fair and impartial decisions and ensure a fair peer arbitration process.

Responsibilities of the Editorial Board

The description of the processes of peer review is made known by the Editorial Board in order that the Authors know the evaluation criteria and will always be willing to justify any controversy in the evaluation process. In case of Detection of Plagiarism to the Scientific Work the Committee notifies the Authors for Violation to the Right of Scientific, Technological and Innovation Authorization.

Responsibilities of the Arbitration Committee

The Arbitrators undertake to notify about any unethical conduct by the Authors and to indicate all the information that may be reason to reject the publication of the Scientific Work. In addition, they must commit to keep confidential information related to the Scientific Work that they evaluate.

Any manuscript received for your arbitration must be treated as confidential, must not be displayed or discussed with other experts, except with the permission of the Editor.

The Referees should conduct themselves objectively, any personal criticism of the Author is inappropriate.

The Arbitrators must express their points of view with clear and valid arguments that contribute to the Scientific, Technological and Innovation of the Author.

The Arbitrators should not evaluate the manuscripts in which they have conflicts of interest and that they have been notified to the Editor before submitting the Scientific Work to evaluation.

Responsibilities of Authors

Authors must ensure that their Scientific Works are the product of their original work and that the data have been obtained in an ethical manner.

Authors must ensure they have not been previously published or are not being considered in another serial publication.

Authors must strictly follow the rules for the publication of Scientific Works defined by the Editorial Board.

Authors should consider that plagiarism in all its forms constitutes unethical editorial conduct and is unacceptable, consequently any manuscript that incurs plagiarism will be removed and not considered for publication.

Authors should cite publications that have been influential in the nature of the Scientific Work submitted to arbitration.

Information services

Indexing - Bases and Repositories

RESEARCH GATE (Germany)
MENDELEY (Bibliographic References Manager)
GOOGLE SCHOLAR (Citation indices-Google)
REDIB Ibero-American Network of Innovation and Scientific Knowledge-CSIC

Publishing Services

Citation and Index Identification H
Management of Originality Format and Authorization
Testing of Handbooks with PLAGSCAN
Evaluation of Scientific Work
Issuance of Certificate of Arbitration
Edition of Scientific Work
Web layout
Indexing and Repository
Publication of Scientific Work
Certificate of Scientific Work
Editing Service Billing

Editorial Policy and Management

Park Pedregal Business 3580 - Adolfo Ruiz Cortines Boulevar, CP-01900. San Jeronimo Aculco Álvaro Obregón - Mexico City. Phones: +52 1 55 6159 2296, +52 1 55 1260 0355, +52 1 55 6034 9181; Email: contact@ecorfan.org www.ecorfan.org